学位論文

# $J/\psi$ photoproduction in Au+Au ultra-peripheral collisions at $\sqrt{s_{NN}} = 200$ GeV at RHIC

(RHICでの核子対あたり重心系衝突エネルギー200GeVの金金原子核超周辺衝突における$J/\psi$ 光生成)

平成25年12月博士(理学)
申請

東京大学大学院理学系研究科
物理学専攻
髙原 明久

# Abstract

The photo production of $J/\psi$ in Au+Au collisions at the center of mass energy per nucleon pair of 200 GeV have been studied at the PHENIX experiment at mid and forward rapidity at Relativistic Heavy Ion Collider (RHIC) at Brookhaven National Laboratory (BNL).

For central-rapidity, the $d\sigma/dy$ of $J/\psi$ $+Xn(< 2mrad)$ was measured to be $45.6 \pm 13.2$ (stat)$\pm$ 6.0 (sys) $\mu$b. The $d^2\sigma/dydp_T$ of $J/\psi$ $+Xn(< 2mrad)$ distribution was measured and it shows clear coherent peak and wider incoherent distribution. Additionally, the result of first measurement at forward-rapidity was described in the thesis. The new result shows incoherent process is dominant at the forward rapidity region.

# Abstract

米国率ブルックヘブン研究所における RHIC 加速器を用いた PHENIX 実験において核子対あたり重心系エネルギー 200GeV での金金衝突における $J/\psi$ の光合成過程を前方及び後方ラピディティ領域において測定した。中心ラピディティ領域において $J/\psi + Xn(< 2mrad)$, $d\sigma/dy$ 45.6 ± 13.2 (stat) ± 6.0 (sys) $\mu$b の結果を得た。$d^2\sigma/dydp_T$ of $J/\psi + Xn(< 2mrad)$ 分布の測定を行い、明瞭なコヒーレントピークと広いインコヒーレント分布を確認した。

加えて前方領域については初の測定を行った。この新しい結果は前方ではインコヒーレント過程が種であると示すものである。

# Contents

# List of Figures

# List of Tables

# Chapter 1

# Introduction

In 1969, in the *ep* deep inelastic scattering (DIS) experiment at Stanford Linear Accelerator Center (SLAC) found point like particles were found inside the nucleon [1]. Since then, there have been many experiments to study the inner structure of the nucleon at CERN, DESY, and FNAL [2]. These experiments showed a nucleon is a complex object with valence quarks, sea quarks and gluons.

The momentum distribution of partons inside a nucleon, called as a Parton Distribution Function (PDF), has been measured as a function of Bjorken $x$ and $Q^2$ being the energy scale of the hard interaction.

Especially, HERA found a rapid increase of the gluon distribution with decrease $x$ are shown in Fig 1.1 [1].

In the $l$A experiments, notable nuclear modification of PDF was found [3, 4, 5, 6, 7, 8, 9, 10]. However, its mechanism and amplitude are not well understood theoretically. Recently, ultra-peripheral heavy ion collisions have attracted great interests to study the parton distribution in the nucleus by using the strong electromagnetic fields that act as a field of photons provided by fast moving heavy ions. Especially, exclusive photo-nuclear vector meson production is a sensitive probe of gluons inside nuclei. Ultra-peripheral collision (UPC) is the collision whose impact parameter is larger than the sum of the two nuclear radii. The $\gamma$ flux of the UPC is proportional of the square charge of the nuclei, $Z^2$.

In this thesis, $J/\psi$ productions in the UPC are studied at Au+Au collisions at RHIC-PHENIX in Brookheaven National Laboratory. The maximum center of mass energy in the $\gamma$Au system is 34 GeV, which is large enough to produce a $J/\psi$. The UPC $J/\psi$ measurement at RHIC is sensitive to the gluon distributions in the nucleus down to $x \cong 0.015$, at $Q^2 = 2.5$ (GeV/$c$)$^2$.

The PHENIX already published the measurement of $J/\psi$ production in ultra-peripheral collisions using the data samples taken in 2004 [30]. Only the total cross section at the central rapidity was measured, and it has too low statics to discuss non-linear Quantum chromodynamics (QCD) evolution at small $x$. The purpose of this study is to measure the $p_T$ dependence of the cross section by using data which was taken in 2007. The cross section of $J/\psi$ production in the UPC (UPC $J/\psi$ ) is a relatively simple process so that is useful to study low $x$ QCD.

The PHENIX detector has wide acceptance in both central and forward rapidity regions. The cross sections and its $p_T$ dependence of UPC $J/\psi$ in the forward rapidity region are measured for the first time.

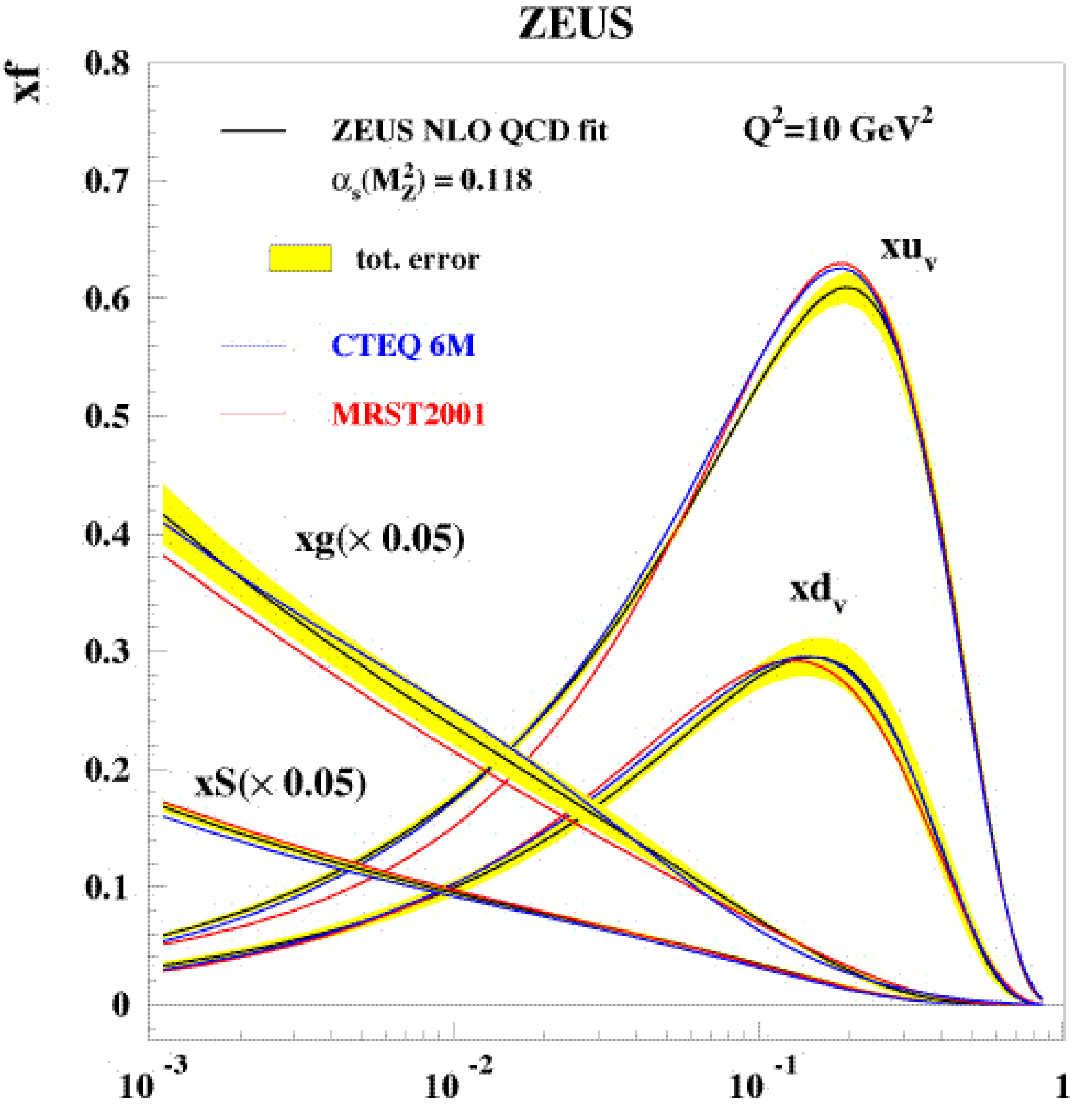

**Figure 1.1:** Gluon, sea and u and d valence distributions extracted by HERA-ZEUS at $Q^2$ =10 GeV$^2$ [1]

The organization of the thesis is as follows. A brief summary of related theoretical background is described in Chapter 2. The experimental setup, the RHIC accelerator and PHENIX detectors are briefly explained in Chapter 3. The detail of trigger and conditions in 2007 and 2010 PHENIX runs are described in Chapter 4. The detail of analysis of 2007 UPC $J/\psi \to e^+e^-$ at central rapidity and 2010 UPC $J/\psi \to \mu^+\mu^-$ at forward rapidity are presented in Chapter 5 and 6, respectively. The results and discussions are shown in Chapter 7. The summary is given in Chapter 7.

### Major Contribution

The author carried out the measurement and analysis of $J/\psi$ photo-production with $J/\psi \to e^+e^-$ and $J/\psi \to \mu^+\mu^-$ channels for the 2007 and 2010 runs at the PHENIX experiments. The author took the responsibilities of the operation and calibration of the Ring Imaging Cherenkov Counters.

# Chapter 2

# Theoretical backgrounds

## 2.1 Deep inelastic scattering and nucleon structure

In the inclusive measurements of the deep inelastic scattering, kinematics can be described by two variables. An example choice is the negative square of momentum transfer, $Q^2$ and the Bjorken $x$ which is defined as $Q^2/2M\nu$, where M is mass of the target and $\nu$ is the energy transfer between incoming and outgoing lepton at the rest frame of the target.

### 2.1.1 Kinematics of deep Inelastic collisions and PDF

Start from the simplest case. The differential cross section of A+B is described by the following equation.

$$\frac{d\sigma}{d\Omega} = \frac{\alpha^2 \cos^2 \frac{\theta}{2}}{4E^2 \sin^2 \frac{\theta}{2}} \left( \equiv \frac{d\sigma}{d\Omega_{Mott}} \right), \tag{2.1}$$

where $m$ is the mass of A and $M$ is the mass of B, $\alpha$ is the electromagnetic coupling constant, $\theta$ is the scattering angle, and $E$ is the incident energy. $m/M \ll 1$ is assumed. If the probe (A) and target (B) have spin 1/2, the differential cross section in fixed target A+B elastic scattering is described by the following equation.

$$\frac{d\sigma}{d\Omega} = \frac{d\sigma}{d\Omega_{Mott}} \frac{E'}{E} \left[ 1 - \frac{q^2}{2M^2} \tan^2 \frac{\theta}{2} \right], \tag{2.2}$$

where $E$ and $E'$ are initial and final energy of A, and $q$ is the momentum transfer. If B is not point like particle, a form factor ($F$) is introduced. It is Fourier transformation of the density function ($\rho(\vec{r})$) defined as,

$$F(q^2) = \int d^3 r e^{i\vec{r}\cdot\vec{q}} \rho(\vec{r}). \tag{2.3}$$

The elastic cross section is then described in the form of

$$\frac{d\sigma}{d\Omega} = \frac{d\sigma}{d\Omega_{Mott}}\frac{E'}{E}\left[\left(F_1^2 + \frac{\kappa^2 Q^2 F_2^2}{4M^2}\right) - (F_1 + \kappa F_2^2)^2 \frac{Q^2}{2M^2}\tan^2\frac{\theta}{2}\right], \tag{2.4}$$

where $F_1$ and $F_2$ are form factors, $F_1(0) = 1, F_2(0) = 1$, and $\kappa$ is the anomalous magnetic moment .

For the inelastic scattering, which includes all possible final states, the inclusive scattering cross section is expressed as follows with an extra variable, the final A energy ($E'$)

$$\frac{d^2\sigma}{d\Omega dE'} = \frac{d\sigma}{d\Omega_{Mott}}\left[W_2(Q^2,\nu) + 2W_1(Q^2,\nu)\tan^2\frac{\theta}{2}\right], \tag{2.5}$$

where $\nu = E - E'$ and $W_1, W_2$ are structure functions which are related to $\rho$. Once, $\frac{d^2\sigma}{d\Omega dE'}$ is measured in a many $Q^2$ , $\nu$ points, $\rho(\vec{r})$ is deduced. The formula can be converted to $x$ and $y$ variables (Bjorken $x$ and rapidity $y \equiv nu/E$).

$$\frac{d^2\sigma}{dxdy} = \frac{4\pi\alpha^2 s}{Q^4}\left[2xF_1\frac{1+(1-y)^2}{2} + (1-y)(F_2 - 2xF_1) - \frac{M}{2E}xyF_2\right], \tag{2.6}$$

where $s$ is the square of the center-of-mass energy and $2ME$. $F_1$ and $F_2$ are different form factors from the ones in Eq. 2.4. This new structure functions are related to $W_{1,2}$ such as $F_1 = MW_1$ and $F_2 = \nu W_2$.

### 2.1.2 Parton model

At the beginning of DIS experiments, the region of $x \sim 0.1$ was covered in the measurements. As shown in Fig 2.1, $F_2$ is independent of $Q^2$ in the region (Bjorken scaling).

To reproduce the scaling, parton model is proposed. The basic ideas of parton model are following;

- Nucleon is consistent of point like particles (parton).
- At the time of the interaction, they can be seen as a collection of free particle .
- However, they are bound in the nucleon.

In this picture, $d\sigma/dy$ of virtual photon and $i$th parton is as follows,

$$\frac{d\sigma}{dy} = \frac{4\pi\alpha^2 xs}{Q^4}\left[\frac{1+(1-y)^2}{2} - \frac{M}{2E}\right]\lambda_i^2 q_i(x)dx, \tag{2.7}$$

where $q_i(x)$ and $\lambda_i$ are momentum distribution function and charge of $i$th parton, respectively. Therefore, $d\sigma/dy$ of virtual photon and proton is

$$\frac{d^2\sigma}{dxdy} = \frac{4\pi\alpha^2 xs}{Q^4}\left[\frac{1+(1-y)^2}{2} - \frac{M}{2E}\right]\Sigma\lambda_i^2 q_i(x)dx. \tag{2.8}$$

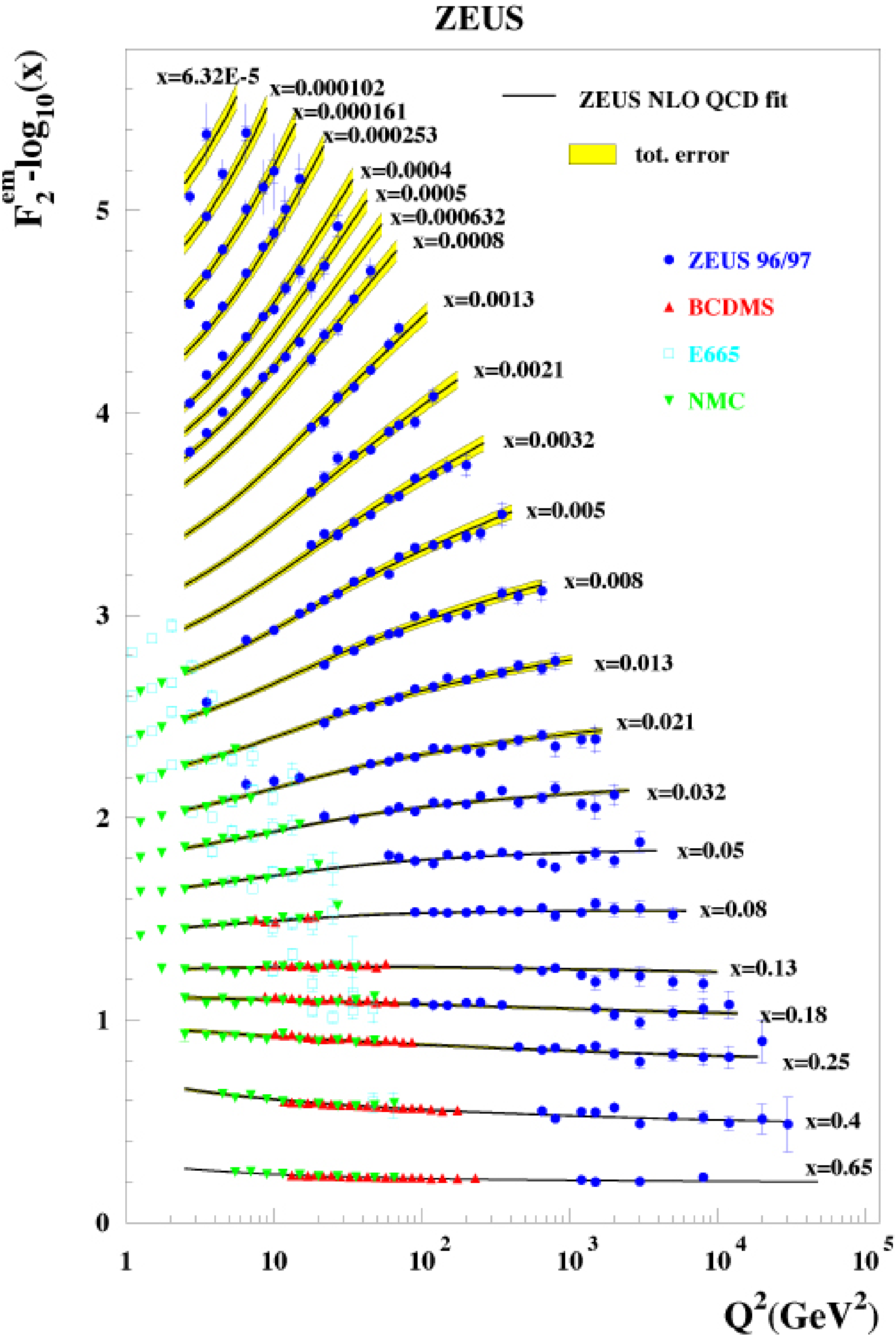

**Figure 2.1:** The measured $F_2$ distributions via e+p collisions [1]

To compare with Eq. 2.6

$$F_2 = 2x\lambda_i^2 q_i(x) \tag{2.9}$$

$$F_1 = F_2/2x \tag{2.10}$$

The equations show dimensionless structure functions are independent of $Q$. In this picture, $F_2$ is the charge-square weighted distribution of partons. Through the measurement of structure functions, momentum distribution of the parton can be deduced. $x$ corresponds to the momentum fraction of the proton carried by the parton in the picture.

As shown in Fig 2.1, in recent years, in the lower $x$ regions, $F_2$ was found to depend on $Q^2$ . As different from parton model, interaction between partons plays an important role, therefore $Q^2$ independence is disturbed. In the region of $x$∼0.1, $Q^2$ independence is incidentally consistent.

### 2.1.3 DGLAP equation

Dokshitzer-Gribov-Lipatov-Altarelli-Parisis (DGLAP) equations describe the $Q^2$ dependence of PDF based on the QCD [11].

From the equations, the distributions for the higher $Q^2$ are predicted. At the limit of high $Q^2$ where the transverse momentum of the partons are neglected, the evolution of the quark ($q$) and gluon ($g$) distribution functions can be written as;

$$\frac{dq(x,Q^2)}{d\ln Q} = \frac{\alpha_s(Q^2)}{\pi}\int_x^1 \frac{d\xi}{\xi} P_{q\leftarrow q}(\xi) q(x/\xi, Q) + P_{q\leftarrow g} g(x/\xi, Q), \tag{2.11}$$

$$\frac{dg(x,Q^2)}{d\ln Q} = \frac{\alpha_s(Q^2)}{\pi}\int_x^1 P_{g\leftarrow q}(\xi)\Sigma_i[q_i(x/\xi, Q) + q_i(x/\bar{\xi}, Q)] + P_{g\leftarrow g} g(x/\xi, Q), \tag{2.12}$$

where $P$ is the splitting functions which are derived from the QCD [11].

## 2.2 Parton distribution function in nuclei

It has been known that the structure function in the nucleus ($AF_2^A$) is not identical to that in free nucleons ($F_2^p$) from several experiments [5], as shown in Fig 2.2. The dominant Nuclear effects each $x$ region are as follows.

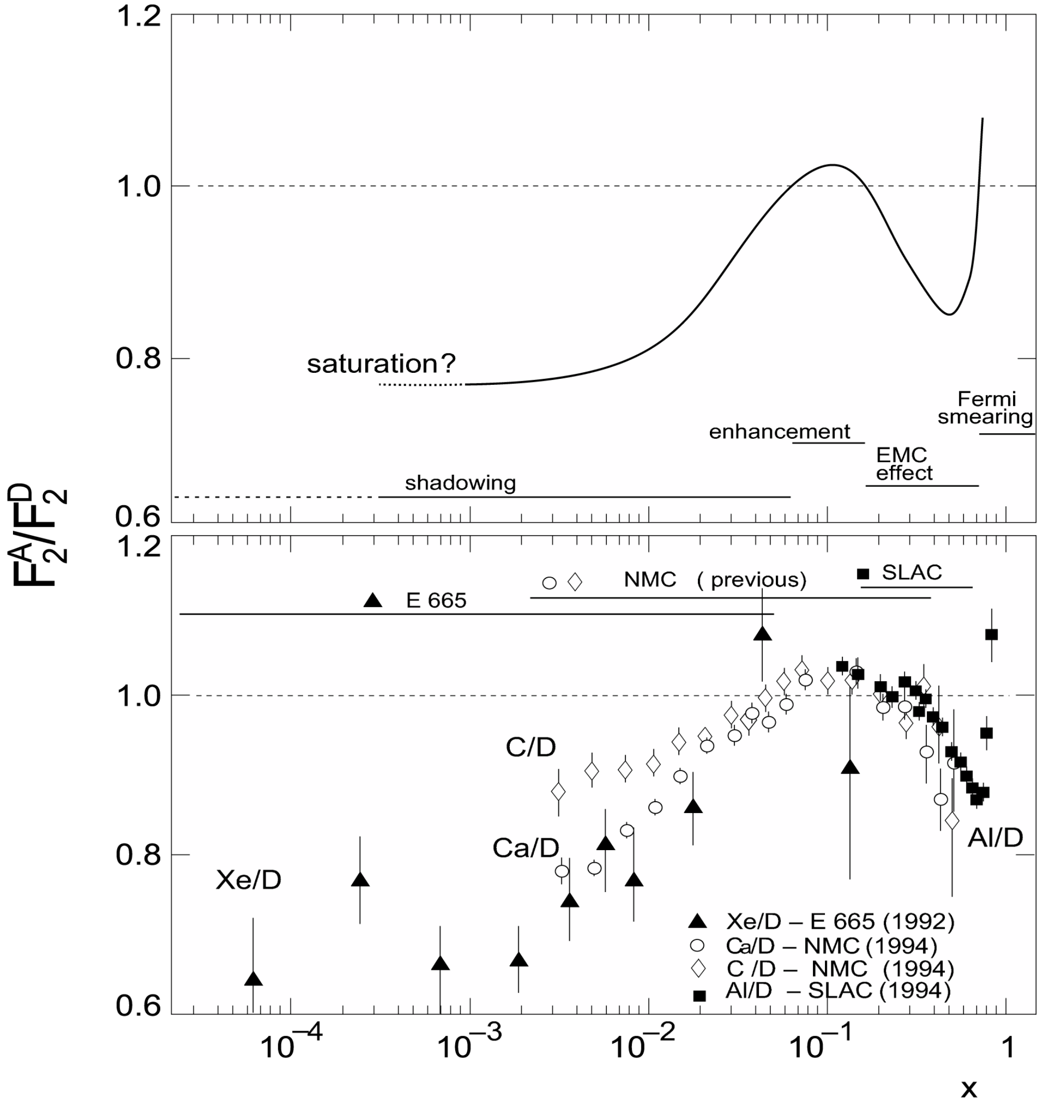

**Figure 2.2:** The ratio of $F_2$ structure functions of various nuclei to that of deuterium [5]

- $x \sim 1$: Fermi motion enhances scattering around the limit.
- $0.3 \le x \le 1$:The decrease is at first discovered by the EMC exp, and hence called EMC effect. The origin is still discussed.
- $0.03 \le x \le 0.3$:The enhancement in this region is often referred as anti-shadowing. The origin is still discussed.

- $x \leq 0.03$:At low-$x$ $R_A$again become less than 1. The origin is still discussed.

One convention to relate the PDF of nucleon and nuclei is to introduce the nuclear modification factor ($R$), defined as

$$q_i^A(x,Q^2) = AR_i^A(x,Q^2)q_i^p(x,Q^2), \tag{2.13}$$

where $q_i$ is the PDF of the $i$th species of quarks or $g$ for gluons. Any deviation from $R=1$ is regarded as nuclear effects.

As seen in Fig. 2.2, shadowing of $F_2$ is experimentally well established. However, there are no well accepted background theory. Since gluon has no charge so that can't be probed directly via DIS or DY at lowest order, gluon PDF of the nuclei remains largely unknown.

Various theoretical models of $R_{F_2}$ and $R_g$ are shown in Fig. 2.3. They are based on DIS and DY experiments and DGLAP equation. At $x$~0.01, $R_{F_2}$s have almost same values, on the other hand, $R_g$s have a wider range.

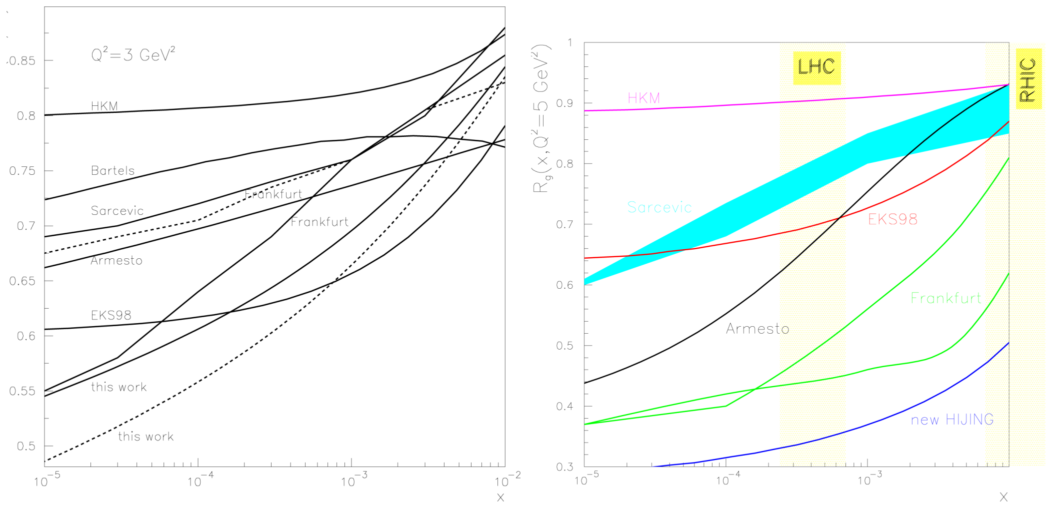

**Figure 2.3:** Left:$F_2$ ratios for Pb versus $x$ at fixed $Q^2 = 3$ GeV$^2$ from various models [12, 13, 14, 15, 16, 17, 18, 19, 20, 21]. Ratios of gluon distribution functions for Pb versus $x$ from different models at $Q^2 = 5$ GeV$^2$ [12, 13, 14, 15, 16, 17, 18, 19, 20, 21]

Poor understanding of $R_g$ is due to the lack of the gluon sensitive measurements. In Fig. 2.3, only the middle point of various theoretical predictions are shown. For example, theoretical calculation and its error of $R_i$ in the EPS model [22] are shown in Fig. 2.4.

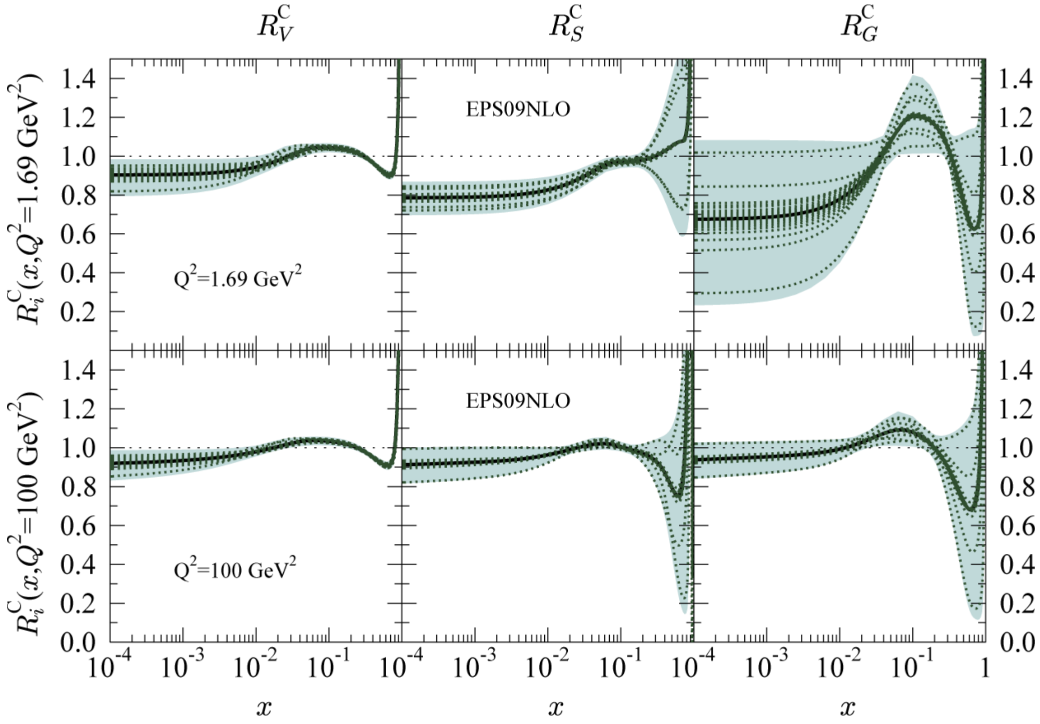

**Figure 2.4:** Theoretical calculation of $R_i$ [22]

## 2.3 $J/\psi$ production in ultra-peripheral collisions

To study parton distribution function of nuclei, photo-production process with ultra-peripheral collision (UPC) has attracted great interests for recent years. [23, 24, 25]. Ultra-peripheral means that the impact parameter of the collision is larger than twice the nucleus radius so that the two nuclei do not overlap with each other. A relativistically moving ion emits a quasi real photon with maximum energy $\sim \gamma/R$, where $\gamma$ is $\gamma$ factor of the nuclei and $R$ is the radius [26, 27]. At RHIC, the maximum energy of heavy ions with $\sqrt{s_{NN}} = 200$ GeV, energy of quasi real photons can reach about 3 GeV and the center of mass energy of $\gamma A$ system can be $\sqrt{s_{\gamma A}}=$ 34 GeV.

### 2.3.1 Cross section estimation in p+p collisions

The lowest order diagram of $J/\psi$ photo-production in Au+Au collisions is shown in Fig. 2.5. The two-gluon picture is applicable to the production of heavy vector mesons. On the simplest assumption, and in the simplest p+p or e+p collisions, the production cross section is expressed as follows.

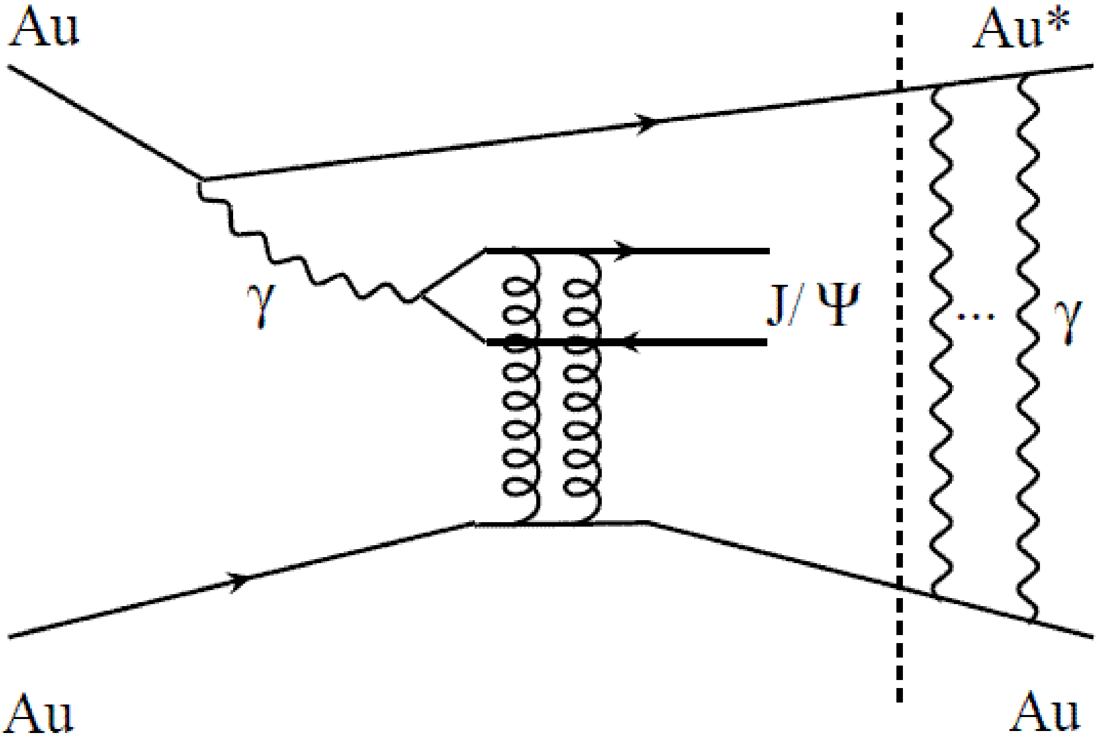

**Figure 2.5:** The diagram of $J/\psi$ production.

$$\frac{d\sigma}{dt}(\gamma^* p \to J/\psi p)|_0 = \frac{\Gamma_{ee} M^3_{J/\psi} \pi^w}{48\alpha} \frac{\alpha_s(\bar{Q}^2)^2}{\bar{Q}^8} [xg(x, \bar{Q}^2)]^2 (1 + \frac{Q^2}{M^2_{J/\psi}}), \tag{2.14}$$

where $\Gamma_{ee}$ is the electronic width of the $J/\psi$ , $M_{J/\psi}$ is the rest mass of $J/\psi$ , $\bar{Q} = (Q^2 + M^2_{J/\psi})/4$, and $x = 4\bar{Q}^2/W^2$ [28]. Therefore, the photo-production cross section is proportional to the square of gluon density. It shows that the cross section can be a sensitive to the gluon PDF of nuclei.

### 2.3.2 Cross section estimation in A+A collisions

To estimate UPC $J/\psi$ cross section in A+A collisions, there are two major approaches.

#### Collinear approach

Collinear approach is based on Eq. 2.14 and nuclear PDF (nPDF). The nPDF is $R_A$ modified PDF. Some of theorists estimate cross section of UPC $J/\psi$ +Xn (with neutron emission) in RHIC with this approach [29]. The detail of neutron tagging is discussed later. The theorist used the nuclear breakup probability, 0.64 (64% of UPC $J/\psi$ events are associated with at least a neutron). This is higher than that of the assumed values in the PHENIX previous measurement, 0.55 [30, 31]

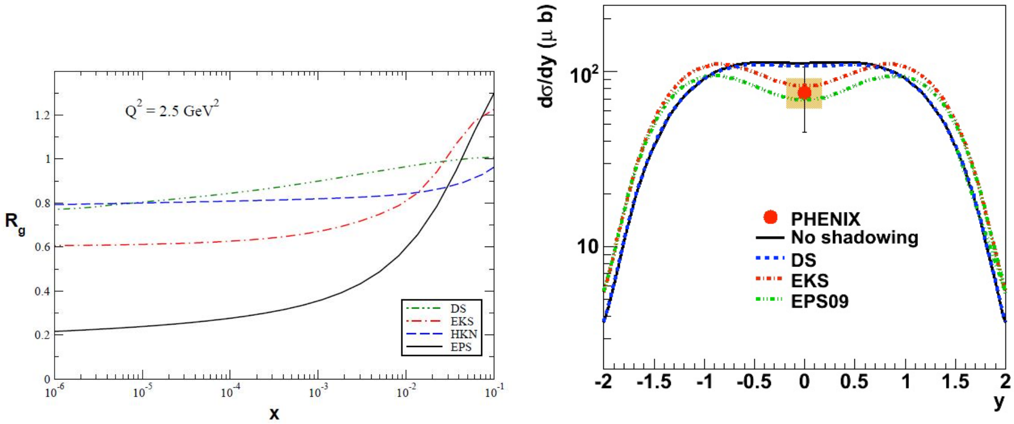

**Figure 2.6:** Left:Theoretical prediction of $R^g_{Au}$. Right:2004 UPC $J/\psi$ $+XN$ result with theoretical predictions [30, 29, 32, 33, 34, 22].

#### Color dipole approach

The basic idea of this approach is that photons can take vector meson state, virtually [35]. In the target frame, $\gamma A$ scattering can be taken as vector meson + nuclei collisions.

In the framework, lifetime of virtual photon in VM state:

$$\Delta t = 1/\Delta E, \Delta E = E_{VM} - E_{\gamma *} = \sqrt{M^2_{VM} + p^2_\gamma} - \sqrt{q^2 + p^2_\gamma} \sim \frac{M^2_{VM} + Q^2}{2p_\gamma} \qquad (2.15)$$

where $E_{VM}$ and M$_{VM}$ are energy and mass of vector meson, $E_{\gamma *}$ and $p_\gamma$ are energy and momentum of virtual photons. Then,

$$c\Delta \sim \frac{2p_{\gamma}}{M_{VM}^2 + Q^2} >> R_A \tag{2.16}$$

Vector meson states live long enough to interact several times in the nucleus. The leading twist (LT) order contribution is taken as an origin of the shadowing in the theorem. The diagram of LT contribution and $\gamma p$ diffractive process are shown in Fig. 2.7 [36, 37]. These diagrams are closely related. Therefore, shadowing effect is related to the $J/\psi$ and nuclei cross section, $\sigma_{J/\psi N}$, and it can be estimated diffractive PDF from HERA data.

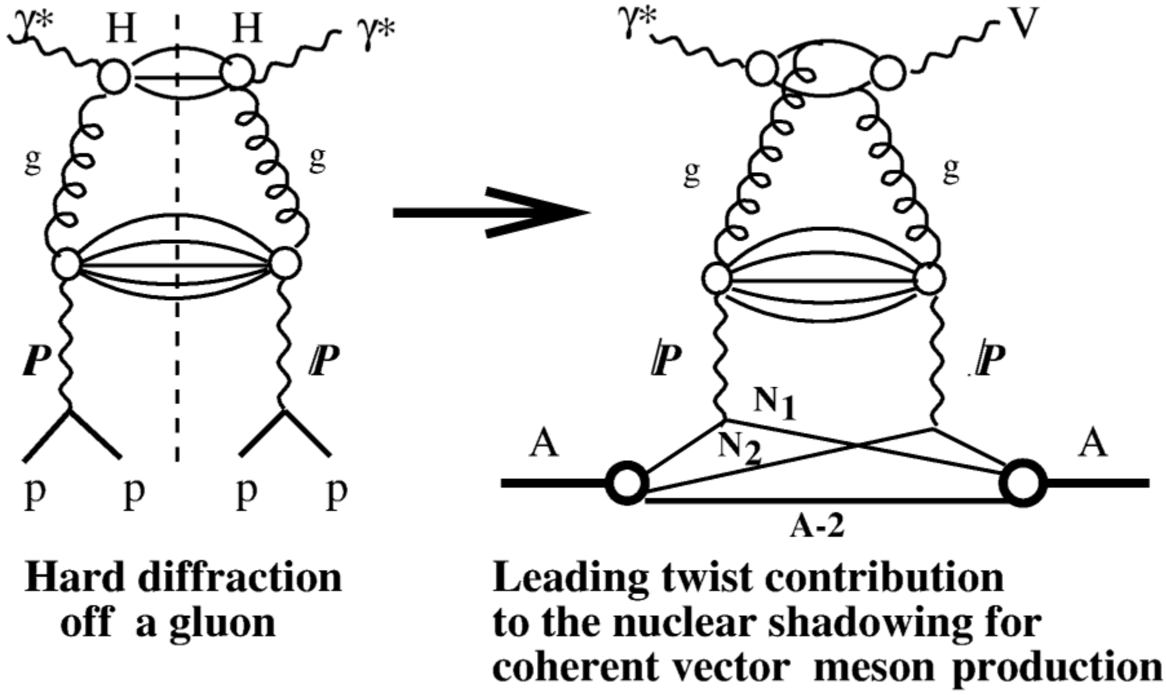

**Figure 2.7:** The diagram of LT contribution and $\gamma p$ diffractive process [36].

In both approaches, UPC $J/\psi$ cross section reflects gluon dynamics in nuclei, therefore the measurement plays important role to study low $x$ QCD.

### 2.3.3 Physical processes in UPC at RHIC energy

In the RHIC energy region, the following three processes are expected to be competitive in the UPC.

- Coherent $J/\psi$ production ($\gamma Au \rightarrow J/\psi + Au$): The $\frac{d\sigma}{dp_T}$ distribution will have a very narrow peak at $t \leq 0.015$ GeV$^2$, because higher momentum transfer is suppressed due to the nuclear form factor.
- Incoherent $J/\psi$ production ($\gamma N \rightarrow J/\psi + Au^*$): The collision is assumed as $\gamma$ and one of nucleon in the nuclei collision. The $\frac{d\sigma}{dp_T}$ distribution will have a wider shape than the coherent case.

- In addition, as a background , a lepton pair is produced via a two photon process ($\gamma\gamma \rightarrow ll$):Especially, in the mid-rapidity region, $\gamma\gamma \rightarrow e^{+}e^{-}$ can be the main background source.

### Forward neutron emission

The photons to the right of the dashed line are soft photons that may excite the nuclei in Fig. 2.5. A Coulomb excitation leads to emission of neutrons in the very forward direction. PHENIX can make triggers only for UPC $J/\psi$ events with neutrons $+Xn$ (detail is discussed in the Chap. 4).

In coherent UPC case, $J/\psi$ production and neutron emission are independent. It means that neutron tagging does not introduce any biases in the extraction of exclusive $J/\psi$ cross section from these events. On the other hand, in incoherent case ($\gamma N \rightarrow J/\psi + Au^{*}$), the nucleon will be recoiled. The recoiled nucleon with the residual nucleus react and emit neutrons, $N + (A-1) = C_i + kn$ [38].

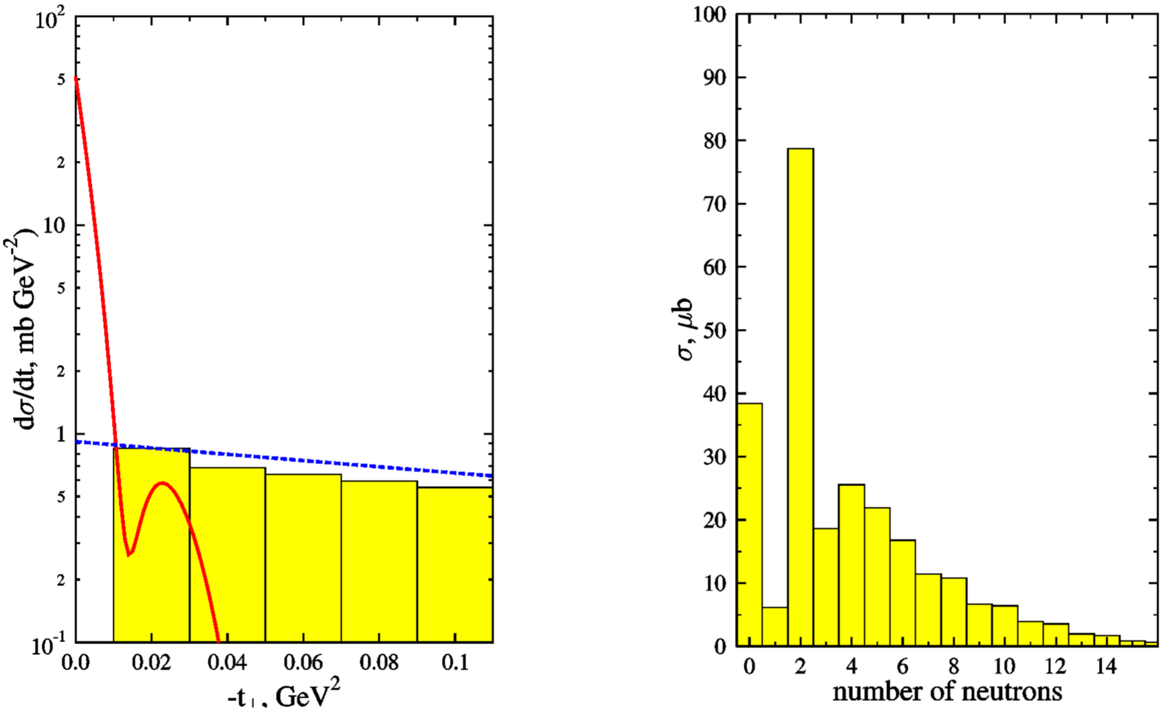

**Figure 2.8:** Left:Theoretical prediction of Integrated over rapidity ($|y| < 3$) the momentum transfer distributions for the $J/\psi$ in the coherent (solid line) and incoherent (dashed line) photoproduction in UPC of Au ions at RHIC [38]. Right:Theoretical prediction of incoherent UPC $J/\psi$ number of emitted neutron distribution without any trigger requirement at $\sqrt{s_{NN}} = 200$ GeV [38].

In this analysis in forward rapidity, both side neutron tagging is required (detail is discussed in Chap. 6). Only Strikman [39] made a prediction for $XnYn$ tagging UPC $J/\psi$ at RHIC. Figure 2.9 shows the prediction.

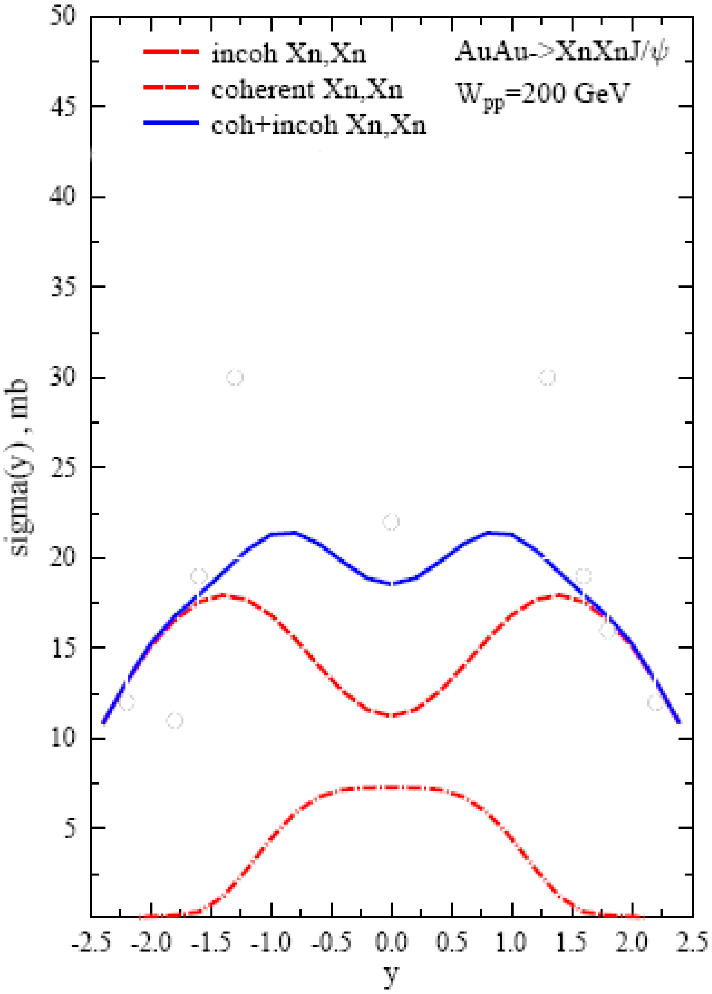

**Figure 2.9:** Theoretical prediction of UPC $J/\psi$ cross section distribution with any trigger requirement at $\sqrt{s_{NN}} = 200$ GeV. Black dots are old preliminary result, they can be ignored.

### 2.3.4 Previous PHENIX UPC $J/\psi$ result and predictions

PHENIX already published combined $\frac{d\sigma}{dy}$ of $J/\psi$ $+Xn$ at $|\eta| < 0.35$ with the data taken in 2004 [30] with $L_{int}$= 121 $\mu\text{b}^{-1}$. Clear $J/\psi$ peak can be seen, and the number of $J/\psi$ is $9.0 \pm 4.0 \pm 1.0$. As shown in Fig 2.10, the result is consistent with many predictions within its statistical error. Since there is low statistics, the previous result is coherent and incoherent combined result. Following thoretical models are presented in Fig 2.10.

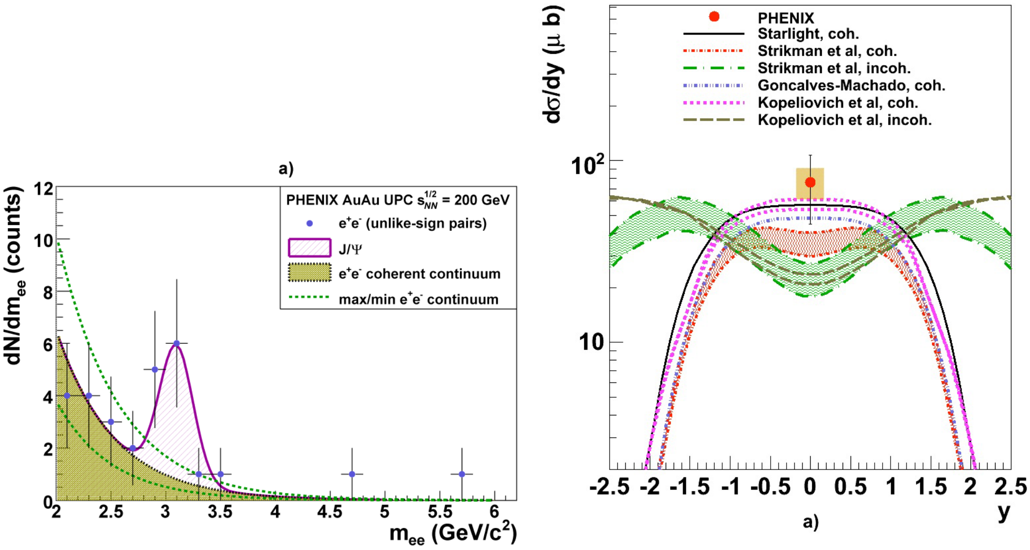

**Figure 2.10:** Left:$dN/dm_{ee}$ distribution fitted to the combination of a dielectron continuum (exponential distribution) and a $J/\psi$ (Gaussian) signal at $\sqrt{s_{NN}}$ =200 GeV in the 2004 PHENIX run [30]. Right:2004 UPC $J/\psi$ $+XN$ result with theoretical predictions [30, 40, 38, 41, 42, 43].

- STARLIGHT : Just for comparison, parameterize to HERA data [40].

- Strikman: Leading twist order shadowing, $\sigma_{J/\psi N}$ is assumed to 3 mb [38].

- Kopeliovich:Leading twist order shadowing, the dipole cross section is treated as a function of $r_t$, $\sqrt{s}$, where $\sqrt{s}$ is the center of mass energy, and $r_T$ is the transverse $q\bar{q}$ separation. Calculations were performed with KST and GBW parameterizations for the dipole cross section, [41].

- Goncalves-Machado: Gluon saturation is assumed [42].

In the figure, based on STARLIGHT [31], theoretical curves are modified with the nuclear breakup probability, 0.55.

# Chapter 3

# Experimental setup

Experimental set up of RHIC PHENIX are presented in the chapter.

## 3.1 Relativistic Heavy Ion Collider (RHIC)

The RHIC is the first heavy ion collider in the world. The basic parameters of RHIC in heavy ion runs are shown in Fig. 3.1.

Its maximum center of mass energy per nucleon pair is $\sqrt{s_{NN}}$ = 200 GeV. It can also be operated with proton-proton collision mode with $\sqrt{s}$ up to 500 GeV It started its operations in 2000 [44].

The schematics of the RHIC accelerator complex are shown in Fig. 3.1. The RHIC accelerator complex is composed of a Tandem Van de Graff, the proton linac, the booster synchrotron, the Alternating Gradient Synchrotron (AGS), and the RHIC rings. STAR [45] and PHENIX [46] are the main experiments at RHIC and two small experiments (BRAMHS [47] and PHOBOS [48]) were conducted until 2012.

**Table 3.1:** The Basic spec of RHIC at heavy ion runs.

| | |
|---|---|
| Injection Energy | $\gamma$ =10.25 ($p$ = 9.5 GeV/$c$ /nucleon) |
| Storage Energy | $\gamma$= 107.4 ($p$ = 100.0 GeV/$c$ /nucleon) |
| Peak Luminosity | $30\times10^{26}$ cm$^{-2}$/s |
| Ions/Bunch | $1.1\times10^{9}$ |
| Number of bunches | 111 |
| Emittance | 17$-$35 $\mu$m |
| Interaction diamond length (maximum) | 20 cm |
| Crossing angle, nominal (maximum) | 0(<1.7) mrad |
| Bunch length | 15 cm |
| Bunch radius | 0.2 mm ($\beta^{*}$= 1) |
| Luminosity life time | 3 hours |

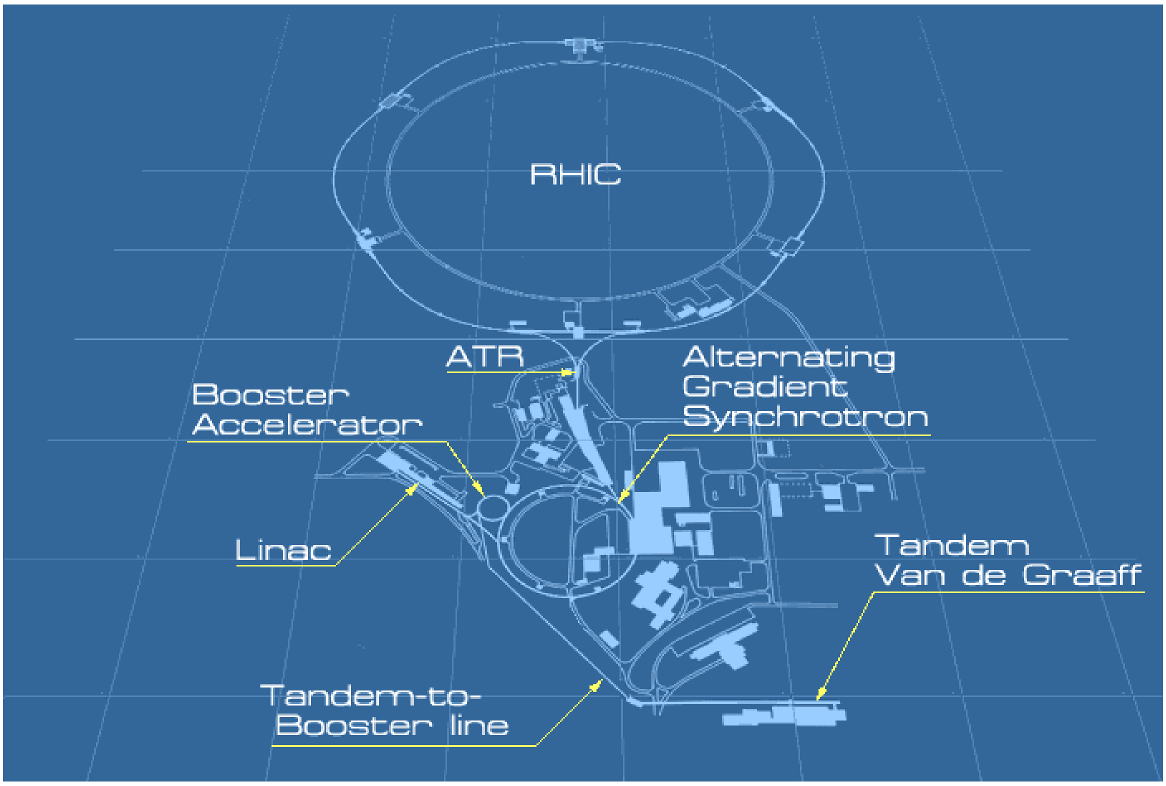

**Figure 3.1:** The figure is the map of RHIC.

### 3.1.1 Acceleration process of heavy ions

Acceleration starts from a pulsed sputter ion source. In case of Au beam, $\mathrm{Au}^-$ ions are created with a peak intensity 250 $\mu$A. The negative ions enter to the Tandem. They are accelerated with + 14 MeV potential. Passing through to a stripping foil at the terminal of high voltage, charged state are changed to $\mathrm{Au}^{12+}$. The ions are accelerated again to the end of the tandem. Another stripping carbon foils are set at the end, where the ions are changed to $\mathrm{Au}^{32+}$.

Secondly, the ions go to the booster. Its circumference is 200 m. Au ions being turned 45 times in the booster are grouped into six bunches. The energy per nucleon is 431 MeV at this stage. At the end of the booster, stripping foils change ions to $\mathrm{Au}^{77+}$. The ions are injected to the AGS and accelerated to 9.75 GeV. Finally, the ions go to the RHIC ring. At the AGS to the RHIC beam line, the ions become $\mathrm{Au}^{79+}$. The RHIC has yellow (counter clockwise) and blue (clockwise) rings. Injection is repeated 14 times to have 56 bunches in each ring. The ions are accelerated to the final energy $\sqrt{s_{NN}} = 200$ GeV in 130 seconds. A typical bunch has $1.1 \times 10^9$ ions. The minimum bunch crossing time is 106 ns.

## 3.2 Overview of the PHENIX detector complex

In the following sections, an overview of the PHENIX detector in the PHENIX 2007 and 2010 runs are described. The layouts of the PHENIX detector system in the 2010 and 2007 PHENIX runs are shown in Fig. 3.2. The definition of the PHENIX coordinate is shown in Fig. 3.3.

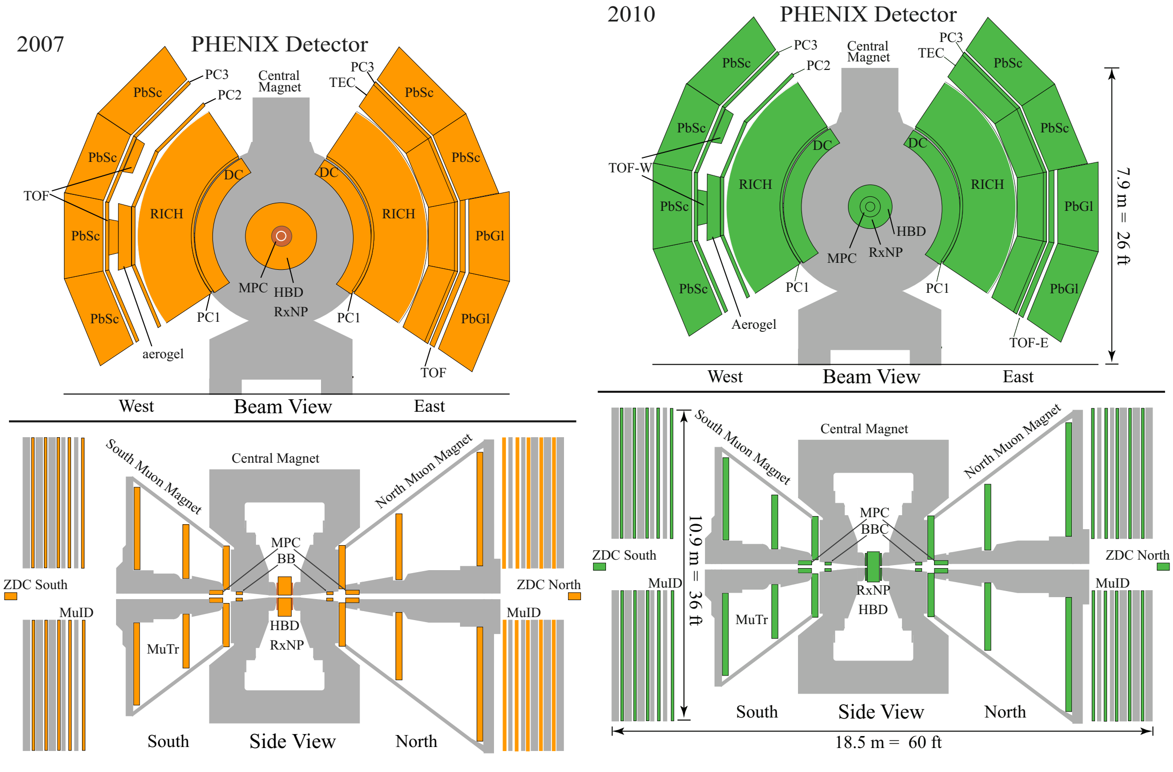

**Figure 3.2:** Left:The PHENIX beam (upper) and side (lower) view in the 2007 PHENIX run. Right:The PHENIX beam (upper) and side (lower) view in the 2010 PHENIX run.

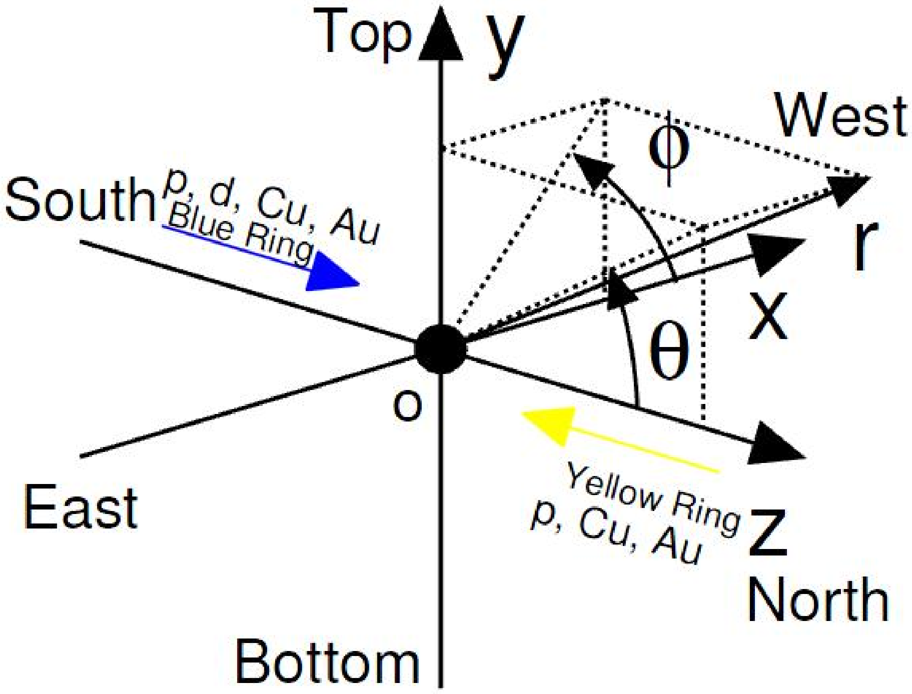

**Figure 3.3:** The definition of the PHENIX coordinate.

## 3.3 Beam Detectors

The PHENIX beam detectors are installed at forward and backward rapidity regions in the PHENIX experiment. Beam detectors consist of the BBC (Beam-Beam Counters) [49] and the ZDC (Zero-Degree Calorimeters) [50, 51, 52]. The main tasks of them are to measure luminosity and the collision vertex, event characterization such as an impact parameter called as collision centrality, and to make trigger and start time for the Time of Flight detectors.

### 3.3.1 BBC (Beam-Beam Counters)

The BBC is a device for the minimum bias trigger in the PHENIX. The BBC consists of two arrays of counter elements.Each BBC array has 64 modules. A module consists of 3 cm thick quartz as a Cherenkov radiator and 1 inch diameter mesh-dynode photomultiplie (Hamamatsu R6178). A module (a), an array (b), and the BBC mounted in the PHENIX detector are shown in Fig. 3.4.

They are installed in north side and south side of the PHENIX experiment, 1.44 m away from interaction point and cover 3.0< $|\eta|$ <3.9. The BBC is designed to measure the charged particle multiplicity and the timing. The timing information is converted to the collision point

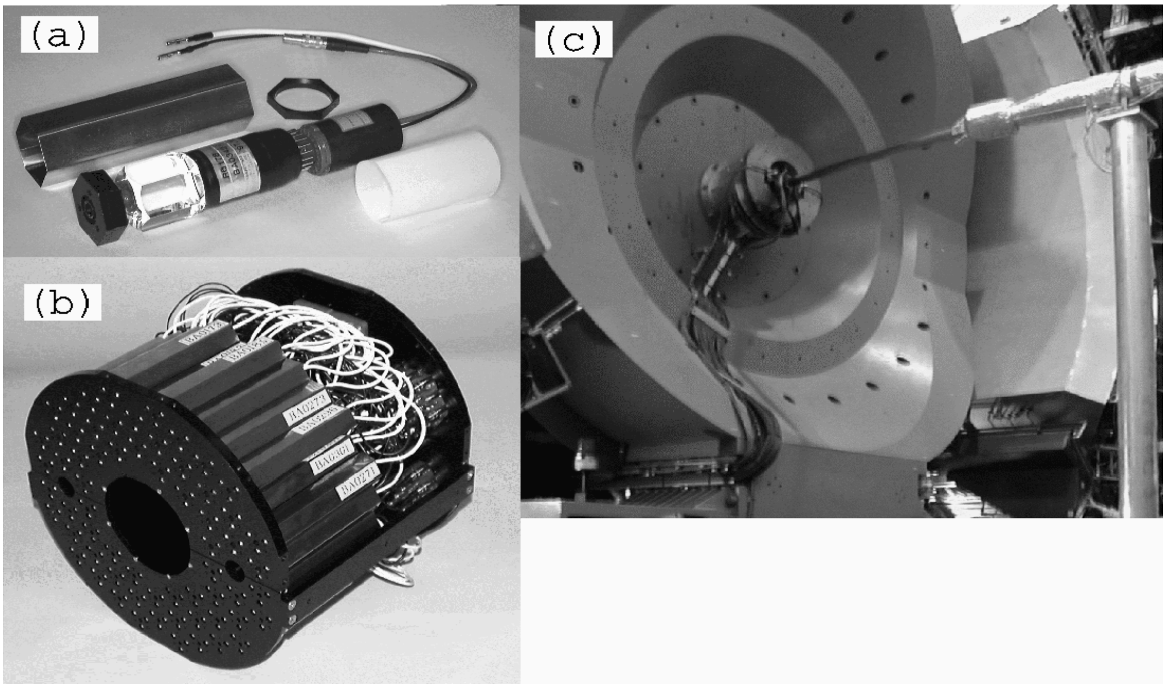

**Figure 3.4:** (a) single BBC. (b) A BBC array. (c)The BBC is mounted on the PHENIX beam pipe.

in $z$ direction (beam moving direction) by the following equation.

$$BbcZvertex = \frac{c \times (T_1 - T_2)}{2}, \tag{3.1}$$

where $T_1$ and $T_2$ are the incident timing which are measured by north and south BBC, $Z_{offset}$ is the calibration parameter. The measured resolution of a $z$-vertex is 6 mm (20 ps) in most central Au+Au collisions for BBC system. The intrinsic time resolution of one PMT elements is of the order of 100 ps.

### Luminosity

In PHENIX analysis, integrated luminosity $L_{int}$ was measured with the BBC with following:

$$L_{int} = \frac{N_{BBCLL1analyzed}}{\sigma_{AuAu} \times \epsilon_{BBC}}, \tag{3.2}$$

where $N_{BBCLL1analyzed}$ is the count of BBC trigger, $\epsilon_{BBC}$ is the efficiency of the BBC trigger and is measured to be 0.93, and $\sigma_{AuAu}$ is the total Au+Au cross section and is 6.85 b/.

## 3.3.2 ZDC (Zero-Degree Calorimeters)

The ZDC is a hadron calorimeter detect neutrons emitted at 0 degree. The ZDC is used as a trigger device of PHENIX. Same type of detectors is installed in STAR and the other experiments as well. As same as BBC, ZDC has two arrays and they are installed at frontward and backward of PHENIX collision point (±18.25m , $|\theta| < 2$mrad). The DX dipole magnets which are installed between the collision point and ZDC is shown in Fig. 3.5. Due to its magnetic field,only neutral particles are entered to the ZDC Each ZDC consists of three modules. The design of a module is shown in Fig 3.6. A module is a sandwich structureof PMMA fibers ($\phi$= 0.5 mm) and 5 mm-thick tungsten absorbers (27 plates). Each module has two interaction length. The angle between beam direction and the sandwich front planes is 45 degrees. The optical fibers are connected to phototubes (Hamamatsu R329-2).

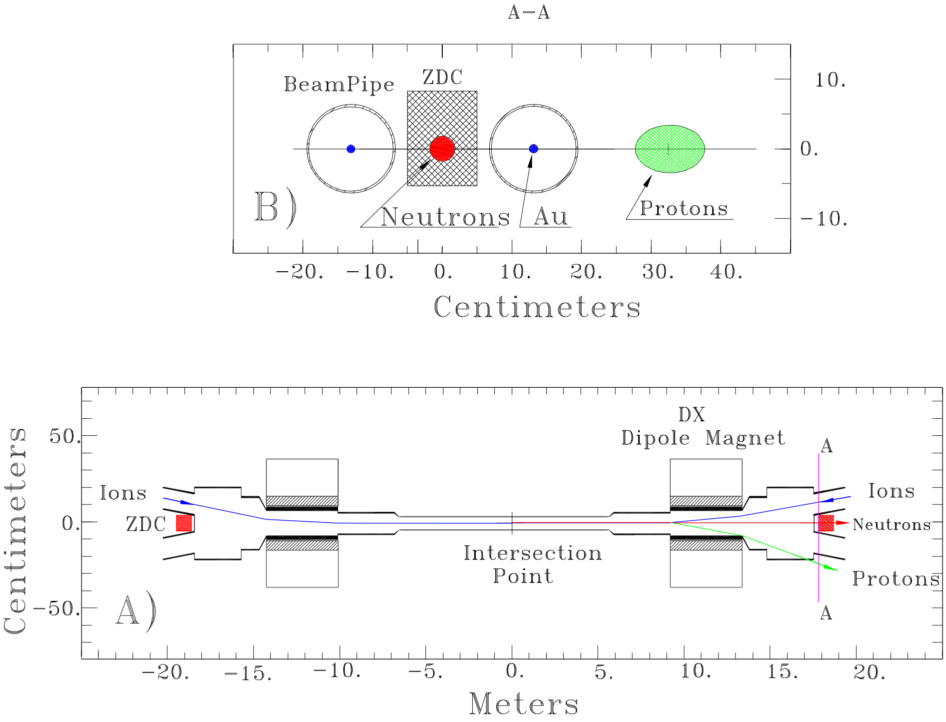

**Figure 3.5:** A:A top view of ZDC layout B:A beam view.

The energy resolution of the ZDC is 21% for 100 GeV neutrons.

The time resolution is about 120 ps. The resolution of vertex from the two ZDC is about 2.5 cm for one neutron with 100 GeV [50, 51, 52].

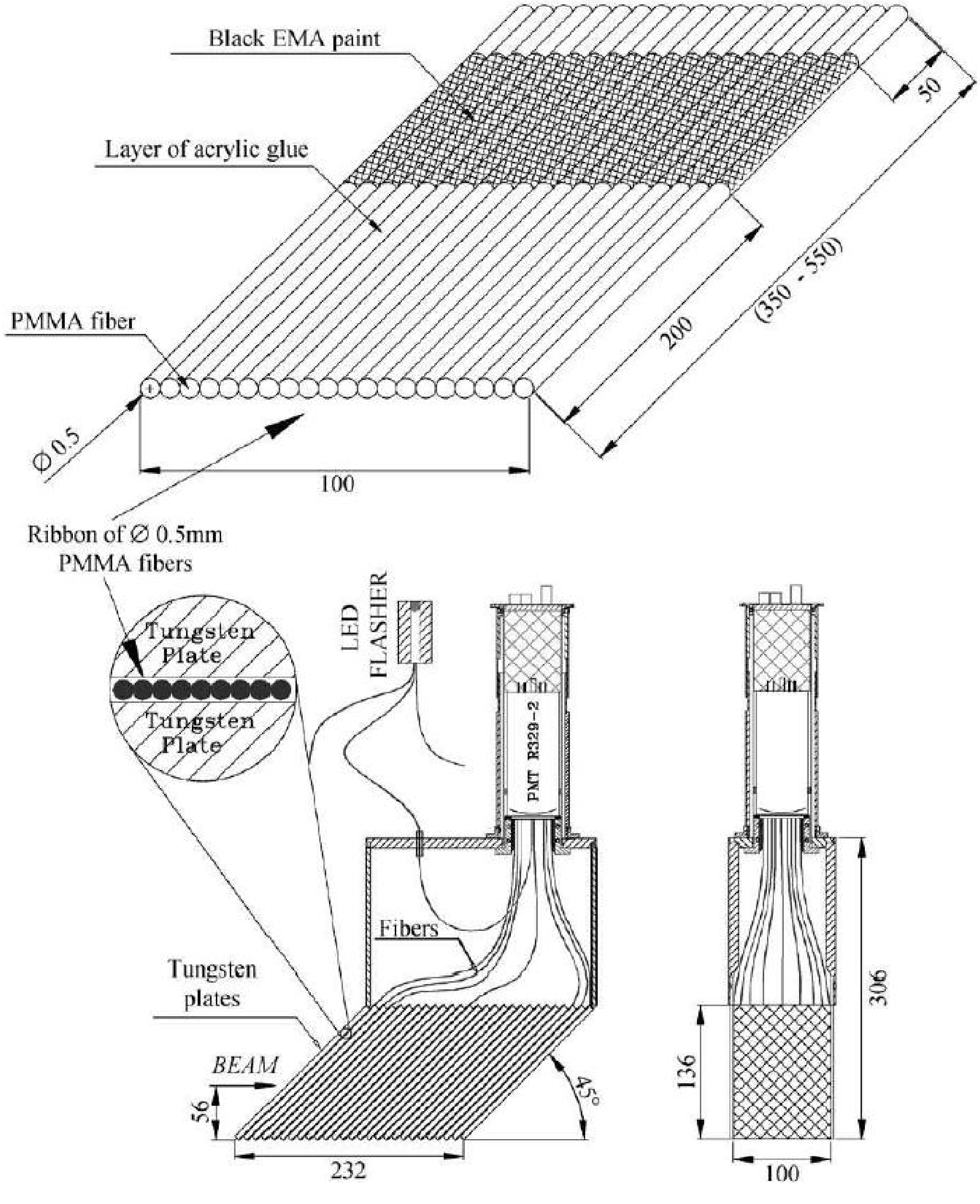

**Figure 3.6:** The ZDC inside schematic view.

### 3.3.3 Reaction Plane Detector (RxNP)

The RxNP is a pair of ring shaped scintillator installed at ($38 < |z| < 40$ cm) and ($1.0 < |\eta| < 2.8$). [53]. The main task of RxNP is to measure the charged particle multiplicity. Each RxNP separate to in 12 azimuth and two in the radial direction and hence has 24 units.

Each unit is composed of trapezoid shaped scintillator (BCF92), wavelength shifter, and photomultipliers (Hamamatsu R5924). The scintillator is perforated vertically by multiple light collecting optical fibers. The collected scintillation light output is read by one photomultiplier per slab. The photographs of RxNP are shown in Fig. 3.7, a) an uncovered scintillator unit, b) fully assembled sector (three units), and c) RxNP.

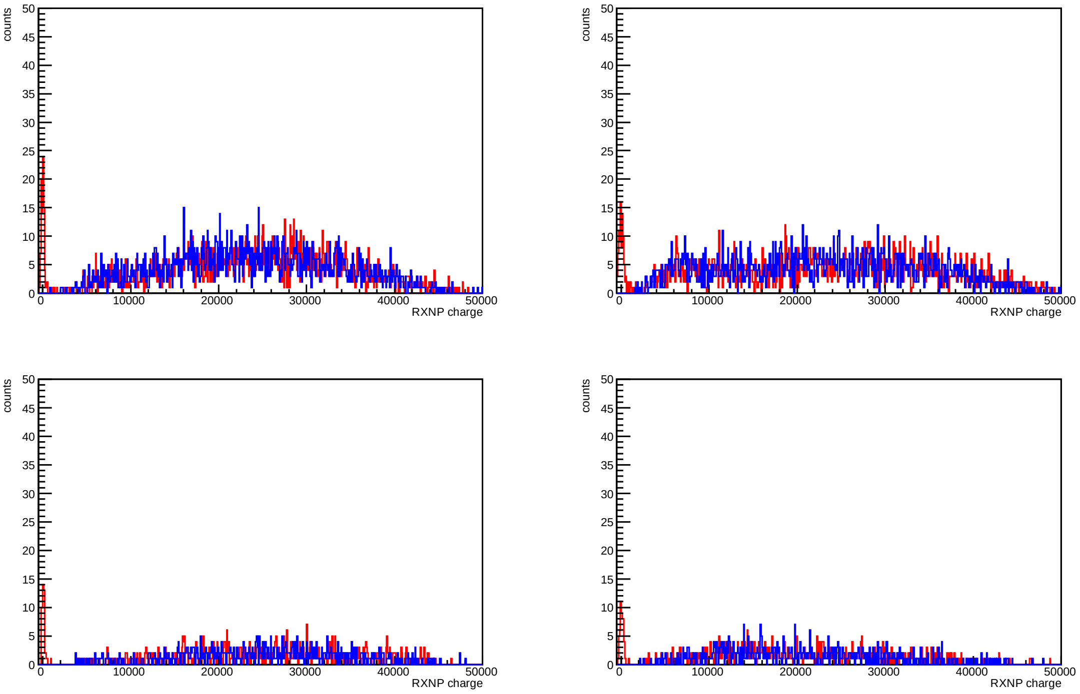

**Figure 3.7:** a) an uncovered scintillator unit, b) fully assembled sector (three units), c) RxNP

## 3.4 PEHNIX magnets

PHENIX has three magnets, Central, North Muon, and South Muon Magnets (CM, MMN, MMS) [54]. The layout is shown in Fig. 3.9

### 3.4.1 Central Magnets (CM)

As same as the central arm, CM covers $0.35 > |\eta|$.

CM is composed of inner and outer concentric coils. The two coils can be operated and run separately. PHENIX has three modes (CM+(outer only) , CM++, CM+−). The field integral

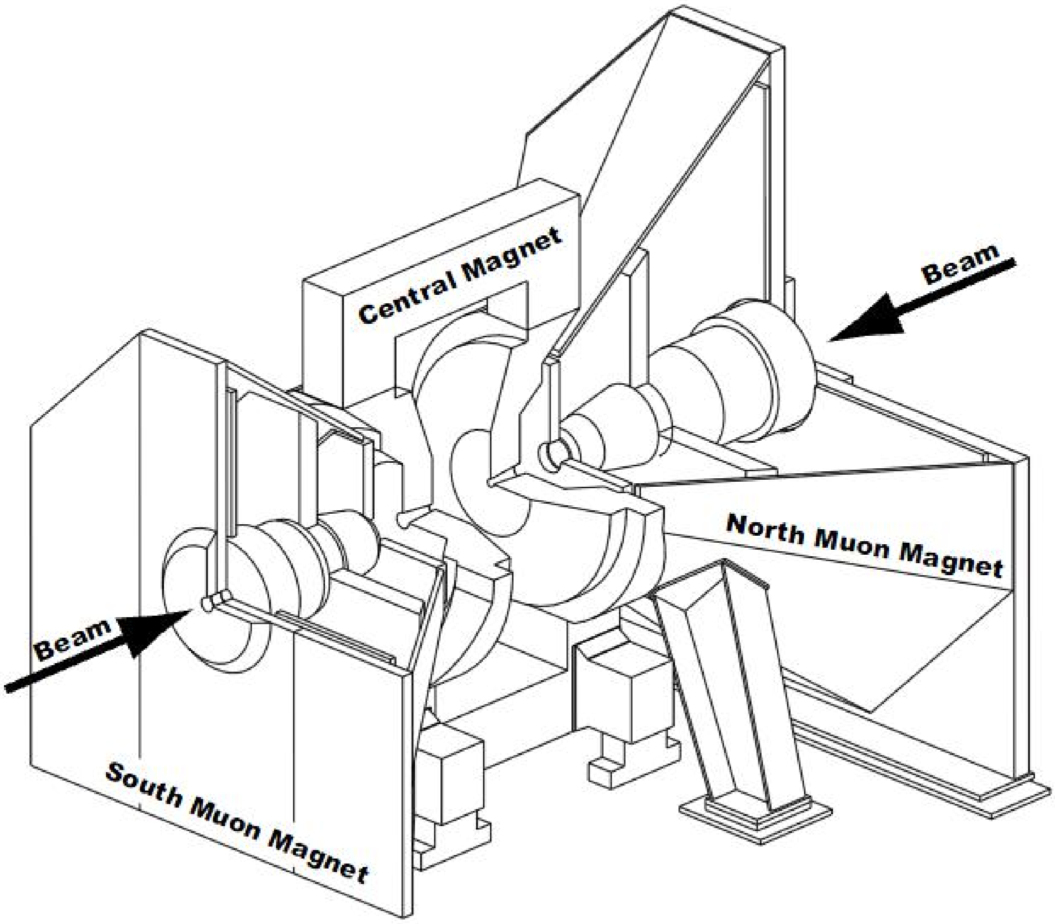

**Figure 3.8:** The layout of PHENIX magnet.

$\int B \cdot dl$ at $z = 0$ for each cases are 0.78, 1.04 and 0.43 T·m , respectively. In the 2007 PHENIX run, CM$+-$ was used. The field lines for in CM$+-$ case are shown in Fig 3.9.

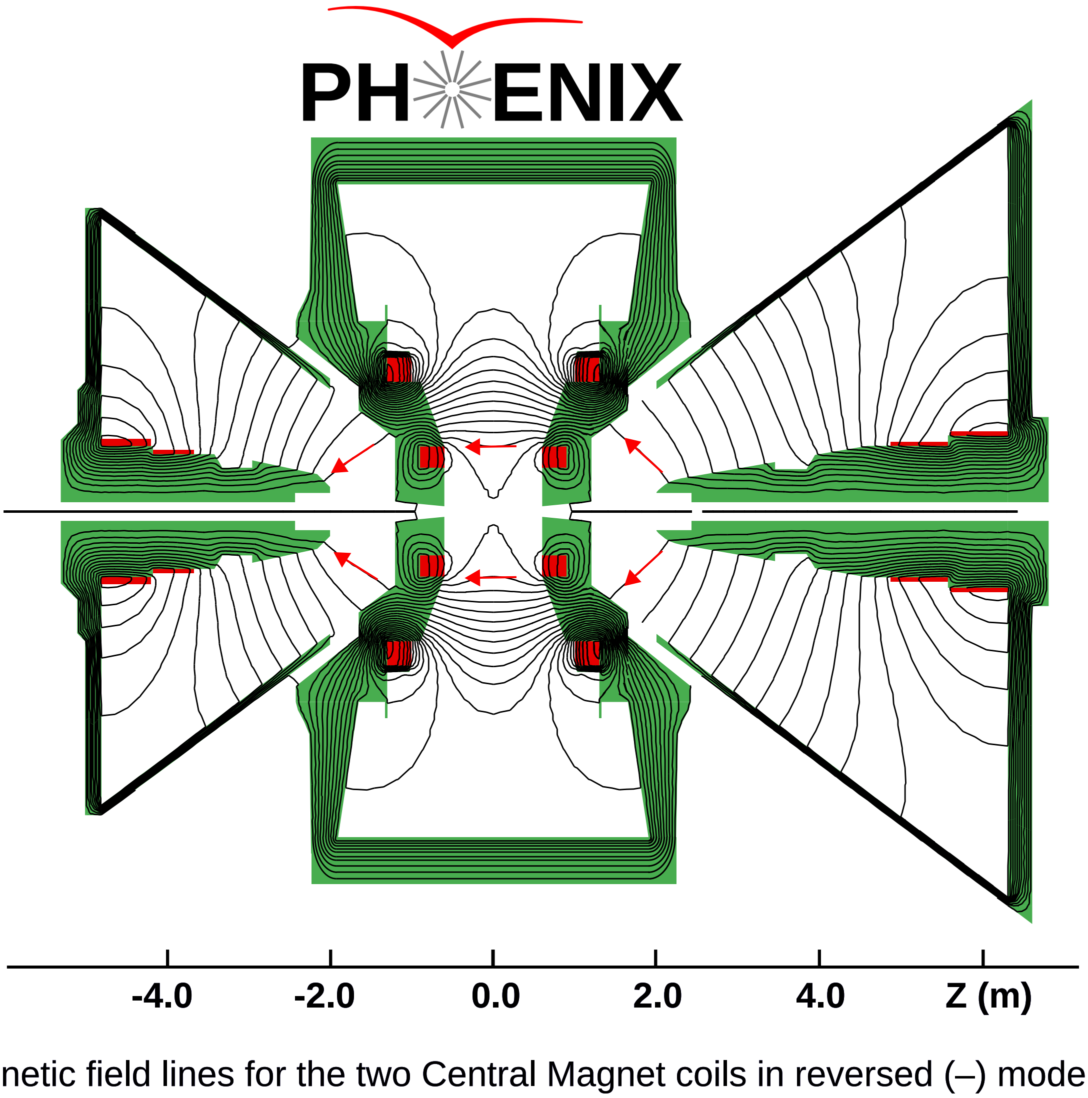

**Figure 3.9:** The mapping of PHENIX magnetic field for CM+- case.

### 3.4.2 Muon Magnets

Muon magnets (MMN and MMS) cover $1.1 < |\eta| < 2.4$ and $2\pi$ in azimuth. MMN and MMS consist of an eight lampshad and back planes. The field integral of each magnet is 0.72 Tm.

## 3.5 PHENIX detector system in central arm

The PHENIX central arm is divided into East and West arms. They cover $|\eta| < 0.35$, measure and identify hadrons, electrons and photons. The main tracking detectors in the central arm are the Drift Chamber (DC) and Pad Chamber (PC) [55]. The energy of a photon is measured by Electro Magnetic Calorimeter [56]. The Ring Imaging CHerenkov counter (RICH) and EMCal are used for electron identification. This section describes DC, PC, EMCal, and RICH.

### 3.5.1 Drift Chambers (DC)

The PHENIX Drift Chambers are the main tracking detector in the central arm. DC provides the position information of charged particles in ($\phi$) at the reference radius ($r$=220cm) and provides the information on the transverse momentum ($p_T$ ).

The frame of drift chamber is shown in Fig. 3.10. The length of DC in Z direction is 2.5 m and active area in $z$ is 1.8 m. DC covers $2.02 < r < 2.42$ m. The coverage in $\phi$ is 90 degrees and it is divided into 20 equal sectors (4.5 degree/sector). A sector of DC is shown in Fig. 3.11. There are six wire planes, which are called as X1, U1, V1, X2, U2 and V2 planes. The wires in X1 and X2 planes run in parallel to the beam axis. U1, U2, V1, and V2 are the stereo wire planes, which have the stereo angle of 6 degrees relative to X wires. U and V planes consist of four anode (sense) and four cathode wire planes. X plane consists of 12 wire planes. Typically the distance between planes in $\phi$ direction is $20-25$ mm . As shown in Fig 3.11 an anode plane has four type wires, sense (S), potential (P), gate (G), and back (B) wires. Their typical operation voltages are 4700, 2600, 2600, and 900 V, respectively. The P wires form a strong electric field and separate sensitive region created by sense wires. The G wires limit track sample length about 3 mm. The B wires have low potential and improve the gas gain control on the sense wires. The gas of DC is a mixture of Argon (50%) and ethane (50%). Simulated electrostatic lines are shown Fig 3.12.

Typical wire by wire gain is about 95 to 98 %. The order of gas gain is $10^4$.

The closest distance, $x$ , from an anode wire to the drift line can be described as follows.

$$x(t) = V_{dr}(x,t)(t - t_0), \tag{3.3}$$

where $V_{dr}$ is the effective drift velocity in the drift region, $t_0$ is the effective time at which the ionization occurred exactly on the anode wire. Working gas is chosen to have a uniform drift velocity in the active region. The $V_{dr}$ can be assumed as a constant, typically 5 cm/s. DC requires most frequently calibration, once per four hours. A typical Drift time distribution is shown in the right panel of Fig 3.12, $V_{dr}$ and $t$ are modified with the distribution.

DC can handle up to 500 tracks / events and double track resolution is 2 mm. The single wire resolution is 165 $\mu$m.

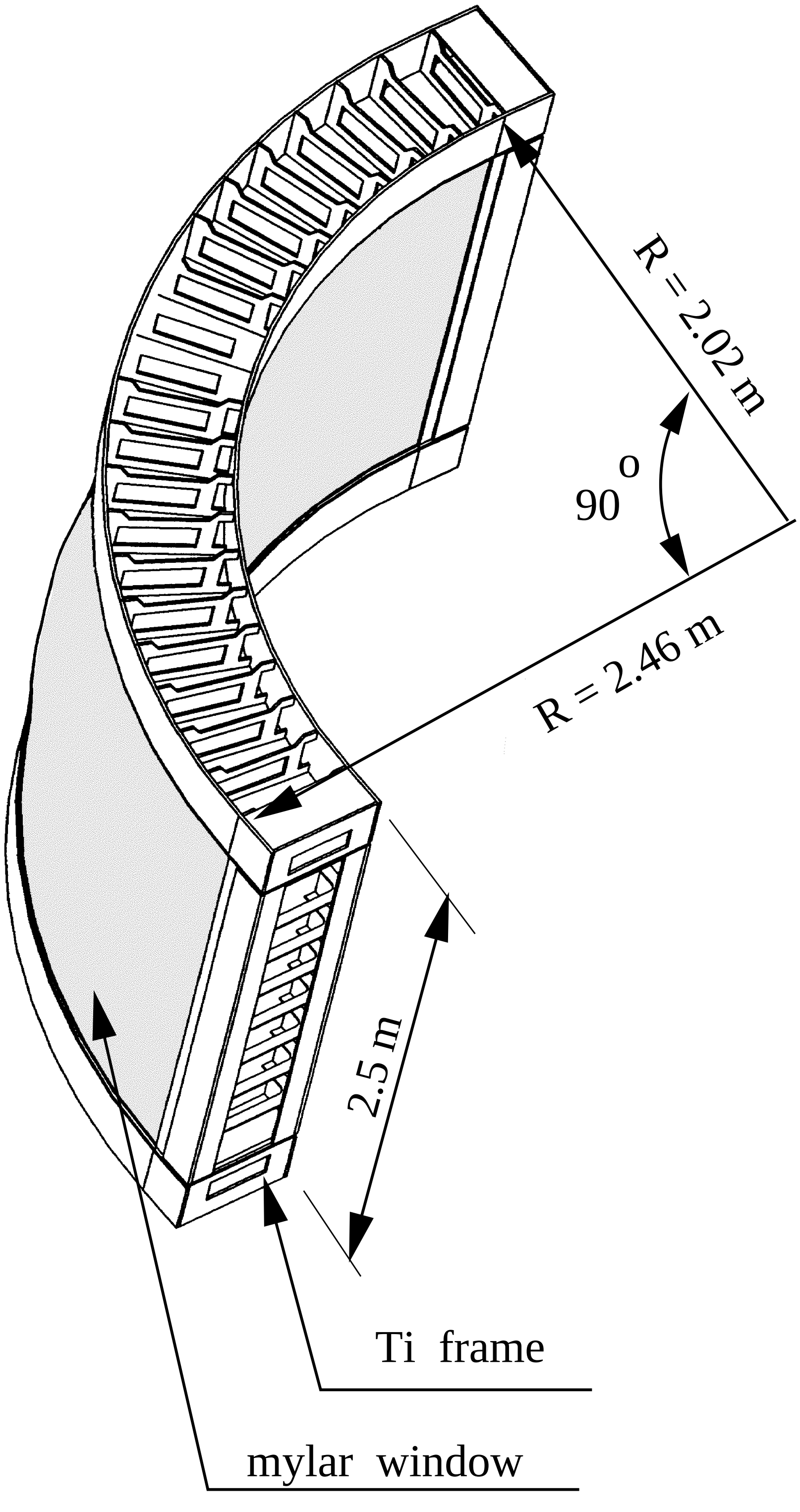

**Figure 3.10:** The frame of DC.

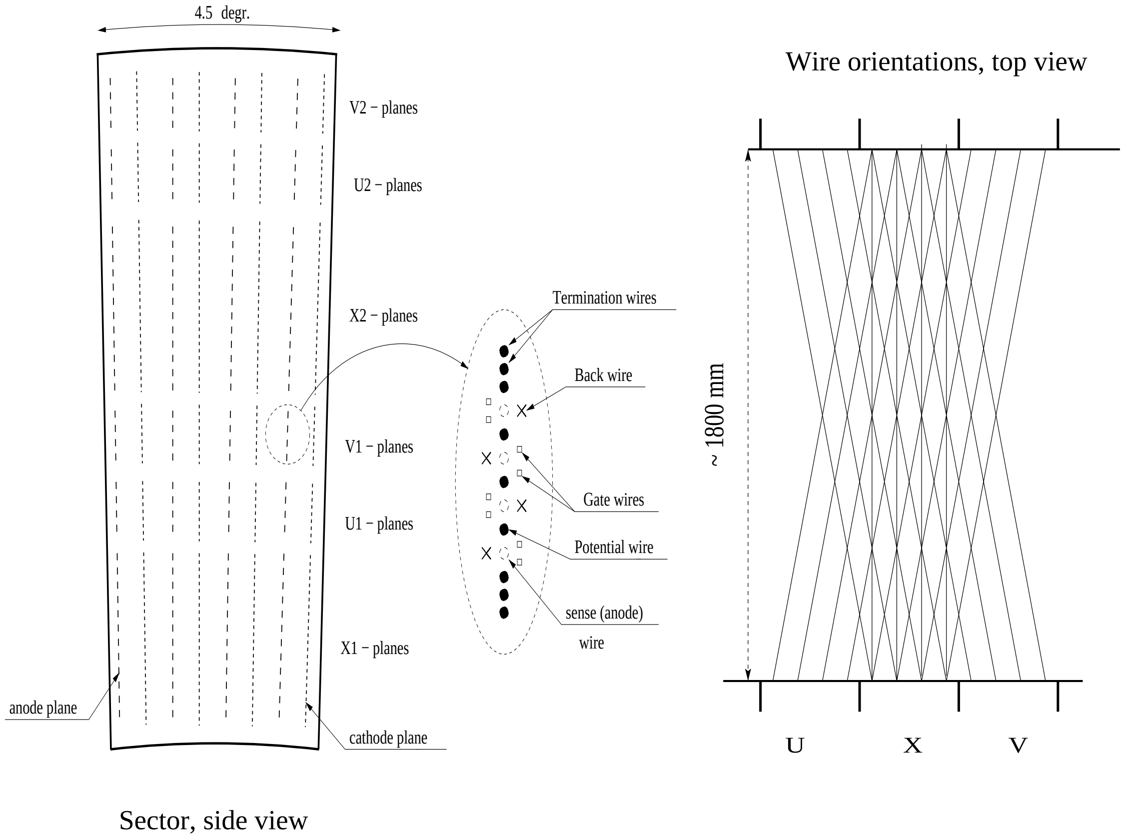

**Figure 3.11:** Left: The setup of DC wires in sector side view. Left: The setup of DC wires in sector top view.

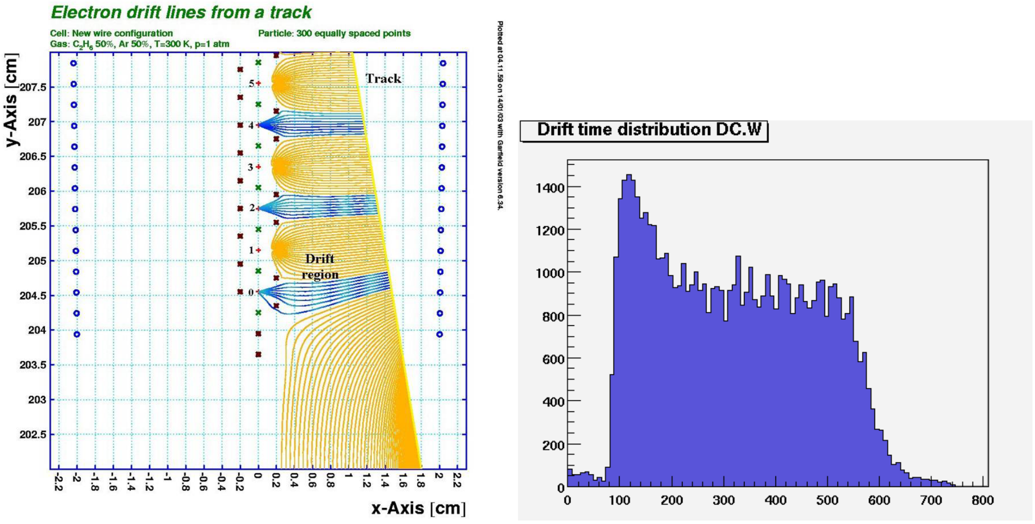

**Figure 3.12:** Left:Simulated electrostaic lines. Right:Typical Drift time distribution.

### 3.5.2 Pad Chambers (PC)

The pad chambers (PC) are multi-wire proportional chambers with pad read out. As shown in Fig. 3.13 PC consists of three layers PC1 ($r$ = 2.47−2.52 m), PC2 ($r$ = 4.15−4.21 m), and PC3 ($r$ = 4.91−4.98 m). PC1 and PC3 are installed in both West and East arms. However, PC2 is installed only in West arm. Each PC layer consists of a cathode plane, signal pad plane, anode and field wire planes. Pad plane consists of three layers. The schematic view is shown in Fig. 3.14. A pad which is made up nine pixels is shown in the left panel. As shown in the right panel, three pad layers cover full area. The gas of PC is a mixture of argon (50%) and ethane (50%) at atmospheric pressure. Specifications of PC layers are summarized in Tab 3.2 . The main function of PC is to perform three dimensional tracking and determine the particle momentum in beam direction $p_Z$. PC1 is installed behind DC. Ar/Ethane 50/50 flammable gas is used. The typical operation voltage of PC1, PC2, and PC3 are about 1700, 1800, 850 V. The typical gain is order $10^4$ PC2 and PC3 are used to reduce ambiguities in outer detectors.

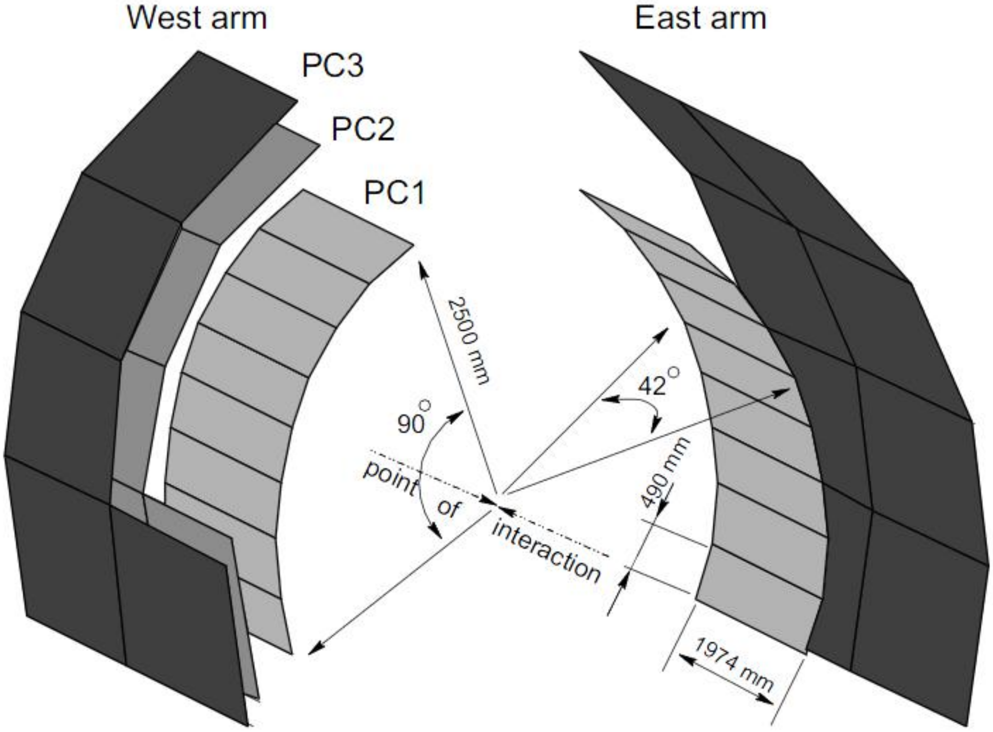

**Figure 3.13:** The layout of PC.

### 3.5.3 Ring Image CHerenkov detectors (RICH)

RICH is the main detector for electron identification [57]. RICH is installed in $2.5 < r < 4.1$ m in the West and East arm in PHENIX, as shown in 3.15. The inner of RICH is shown in Fig. 3.16. The RICH gas vessel is filled with $CO_2$. According to the $CO_2$ Chrenkov threshold $(\gamma_{th}) = 35$, only electrons and positrons can emit Cherenkov light up to 4 GeV/$c$ in $CO_2$ gas radiator. The Cherenkov light is reflected by the mirrors and detected by phototubes. The

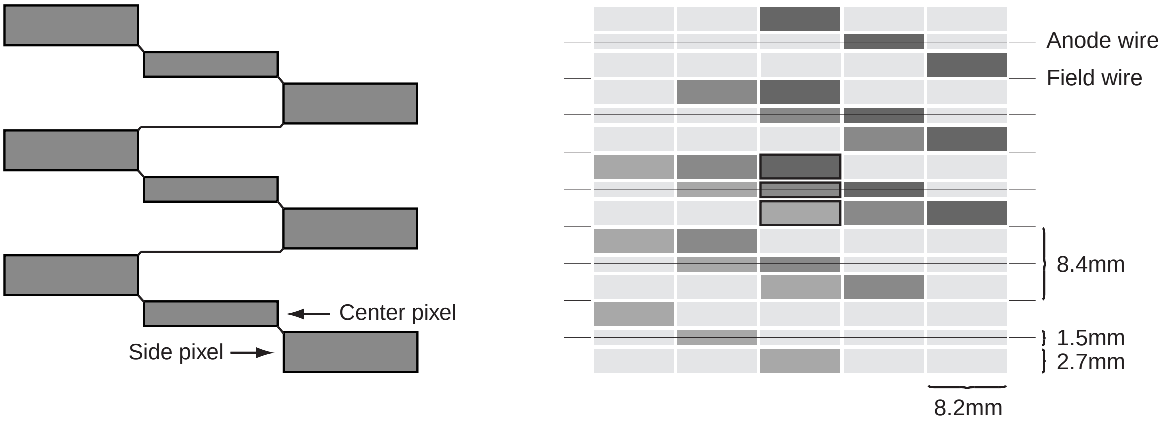

**Figure 3.14:** Left:The pixels of PC. Right the layesr of PC.

| parameters | PC1 | PC2 | PC3 |
|---|---|---|---|
| Pad size ($\phi \times z$) (mm$^2$) | 8.4×8.4 | 13.6×14.4 | 16.0×16.7 |
| Single hit resolution in z axis (mm) | 1.7 | 3.1 | 3.6 |
| Efficiency (%) | $\geq$99 | $\geq$99 | $\geq$99 |

**Table 3.2:** Parameters of PCs

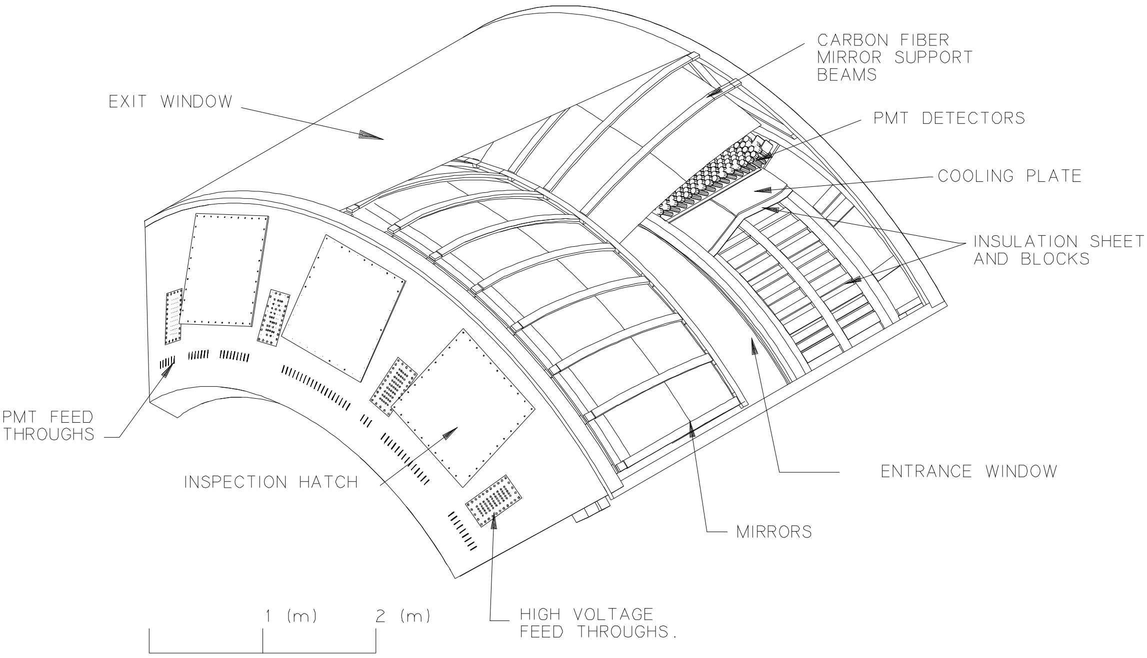

**Figure 3.15:** The figure schematic view of RICH.

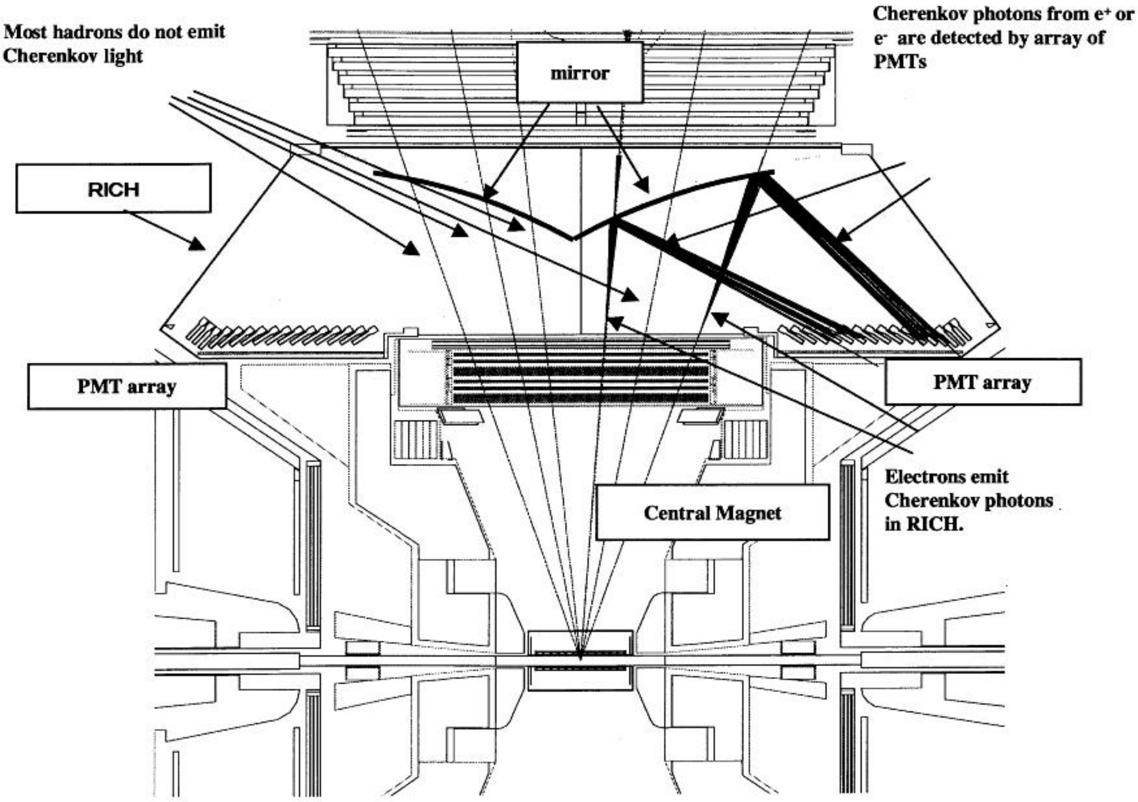

**Figure 3.16:** The schematic view of inside of RICH.

volume of each side RICH is 40 m$^3$, and its area of the entrance window is 8.9 m$^2$ and its area of the exit window is 21.6 m$^2$. Each side RICH has 48 composite spherical mirror panels forming two intersecting with sphere radius of 4.01 m. The size of each mirror panel is 0.812 $\times$ 0.432$-$0.505 m$^2$. Total area of the mirrors is 20 m$^2$. Each mirror shape is a thick piece of the sphere with a curvature with radius about 4.01 m. The mirror panels are made of 12.5 mm Rohacell foam with four layers of graphite epoxy on each side. The total thickness is 0.7 mm. The reflectivity of the mirrors are 83 % for 200 nm and are 90 % for 250 nm. The mirror focus Cherenkov lights into the PMT arrays, where 1280 PMTs are installed (H3171S UV photomultipliers). The quantum efficiency is about 5 % and 19% at the wavelength of 200 nm and 300 nm, respectively.

### 3.5.4 ElectroMagnetic Calorimeters (EMCal)

The main purpose of EMCal is to measure the energy and three dimensional position of electrons, positrons and photons. The East arm has four sectors of Lead Scintillator calorimeters (PbSc). The west arm has two sectors of PbScs and two sectors of lead glass calorimeters (PbGL). Each sector of PbSc and PbGl covers $\pi/8$ in azimuth.

#### Lead Scintillator Calorimeters

The PbSc is a shashink type sampling calorimeter. A schematic view of a PbSc module is shown in Fig. 3.17.

Each PbSc sector has 18 super modules. Each super module has 36 individual modules. A module consists of four towers, which is shown in Fig. 3.17.

Each PbSc tower has the depth of 66 sampling cells. Each cell consists of a Pb tile and a scintillator. 36 longitudinally penetrating wavelength shifting fibers connect these cells to 30 mm FEU115M phototubes. A module consists of four towers. Total covering area of the PbSc is about 50 m$^2$. There are total 15552 individual towers. The overall energy resolution to the electron was measured in the beam test and found to be

$$\frac{\sigma_E}{E} = \frac{8.1\%}{E(GeV)} \oplus 2.1\%. \tag{3.4}$$

#### Lead Glass calorimeters

A PbGL sector consists of 192 super modules and one super module consists of 24 individual modules as shown in Fig. 3.18. These 24 modules are glued together with carbon fibers and epoxy resin. Each module has 40×40×400 mm lead glass crystal. The thickness corresponds to 14 radiation length. The crystal is wrapped with aluminized mylar and shrink tube. Electrons and positrons created through the electromagnetic shower process emit Cherenkov photons in the crystal. The photons are read out by an FEU84 phototube. The overall energy resolution of PbGl tested by using electron beams is as follows.

$$\frac{\sigma_E}{E} = \frac{5.9\%}{E(GeV)} + \oplus 0.8\% \tag{3.5}$$

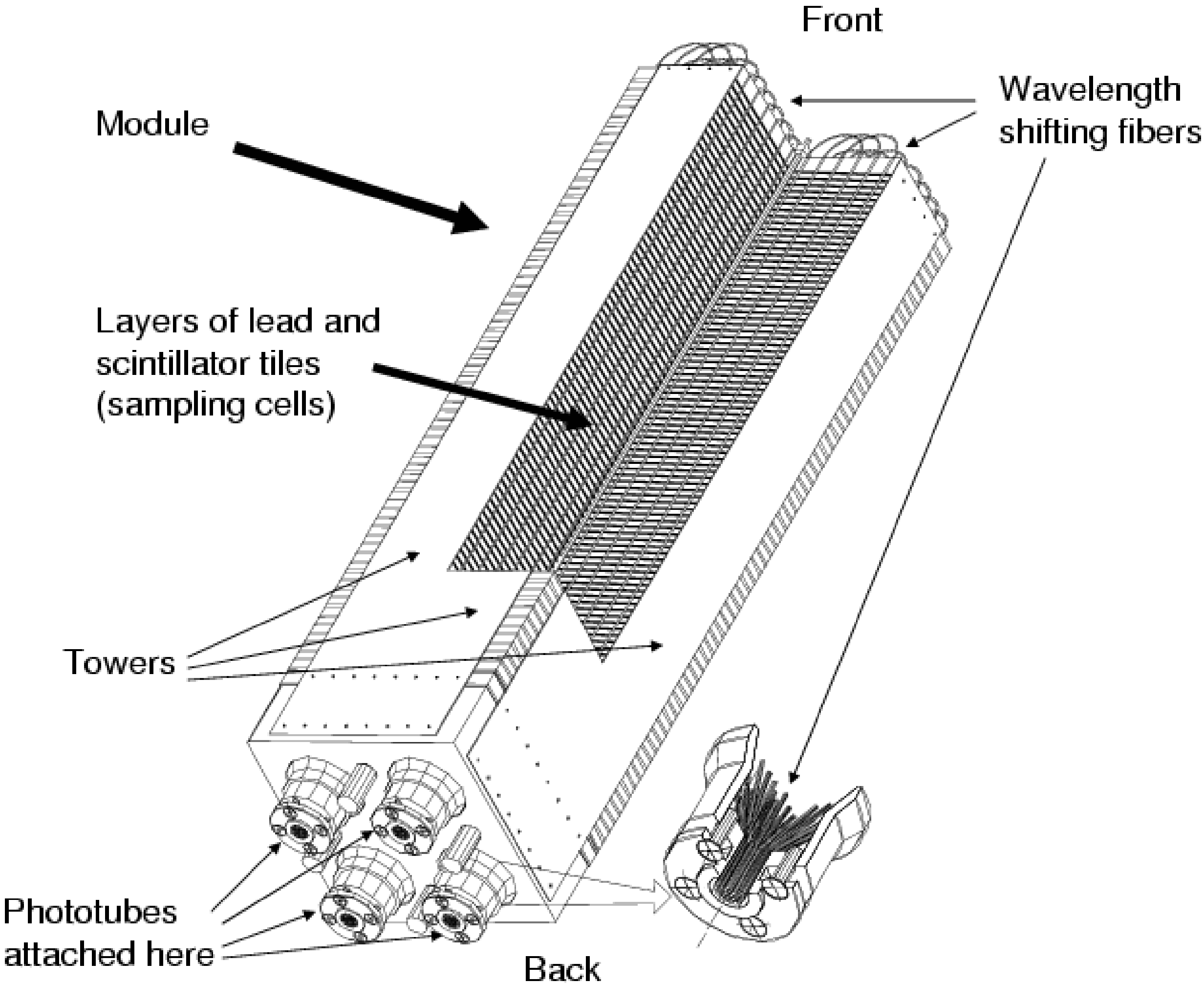

**Figure 3.17:** The schematic view of one module of PbSc.

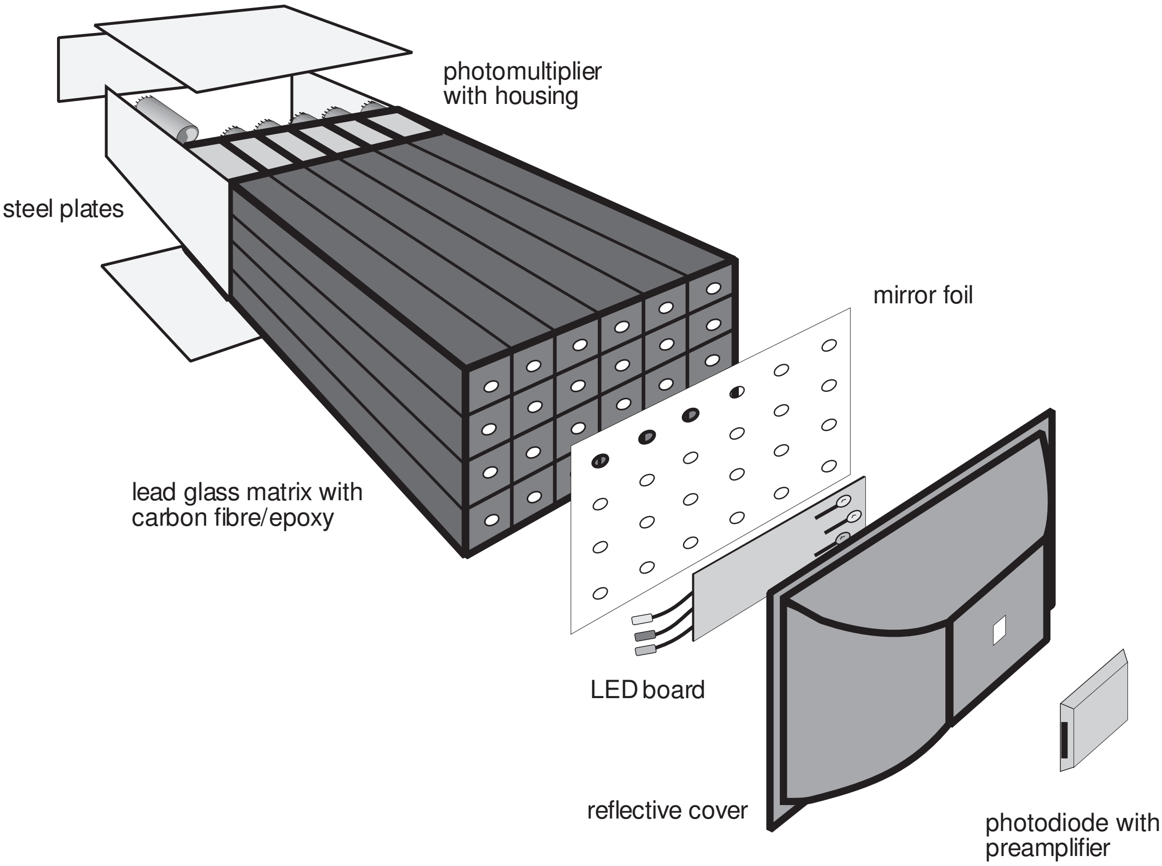

**Figure 3.18:** The schematic view of super module of PbGL.

## 3.6 Muon Arms

The main purpose of the PHENIX muon arms is to identify muons in the forward direction and to measure its momentum. There are two muons arms in PHENIX; The South and North muon arms. Both of them cover full azimuth and $1.2 < |\eta| < 2.4$ [58]. Since the location of the South and North muon arms is different in beam direction, the overall volume of the South and North muon arms is different.

Each muon arm consists of a hadron absorber (Cu), and two muon detectors (MuTr: muon tracker, MuID: muon identifier).

### 3.6.1 Hadron absorber

The interaction length of the south muon arms is shown in Fig. 3.19. A central magnet (Fe) and a nosecone (Cu) are placed in front of Muon arms.

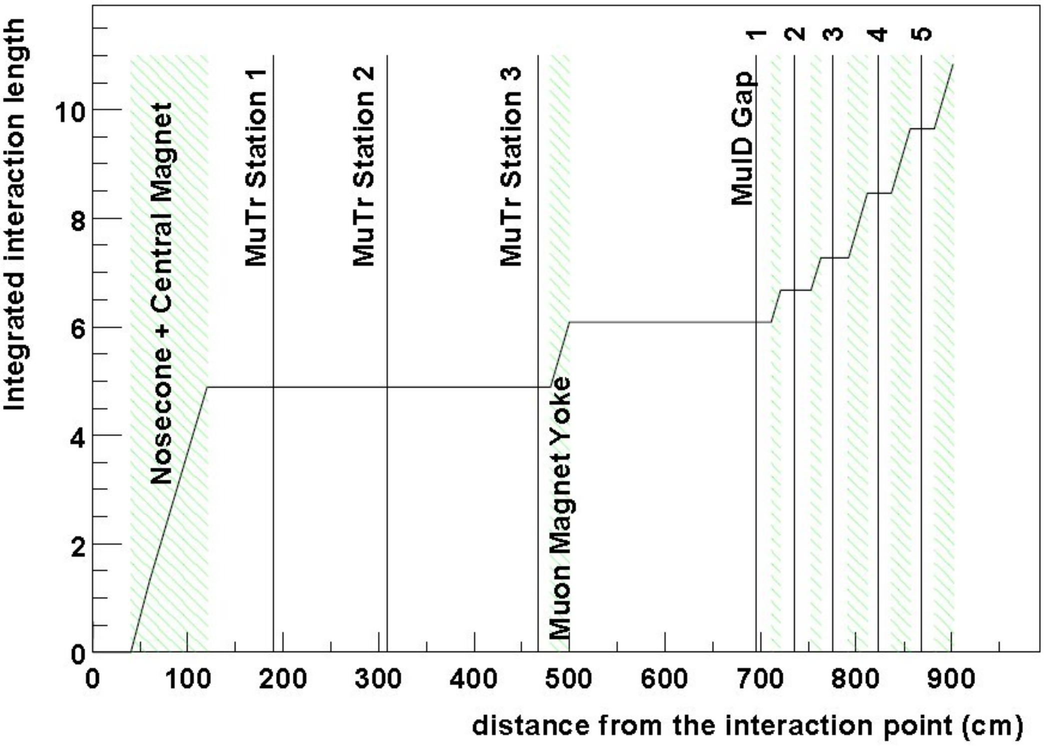

**Figure 3.19:** The integrated interaction length of south arm.

Typically, the irreducible $\mu/\pi$ ratio at collision point is $1\times 10^3$, and pion rejection factor is about $(2.0\pm1.4\times10^{-4})$ at muon momentum is 2.0 GeV/$c$ [58].

### 3.6.2 MuTR (Muon TRacker)

MuTR is placed inside MMN and MMS. As shown in Fig 3.20, MuTr is composed of the three stations and one station is divided into eight sectors called as octant 1 to 8. Each octant covers

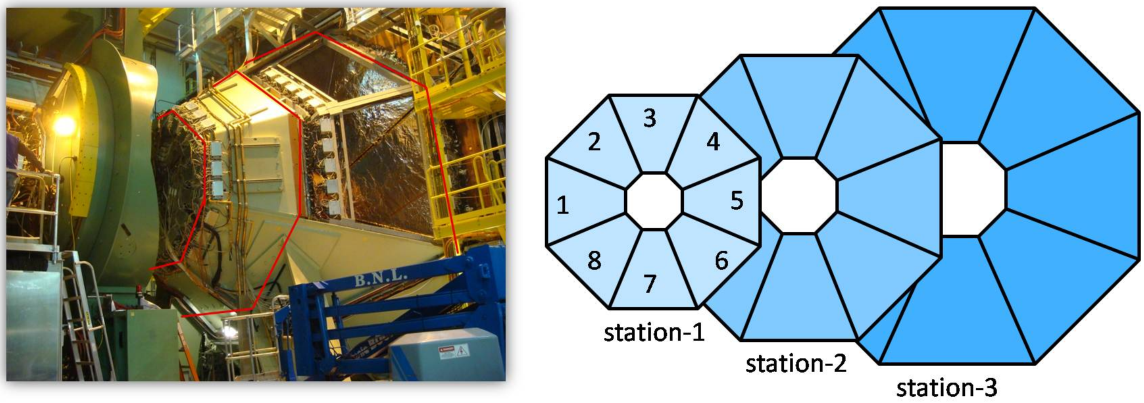

**Figure 3.20:** The schematic view of MuTR.

$\pi/4$. As shown in Fig 3.21, each octant divided into two half octant. Each octant in station 1

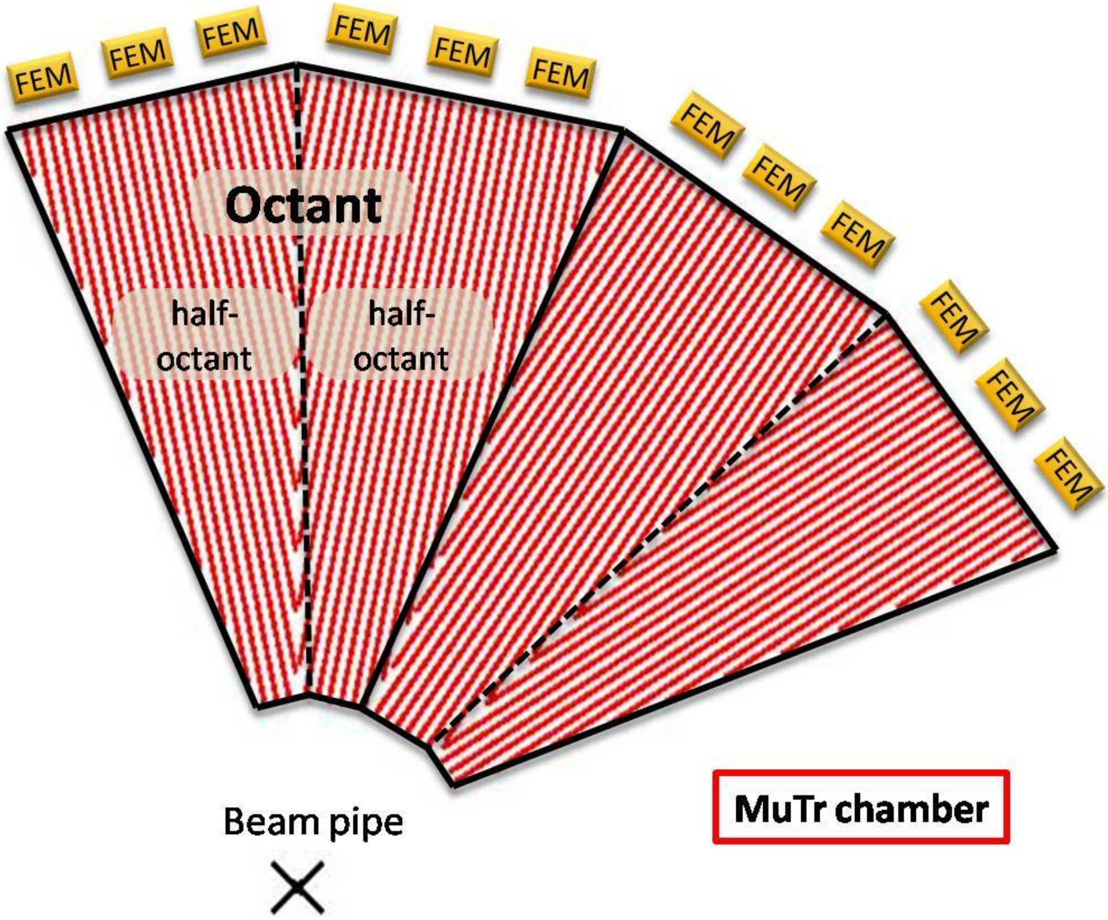

**Figure 3.21:** The schematic view of a super module of MuTR octant.

and 2 (3) consists of cathode strip readout tracking chambers with three (two) gaps. As shown in Fig 3.22, each gap is a sandwich of two cathode strip planes and an anode wire plane. Each gap has two types of cathode strip planes, stereo and non stereo planes.

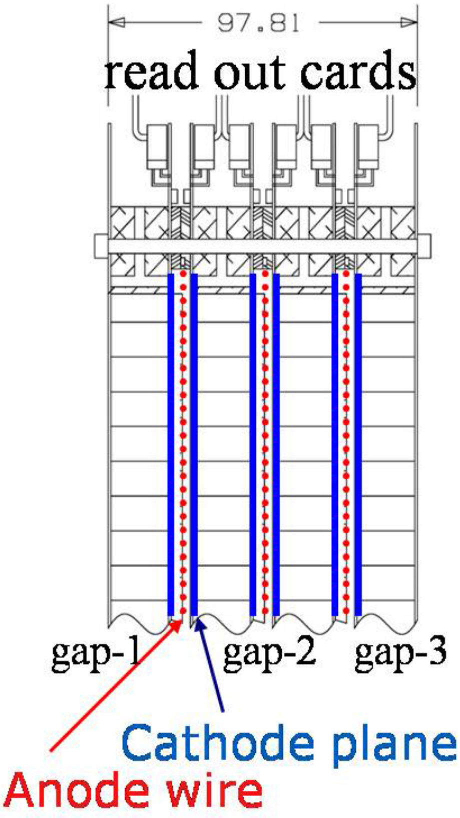

**Figure 3.22:** The schematic view of inside of of MuTR .

Wires of stereo planes are orthogonal to the outer circumference of MuTR. And wires of non stereo planes are little twisting. As summarized in Tab. 3.3, angles are different gap by gap. The used gas is a mixture of Ar (50%), $CO_2$ (30%), and $CF_4$ (20%). Typical operation

**Table 3.3:** The azimuthal offset angles between wires of stereo and non stereo planes.

| | |
|---|---|
| station 1 gap 1 | -11.25 |
| station 1 gap2 | 6.00 |
| station 1 gap3 | 11.25 |
| station 2 gap 1 | +7.50 |
| station 2 gap 2 | +3.75 |
| station 2 gap 3 | +11.25 |
| station 3 gap 1 | -11.25 |
| station 3 gap 2 | -11.25 |

voltage is 1900 V and typical gain is $2\times 10^4$. The position resolution in cosmic lay test is 130 $\mu$m. The relative mass resolution of the reconstructed muon pair is given by $\sigma(M)/M$ =9 % $/\sqrt{M}$.

### 3.6.3 MUon IDentifer (MUID)

MuID is a sandwich of five drift tubes and four steel absorbers. Each drift chamber is called gap1, 2, 3, 4, and 5. (Sometimes, gap0, 1, 2, 3, and 4 are used. In this thesis, 1, 2, 3, 4, and 5 are used.) The photo of MUID is shown in Fig. 3.23.

**Figure 3.23:** The schematic view of MUID.

Each gap consists of four large panels and two small panels as shown in Fig 3.24.

The configuration of wire chamber is shown in Fig. 3.25, each wire chambers consists of eight 100 $\mu$m gold coated Cu+Be anode wires at the center of long channels of a graphite coated plastic cathode.

The used gas is mixture of $CO_2$ (92%) and i-$C_4H_{10}$(8%). Typical operation voltages are 4300 − 4500 V, and typical gain is $2\times10^4$.

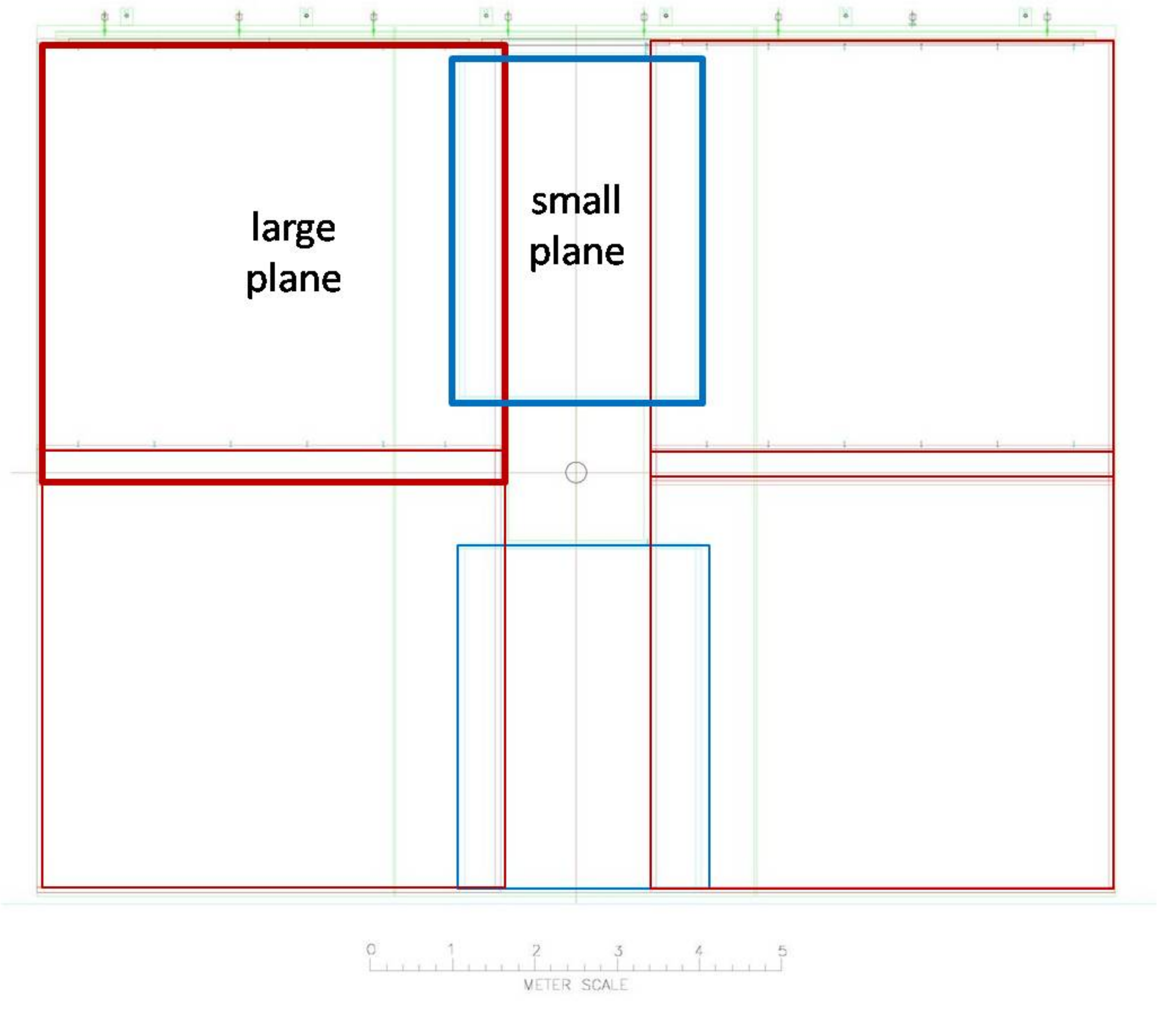

**Figure 3.24:** Upper: Cross section of the MUID panel. Lower:Cross section of the plastic tube.

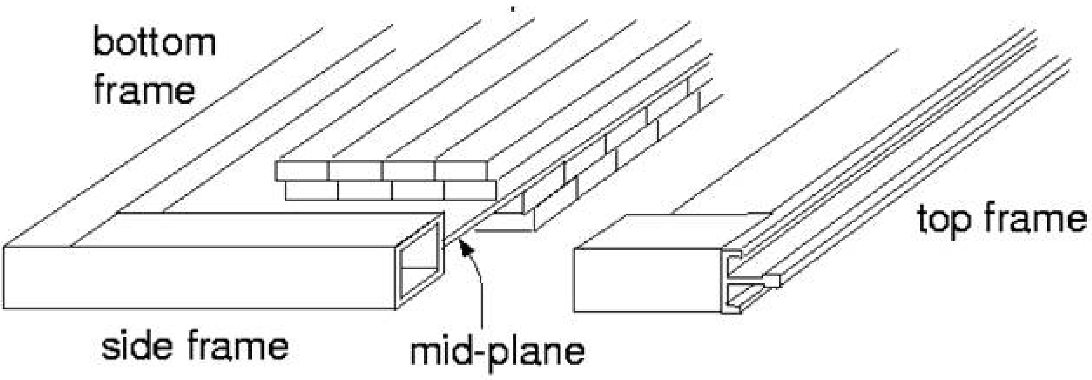

Cross section of the MuID panel

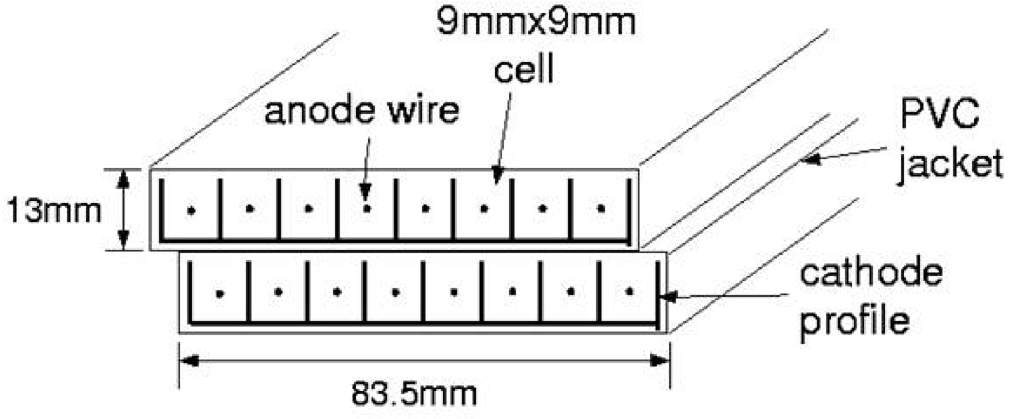

Cross section of the plastic tube(2-pack)

**Figure 3.25:** The schematic MUID wire chamber

## 3.7 Trigger and Data acquisition

### 3.7.1 Trigger

The PHENIX Level-1 trigger (LVL1) is used to select interesting events among the collisions [59]. LVL1 consists of Local Level-1 (LL1) and GlobalLevel-1 (GL1). LL1 is a low level decision provided by detectors such as BBC, ZDC, EMCal, RICH, and MuID. BBC LL1 trigger (BBCLL1) is an event trigger being used as PHENIX minimum bias trigger. Typical PHENIX analysis requires $|Z_{VTX}| < 30$ cm. However BBCLL1 itself requires $|Z_{VTX}| <50$ cm. LL1 provided by RICH & EMCal (ERTLL1) and EMCal is used to select events with electrons and high energy photons, respectively.

GL1 receives LL1 trigger signals and make a final decision for the data acquisition within 30 beamclock (BC), where one BC has 110 nsec.

### 3.7.2 Data AcQuisition (DAQ) System

The schematic diagram of PHENIX DAQ is shown in Fig. 3.26. The PHENIX DAQ system treats the data from all PHENIX detectors, makes triggers, and stores the triggered data [59].

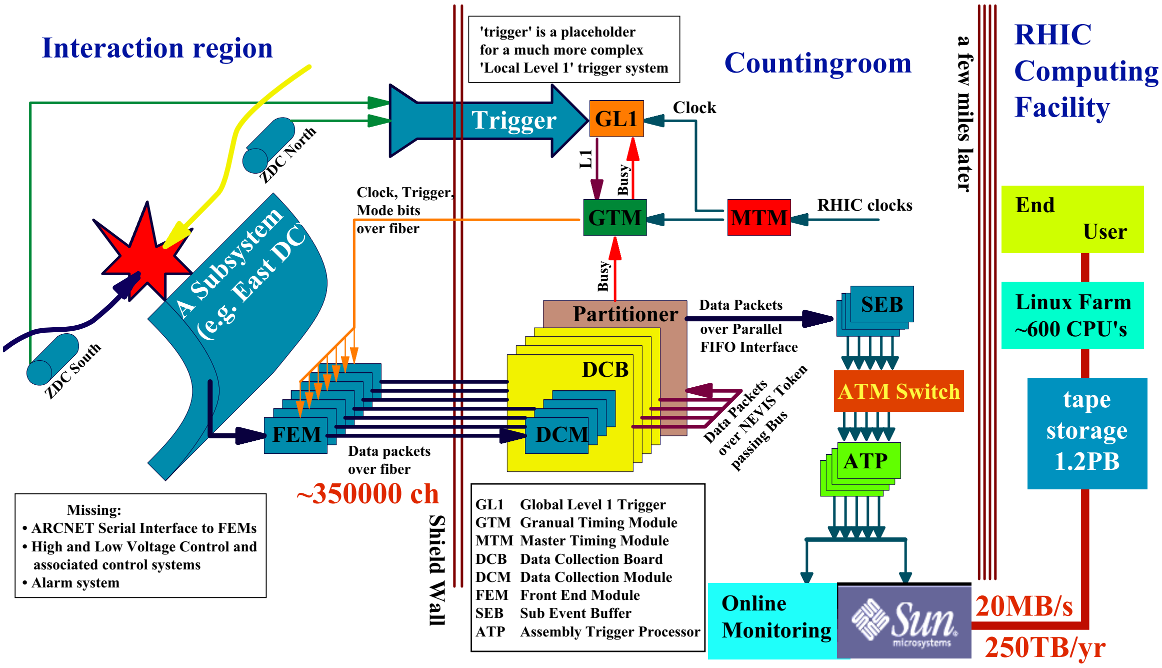

**Figure 3.26:** Schematic diagram of PHENIX data acquisition system.

9.4 MHz RHIC clock goes to MTM, then MTM sends it to GL1 and GTM. GTM sends control commands including initialization, reset, and event accept signal (Mode Bit), and an event accept signal to the Frond End Modules (FEM) of each detector. Timing adjustment of LVL1 trigger for each FEM can be done at GTM. GL1 make the first LVL1 decision, combining

LVL1 signals from the detectors. Making a global decision means the data should be taken or rejected.While the process, the FEM of each detector stored the signal data.

PHENIX FEM keeps analog signals in the analog memory and once the FEM receives LVL1 signal, corresponding analog data is converted to digital data, and finally digital data is sent to the Data Collection Module (DCM). The DCM does data buffering , zero suppression, error checking and data formatting. The DCM sends the data to the Event Builder (EvB). The EvB consists of 39 Sub Event Buffers (SEBs). The SEBs send the data to 52 Assembly Trigger Processors (ATPs) through Asynchronous Transfer Mode (ATM). ATPs perform event assembly. Finally, the data are stored to the disk with maximum logging rate of 400 Mbytes/s. The typical zero suppressed event size is 160 kbytes for Au+Au collisions. Then, expected rate is about 2.5 kHZ In the 2007 and 2010 PHENIX run, measured typical event size is a little lower (about 100 kbytes) and the typical minimum byas rate is a little higher (about 3 kHz)

# Chapter 4

# Run conditions in the 2007 and 2010 PHENIX runs in Au+Au collisions at $\sqrt{s_{NN}}$ =200 GeV

The analysis is based on the data which was taken in the 2007 and 2010 PHENIX runs. The run and trigger conditions are described in the chapter.

## 4.1 UPC trigger

The events which are looking for are ones with a lepton pair and nothing else in the main detectors.

Therefore, on contrary to the minimum bias trigger of the PHENIX, little hits in BBC is required. Special triggers for the UPC events have following logic.

1. Central UPC trigger:" ERT2x2 & $\overline{(BBCN\&BBCS)}$ &ZDC" Detail of each subtriggers is described in the next section. Essentially, it requires at least one energy deposit above the threshold (in 2007, 1 GeV) in the Emcal in the central arm with at least one of the two BBC has no hit. In addition at least one of two ZDC has energy above 30 GeV.

2. Forward UPC trigger:" MUID2D $\overline{(BBCN\&BBCS)}$ && ZDCLL1" This trigger requires two muon candidate tracks in one of the Muon arms with at least one of the two BBC has no hit. In addition both ZDC are required to have energy deposit above 30 GeV.

As a reference events, triggered with following logic are used for the comparison studies.

1. The minimum bias trigger in the Au+Au runs BBCLL1(tube>1). At least "two" tubes in north and south BBC getting a minimum ionization particle, and reconstructed absolute value of $z$ vertex from BBC timing information is within 30 cm.

2. The minimum bias trigger in the p+p runs BBCLL1(tube>0). At least "one" tubes in north and south BBC getting a minimum ionization particle, and reconstructed absolute value of z vertex from BBC timing information is within 30 cm.

| Trigger | rate |
|---|---|
| UPC central | 20 Hz |
| BBCLL1 | 3.6 kHz |
| BBCLL1(novtx) | 7.6 kHz |
| ERT2x2 | 8.8 kHz |
| ZDCLL1wide | 12 kHz |
| ZDCLL1narrow | 6 kHz |

**Table 4.1:** Triggers and typical rate in 2007 PHENIX run

| Trigger | rate |
|---|---|
| UPC North | 58 Hz |
| UPC South | 50 Hz |
| BBCLL1 | 3.7 kHz |
| BBCLL1(novtx) | 7.6 kHz |
| MuID_N1D \| S1D | 90 kHz |
| ZDCLL1wide | 14 kHz |
| ZDCLL1narrow | 5.7 kHz |

**Table 4.2:** Triggers and typical rate in 2010 PHENIX run

### 4.1.1 Description of the other triggers

- BBCN (BBCS):At least "two" tubes in north (south) BBC has energy deposits more than the threshold which is set at the two sigma below the average deposit of the minimum ionization particle.
- BBCLL1novtx:BBCN & BBCS
- ERT2x2:Any pattern of 2 × 2 Emcal tiles has at least 1 GeV energy deposit.
- MUIDN(S)XD:At least X muon candidate tracks reaches North (South) MUID gap3.
- ZDCN (ZDCS):North(south) ZDC is getting at least an neutron
- ZDCLL1wide:ZDCN & ZDCS
- ZDCLL1narrow : ZDCLL1wide with vertex cut ($|z| < 30$ cm)

### 4.1.2 Trigger rates during run

The typical rate of the triggers in 2007 and 2010 are shown in Tab. 4.1 and Tab. 4.2.

The rate of central, north and south UPC triggers are 20, 58, 50 Hz, respectively. Their rates are lower enough than total bandwidth of PHENIX DAQ (few thousands Hz).

It is preferable to has a trigger without ZDC requirements. However because of the high rates of ERTLL1 and MUID triggers, there rates were 2 kHz for the central and 50 kHz for the forward triggers. So that they were not be implemented.

The both side neutron tagging in forward triggers are required to measure z vertex. The detail will be described in Chap 6.

## 4.2 The 2007 PHENIX run

In 2007, RHIC was operated only Au+Au collisions with $\sqrt{s_{NN}}$ =200 GeV. In this run period, the HBD was installed inside of the central arms. The run was divided into three groups,

1. G1:run with west and east HBD and with $+-$magnetic field configuration
2. G2:run with east HBD and with $+-$magnetic field configuration. The west HBD was removed.
3. G3:run with east HBD and with $-+$magnetic field configuration

Because G1 period is short and unstable, runs in the G1 group were not used in this thesis. In this thesis, the data from HBD wasn't used but additional material should change the efficiency of electron identification. The integrated luminosity of G2 and 3 is 527 $\mu b^{-1}$. The integrated luminosity as a function of date is shown in Fig. 4.1. In this year, PHENIX already had the muon arm UPC trigger, but unstable. Therefore, only central data were analyzed in this thesis.

## 4.3 The 2010 PHENIX run

In 2010, RHIC performed energy scan with Au+Au collisions. This year PHENIX took data with $\sqrt{s_{NN}}$ = 200, 62.4, 39 and 7 GeV. Unlike 2007 case, in PHENIX, detector conditions were stable. Only $\sqrt{s_{NN}}$ = 200 GeV run is used in this analysis. The other runs are short and little integrated luminosity.

The integrated luminosity as a function of date is shown in Fig. 4.2. The analyzed integrated luminosity of the analysis is about 640 $\mu b^{-1}$ In this year, the central and the muon arms UPC trigger is available. In this analysis, only data of the forward region are analyzed.

## 4.4 2006 and 2009 runs

In 2006 and 2009, RHIC ran with p+p collisions at $\sqrt{s}$ =200 GeV. These pp data can be used as a reference data in this thesis.

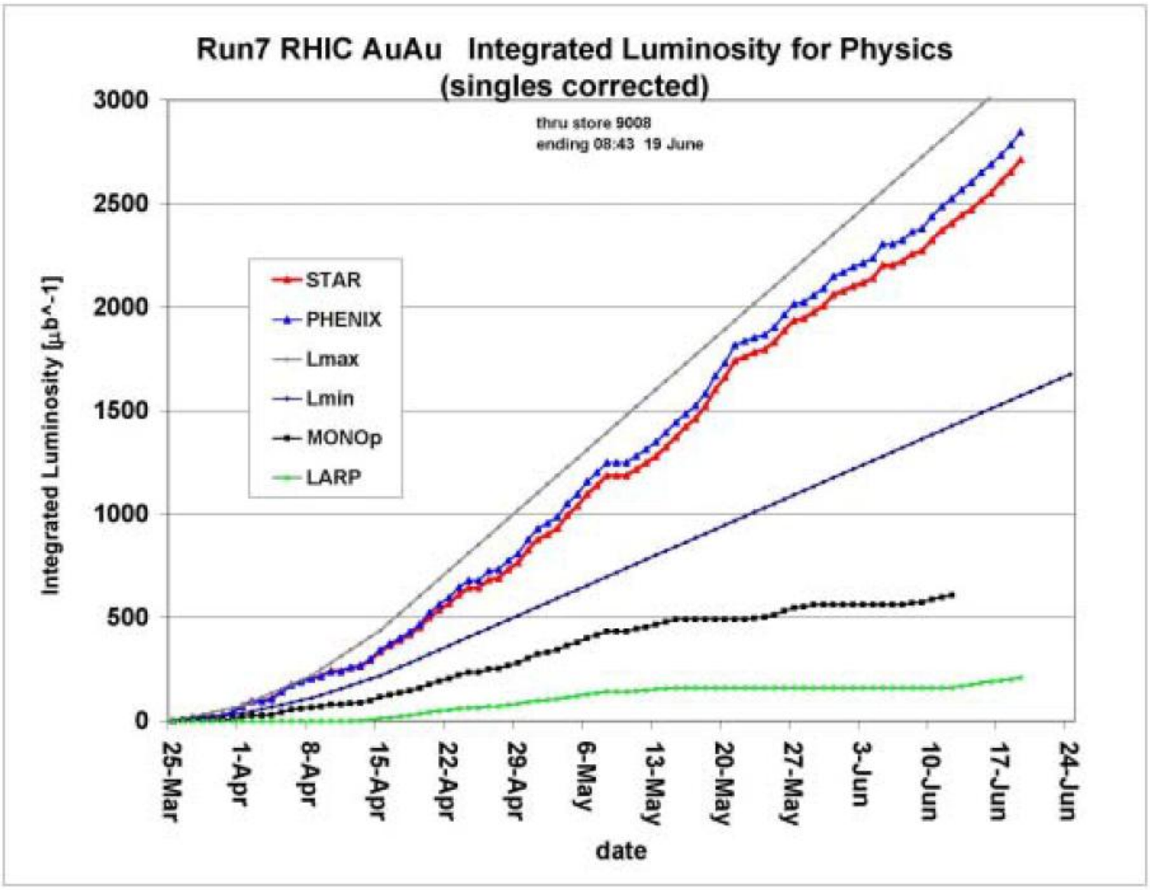

**Figure 4.1:** The 2007 RHIC DC luminosity as a function of date [60]

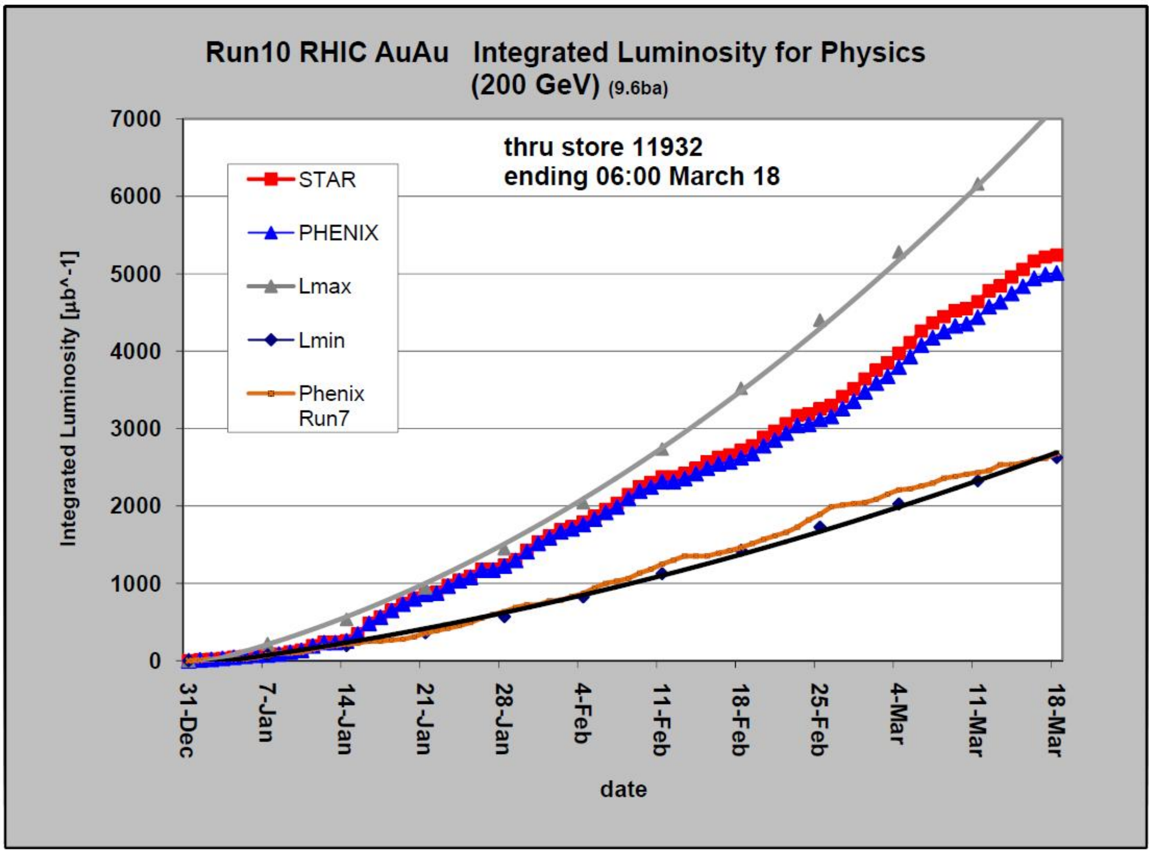

**Figure 4.2:** The 2010 RHIC DC luminosity as a function of date [60]

# Chapter 5

# Analysis of $J/\psi$ -production at mid rapidity

The cross section is extracted with the following formation.

$$\frac{B_{ee}d^2\sigma_{J/\psi}}{2\pi p_T dp_T dy} = \frac{1}{2\pi p_T \Delta p_T \Delta y}\frac{N_{J/\psi}}{(Acc \cdot \epsilon_{reco} \cdot \epsilon_{cuts}) \cdot \epsilon_{trigger} \cdot \mathcal{L}_{int}}, \tag{5.1}$$

$$\tag{5.2}$$

where $B_{ee}$ is the $J/\psi \rightarrow e^+e^-$ branching ratio, 0.0593. $\Delta y$ is 0.7 corresponding to the acceptance of the PHENIX central arm rapidity. $N_{J/\psi}$ is the number of measured $J/\psi$ s. $\mathcal{L}_{int}$ is the integrated luminosity. $\epsilon_{trigger}$ is the efficiency of UPC trigger. $Acc$ is the geometrical acceptance of $J/\psi$ of the PHENIX detector. $\epsilon_{reco}$ is the efficiency of the reconstruction process. $\epsilon_{cuts}$ is the efficiency of the analysis cuts. $(Acc \cdot \epsilon_{reco} \cdot \epsilon_{cuts})$ is the overall acceptance of $J/\psi \rightarrow e^+e^-$pair and is treated as one parameter. In the following sections, detail of the analysis is described.

## 5.1 The track reconstruction

### 5.1.1 The definition of PHENIX variables

Detail of the track reconstruction method of the PHENIX central arm is described in Ref [61]. In this section, the definition of the variables which will be used in the thesis is briefly presented.

1. $P$:The total momentum of the track at the interaction point
2. $\phi_0$:The azimuthal angle of the track at the interaction point
3. $\theta_0$:The polar angle of the track at the interaction point
4. $p_T$ :The transverse momentum of the track $= P \sin\theta_0$
5. $p_z$:The longitudinal momentum of the track $= P \cos\theta_0$
6. $n_0$:The number of fired RICH phototubes associated to the track in the nominal ring area($3.8 \leq r \leq 8.0cm$) at the PMT plane. The area corresponds to $\beta$ =1 particles.
7. *ecore*:The EMCal shower core energy (GeV) associated to the track
8. *dep*.The normalized energy and momentum matching parameter (assumed as an electron); $(\frac{\frac{ecore}{P} - <\frac{ecore}{P}>}{\sigma(\frac{ecore}{P})})$
9. $emcsdphi_e$ and $emcsdz_e$:The position difference between projected track and EMCal cluster in the $\phi$ and $z$ direction. They are normalized by $\sigma$
10. $z_{VTX}$:$z$ position of the interaction point (non track by track parameter). Sometimes $z_{BBC}$, $z_{ZDC}$, and $z_{PC}$ are used to make clear source of the information.
11. $E_{ZDCN}$ and $E_{ZDCS}$: The energy deposit in ZDC North /South in unit of GeV. In general, $\frac{E_{ZDCN}}{100(GeV)}$ is a measure of the number of neutrons.
12. $N_{BBCN}$ and $N_{BBCS}$:The number of fired phototubes in North and South BBC. Phototubes which detected at least a minimum ionizing particle with 2 $\sigma$ criteria are getting fired.
13. $N_{track}$:The number of tracks in the Central arm with the highest quality in the central arm with ghost cut. The detail will be discussed later.
14. *centrality*:The experimentally determined centrality classes that have a monotonic dependence on the impact parameter. Centrality is determined by the $E_{ZDC}$ and charge in BBC. The centrality classification is shown in Fig 5.2. Most central collision events are defined as $centrality = 0$, and most peripheral events are defined as $centrality$ =100. In simulation, 7% of total Au+Au collisions does not hit BBC [49], therefore event with $93 < centrality < 100$ can't be triggered by MB trigger.

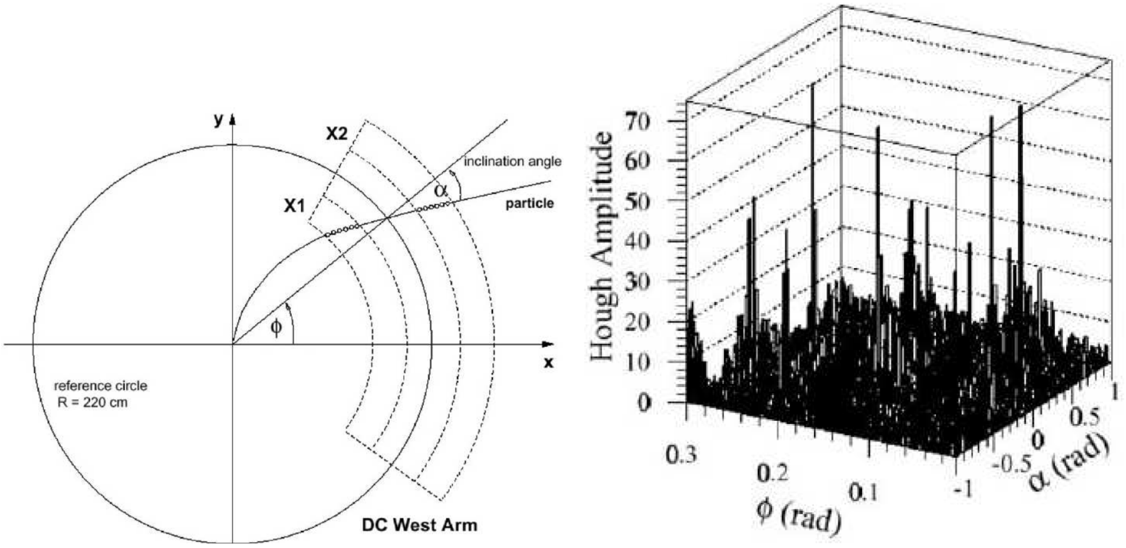

**Figure 5.1:** Left:The definition $\alpha$ and $\phi$. Right: An example scatter distribution of $\alpha$ and $\phi$ of all possible pairs.

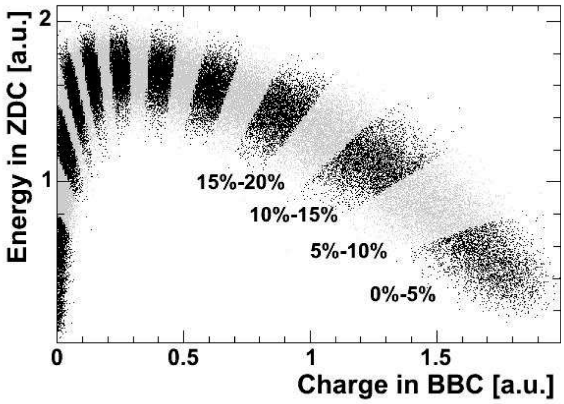

**Figure 5.2:** Centrality classes in the $E_{ZDC}$ vs. charge in BBC scatter plot.

### 5.1.2 The tracking algorithm

In most central Au+Au collisions at $\sqrt{s_{NN}} = 200$ GeV, the PHENIX detector detects hundreds of charged tracks. The PHENIX has a robust algorithm to reconstruct tracks in such high multiplicity environment. However, this analysis focused on the events with only a few tracks. Even though there are two primary tracks, sometimes it happens to reconstruct more than three tracks due to multiple scattering, delta rays and so on. In this analysis, the cut of $N_{track}$ =2 is required in the event selection and loss of the events by above reason is taken into account in the efficiency calculation. The algorithm was briefly described below.

**Tracking**

1. The hits in X1 and X2 layers in DC are searched.
2. Straight lines are drawn between all possible pairs. If N layer of X1 and X2 planes find a hit, $\frac{N(N-1)}{2}$ straight lines are generated. In the $r$ direction, there are 12 layers in DC. Even if there is just one true track, 66 pairs are generated, in case hit efficiency is 100 %.
3. $\alpha$ and $\phi$ defined in the left panel of Fig 5.1 are extracted from each line. The distribution of $\alpha$ and $\phi$ is plotted. An example is shown in the right panel of Fig 5.1.
4. The local maximum of $\alpha$ and $\phi$ is searched for. In $\alpha - \phi$ plane, if there are an $(\alpha, \phi)$ set of the true track, it will be associated with many fake $(\alpha, \phi)$ sets.
5. The tracks are reconstructed and extrapolated to PC1. If there are unambiguous PC1 hits within 2 cm, then the PC1 hits are associated.
6. The reconstructed tracks in the $r - z$ plane. If there are unambiguous UV hit within 5 cm, then the UV hit is accepted
7. If the reconstructed track was associated with hit information of outer detectors (PC2, PC3, RICH, and EMcal ), this information was used to determine track variables.

**Track quality** Quality of reconstructed track is defined using DC and PC hit information as follows. Tracks with the best quality have 63 in the flag, as all detectors have hits. Only the tracks with the best quality are used and counted in this thesis.

**Table 5.1:** The definition of reconstructed track.

| bit | decimal | description |
|---|---|---|
| 0 | 1 | X1 hit is used |
| 1 | 2 | X2 hit is used |
| 2 | 4 | UV hit is found |
| 3 | 8 | UVhit is unique |
| 4 | 16 | PC1 hit is found |
| 5 | 32 | PC1 hit is unique |

**Ghost cut** Sometimes, the tracking algorithm makes ghost tracks. In UPC samples, since lower multiplicity is expected, the looser criteria are used.

The distribution of the distance between the best quality tracks at PC1 in the typical MB run is shown in Fig. 5.3 and same one for UPC triggered data is shown in Fig 5.4. The peak at near 0 is enhanced in UPC triggered samples. In the counting of $N_{track}$, too close tracks ($> 4$ cm) are counted as one track.

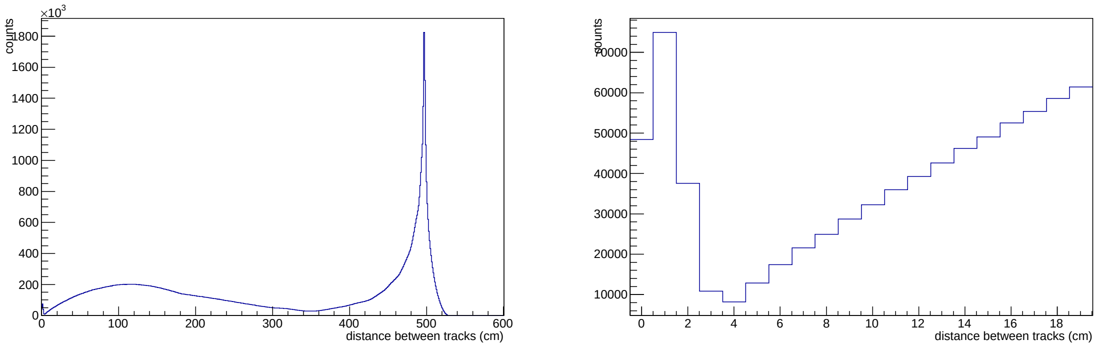

**Figure 5.3:** Left:The distribution of the distance between the best quality tracks at PC1 in typical MB run in 0∼800 cm. Right:The distribution of the distance between the best quality tracks at PC1 in typical MB run in 0∼18 cm.

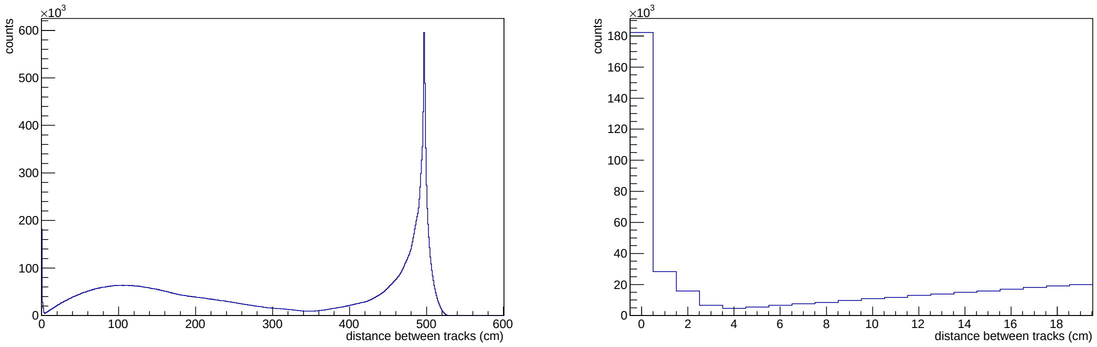

**Figure 5.4:** Left:The distribution of the distance between the best quality tracks at PC1 in typical UPC run in 0∼800 cm. Right:The distribution of the distance between the best quality tracks at PC1 in typical UPC run in 0∼18 cm.

### The momentum reconstruction

The detail of the PHENIX momentum reconstruction method is described in Ref [61, 62]. A brief description is as follows.

1. Association grids between the track parameters $(P, \theta, z_{vtx}, \phi)$ and geometrical parameters $(\alpha, \beta, z_{pad}, \Phi)$ defined for each pattern recognition solution are obtained by full simulation. The momentum interpolation grid is shown in Fig 5.5

2. By using the grids. $\alpha, \beta, z_{pad}, \Phi$ are converted to its initial track parameters $(P, \theta, z_{vtx}, \phi)$ .

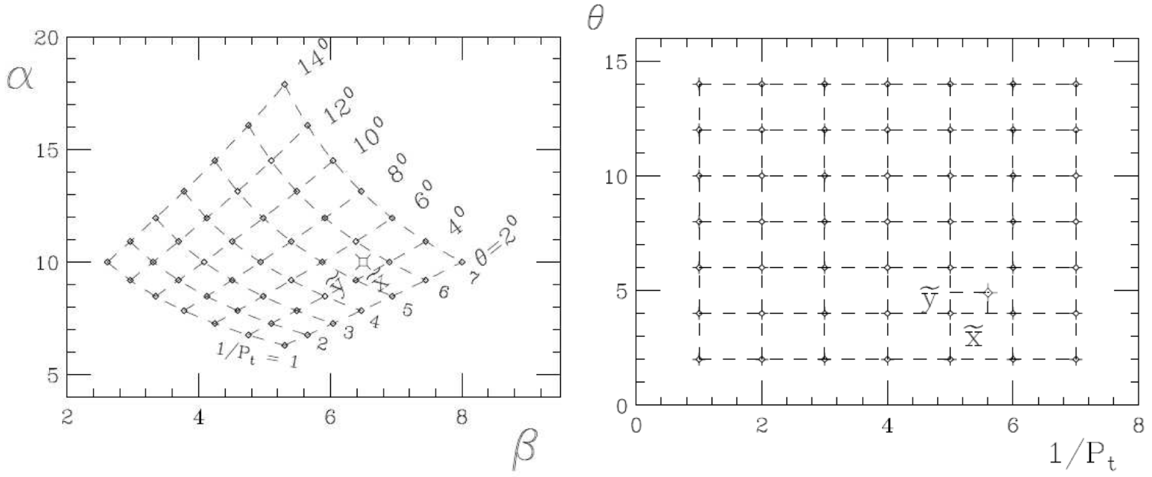

**Figure 5.5:** Momentum interpolation grid.

### 5.1.3 The electron (positron) selection

The following standard track cuts were applied to select electron or positron tracks:

1. $n_0 \geq$2 :At least two photo tubes in the RICH are fired.
2. $dep > -3$:The energy and momentum are consistent within 3 $\sigma$ criteria.
3. $\sqrt{(emcsdphi_e \times emcsdphi_e + emcsdz_e \times emcsdz_e)} \leq$5:The distance between projected track and the nearest Emcal is within 5 cm.

The simulated distributions of those of electrons from $J/\psi$ (0< $p_T$ ($J/\psi$ ) < 5 GeV/c) are shown in Fig. 5.6 and 5.7. The samples are the ones used in Sec. 5.8.1.

## 5.2 Vertex reconstruction

$z_{PC}$ is determined by a simple average of straight extrapolation at PC1 and PC3 from charged tracks to $(0, 0, z)$.

### 5.2.1 The difference between $z_{BBC}$, $z_{ZDC}$ and $z_{PC}$

The resolutions of the $zvtx$ from BBC ($\sigma_{z_{BBC}}$), ZDC ($\sigma_{z_{ZDC}}$), and PC ($\sigma_{z_{PC}}$) are measured with Au+Au data taken in 2002. The method is as follows.

1. As the true $zvtx$ can't be determined, the resolution is decided from three distributions, $z_{BBC} - z_{ZDC}$, $z_{ZDC} - z_{PC}$, and $z_{PC} - z_{BBC}$.

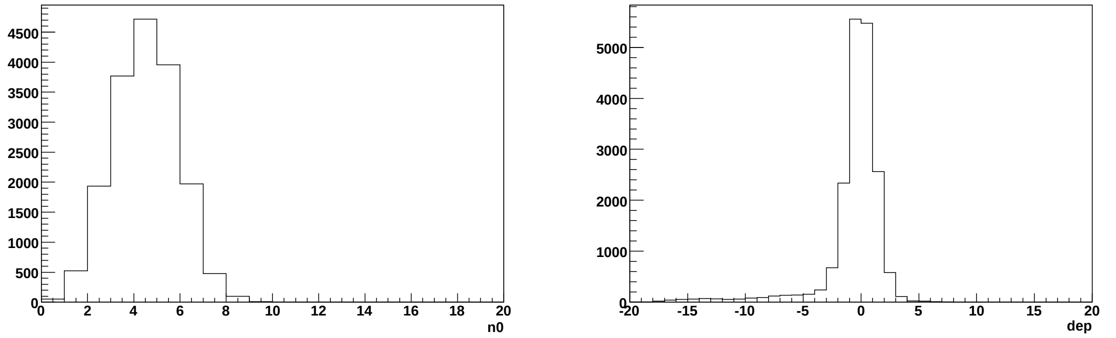

**Figure 5.6:** Left: The simulated $n0$ distribution of electrons. Right: The simulated $dep$ distributions of electrons.

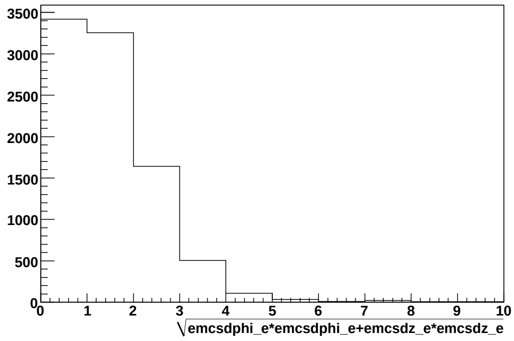

**Figure 5.7:** The simulated $\sqrt(emcsdphi_e \times emcsdphi_e + emcsdz_e \times emcsdz_e)$ distribution of electrons.

2. Fit the three distributions with Gaussian function and get $\sigma_{z_{BBC}-z_{ZDC}}$, $\sigma_{z_{ZDC}-z_{PC}}$, and $\sigma_{z_{PC}-z_{BBC}}$.
3. Solve the system by following equations.
   (a) $\sigma^2_{z_{BBC}-z_{ZDC}} = \sigma^2_{z_{BBC}} + \sigma^2_{z_{ZDC}}$
   (b) $\sigma^2_{z_{ZDC}-z_{PC}} = \sigma^2_{z_{ZDC}} + \sigma^2_{z_{PC}}$
   (c) $\sigma^2_{z_{PC}-z_{BBC}} = \sigma^2_{z_{PC}} + \sigma^2_{z_{BBC}}$

These values measured $\sigma_{z_{BBC}} = 0.6$ cm, $\sigma_{z_{ZDC}} = 2.5$ cm, and $\sigma_{z_{PC}} = 0.2$ cm.

### Multiplicity dependence of the $\sigma_{Z_{PC}}$

In UPC, since events have the lower multiplicity than Au+Au collisions, $\sigma_{z_{ZDC}}$ and $\sigma_{z_{PC}}$ may be worse. However, for $\sigma_{z_{ZDC}}$, even one neutron case, $\sigma_{z_{ZDC}}$ =3 cm [50], [51], [52], the difference is not so significant.

The $\sigma_{z_{PC}}$ require more detailed discussion. In the standard PHENIX analysis, $z_{PC}$ is defined as an average of all $z$ vertexes extrapolated all reconstructed tracks. UPC $J/\psi$ events have just two electron tracks. To get realistic $\sigma_{z_{PC}}$, for one good track, $\sigma_{z_{PC}1track}$ is measured, where the good track means that the track is the highest quality electron track and its $p_T$ is higher than 1.4GeV$/c$ . The distribution of $z_{BBC} - z_{PC}1track$ in MB samples is shown in Fig 5.8. Assume $\sigma_{z_{BBC}}$ is constant, then $\sigma_{z_{PC}1tracks}$=0.6 cm. In conclusion, vertex resolution for UPC events is better than $\sigma_{z_{BBC}} = 0.6$ cm.

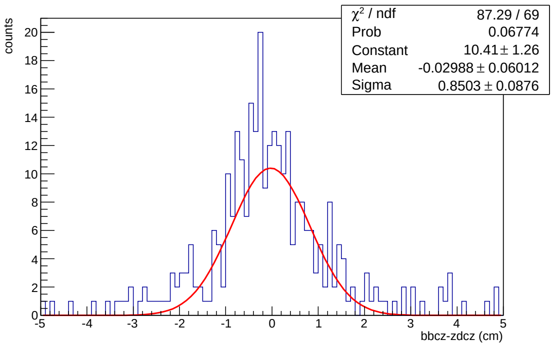

**Figure 5.8:** The distribution of $z_{BBC} - z_{PC}1track$ .

## 5.3 The fiducial cuts

The PHENIX detector is a large complex of subsystems (DC, PC, RICH, and EMCal). A typical PHENIX run period is about a half year. Some part of detectors becomes broken or noisy, and can't be fixed soon. Therefore, those unstable parts should be removed from the analysis.

In the 2007 PHENIX run, the same fiducial cut is used in the $J/\psi$ analysis in Au+Au collisions [63].

Since ERT2x2 trigger is used in the analysis, the tiles which have very low noise rate but return high values throw out the trigger efficiency calculation. The noisy channels listed in Tab. 5.4 in Sec. 5.7.4 are also removed. The detail of fiducial cut is described very briefly below. In this section, MB (not UPC) data are used.

### 5.3.1 Fiducial cut on DC and PC

The main cause of the dead channels of the DC and PC was broken or tripping wires. The distributions of $\phi$ from DC and $zed$ for positrons and electrons in MB data is shown in Fig. 5.9 . The fiducial areas are decided based on these plots.

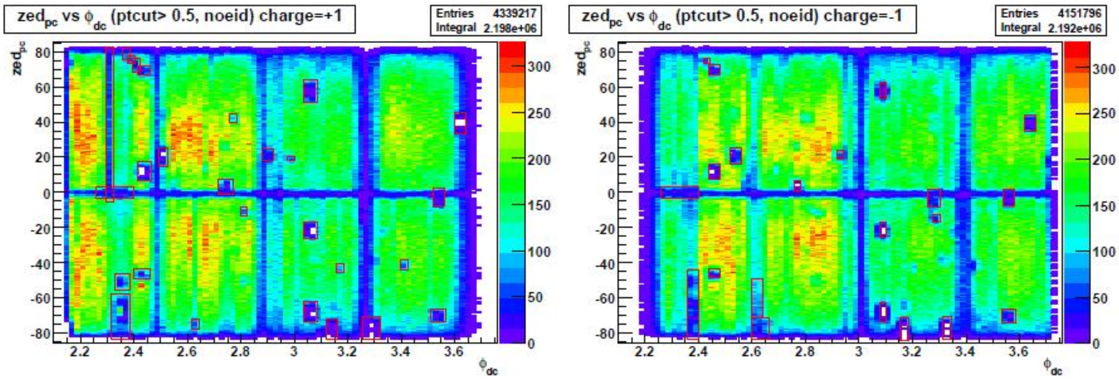

**Figure 5.9:** Left:The distribution of electrons (left) $\phi_{dc}$ (zed) and $zed_{pc}$ (cm) of reference run. The distribution of positrons $\phi_{dc}$ (zed) and $zed_{pc}$ (cm) of reference run [63]

### 5.3.2 Fiducial cut on EMCAL

Following method is used to find broken, hot and noisy EMCAL tiles.

1. A ratio of the number of electrons to that of the charged particles ($R_{el/tr}$) is plotted in $ysect - zsect$ plane, where $ysect$ and $zsect$ means EMCal tile id.

2. If $R_{el/tr} < 0.56$, the tile is excluded. An example of a typical tile of the sector 2 is shown in Fig. 5.10.

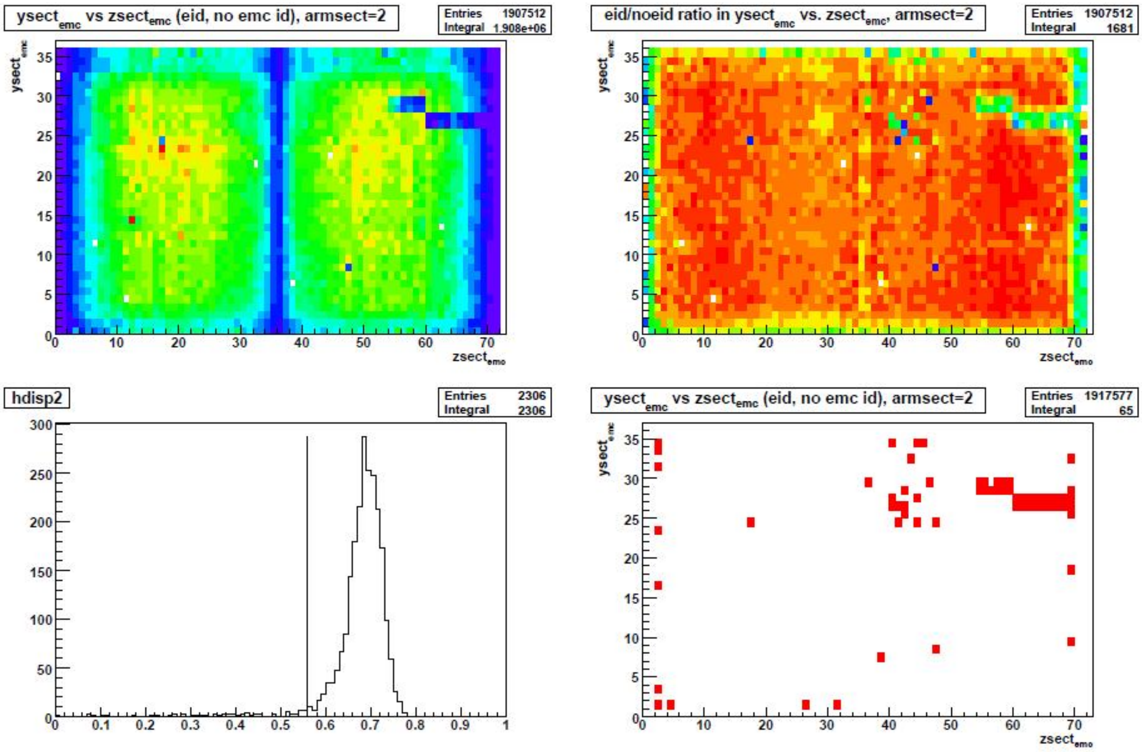

**Figure 5.10:** Upper left: The scatter distribution of the electron multiplicity of *ysect* and *zsect* at sector 2, where *ysect* and *zsect* means EMCal tile id. Upper right:The scatter distribution of the ratio of total per electron ($R_{el/tr}$) of *ysect* and *zsect* at sector 2. Lower left: The distribution of the $R_{el/tr}$ of overall towers at sector 2. Lower right:The scatter distribution of the excluded sectors of *ysect* and *zsect* at sector 2. [63]

### 5.3.3 Fiducial cut at RICH

The distribution of RICH ring center positions as calculated from circular fits to the fired PMTs of electrons is shown in Fig. 5.11. Fiducial area was decided by eye based on these plots.

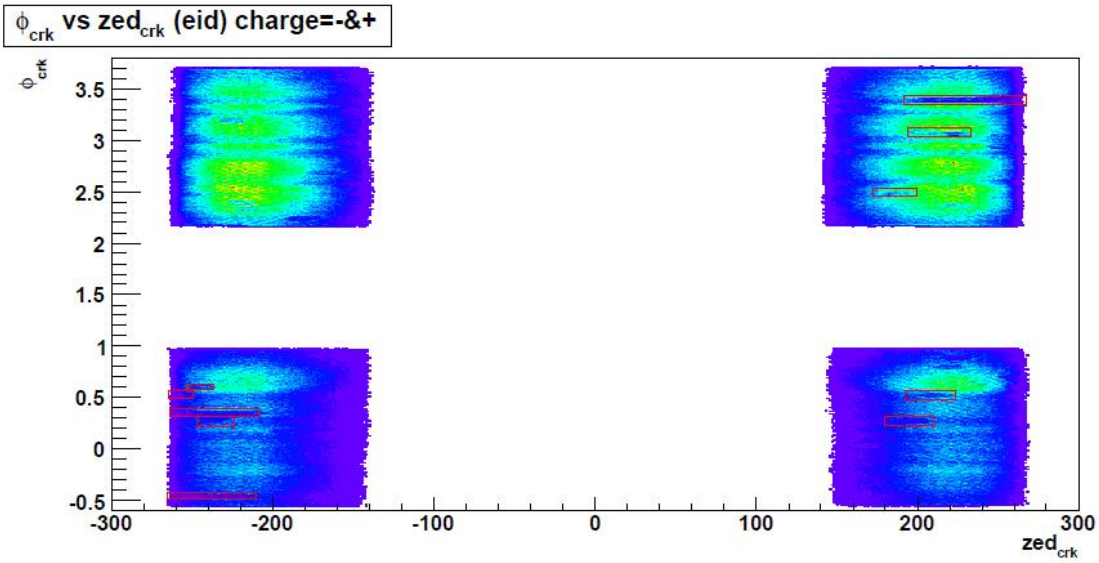

**Figure 5.11:** The scatter distribution of $\phi_{rich}$(zed) and $zed_{rich}$(cm) of reference run[63]

### 5.3.4 Fiducial cut of near $\eta$ =0

It is known that the PHENIX simulation system underestimates the dead zone which is covered with the center bracing struts. Then, correlation between $z_{BBC}$ and $\frac{1}{tan(\theta)}$ of charged particles is studied to remove the corresponding dead space. The scatter distribution is shown in Fig. 5.12. In this analysis, because $z_{BBC}$ can't be calculated, then $z_{PC}$ are used.

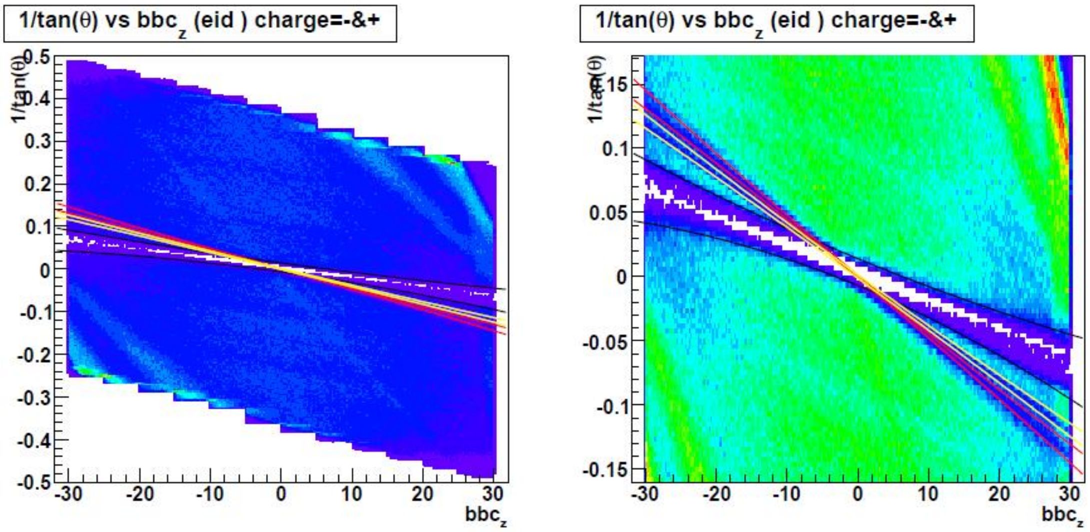

**Figure 5.12:** The scatter distribution of $z_{BBC}$ and $\frac{1}{tan(\theta)}$ of reference run[63]

| Cut | Number of unlike sign pair | like-sign pair |
|---|---|---|
| no-cut | $3.41184\times10^6$ | $3.3526\times10^6$ |
| $E_{ZDC}$ cut | $3.41051\times10^6$ | $3.35131\times10^6$ |
| $E_ZDC$ & $z_{PC}$ cut | $2.87019\times10^6$ | $2.8218\times10^6$ |
| $E_ZDC$ & $z_{PC}$ & $N_{BBC}$ cut | $2.21527\times10^6$ | $2.18717\times10^6$ |
| $E_ZDC$ & $z_{PC}$ & $N_{BBC}$ & $N_{track}$ cut | 245 | 7 |

**Table 5.2:** Cut and events

## 5.4 The event selection

Following selections are applied step-by-step in order to select UPC $J/\psi$ events.

- Good run selection:The criteria is described in the next section.
- Trigger selection:Events triggered with Central-UPC trigger are selected.
- At least two electron or positron tracks are found in the event. The selection is described in Sec. 5.1.3 .
- Offline reconfirmation of the triggered conditions.
  - $E_{ZDCN} > 30$ GeV | $E_{ZDCS} > 30$ GeV.
  - $(N_{BBCN} = 0 | N_{BBCS} = 0)$.
- vertex cut:$|z_{PC}| <30$ cm.
- $N_{track} = 2$

The number of electron (positron) pairs after each selection is shown in Table 5.2. As seen in the table, the final $N_{track} = 2$ cut reduce the events significantly.

### 5.4.1 Good run selection

The good runs are selected with the following requirements which are commonly used in other measurements.

1. The run lasted at least 15 minutes of data acquisition.
2. Online calibration is done for all detectors. (PHENIX detectors sometimes (day by day, week by week, etc.) need recalibration.)
3. The magnetic configuration is CM$+-$ or $-+$.

### 5.4.2 Characteristics of the events taken by the UPC trigger

In the UPC trigger, VETO on BBC is required. If there are any type of background contamination, low multiplicity in any detector is expected. In reality, sometimes, UPC triggered events have high multiplicity.

The distributions of $N_{BBCN}$ and $N_{BBCS}$ for UPC sampled events and MB sampled events are shown in Fig. 5.13. By the definition of UPC trigger, the figure on the left panel should have the entries at $N_{BBCN}$ =0 (or 1) or $N_{BBCS}$ =0 (or 1). However, there are entries, which should not be expected by the trigger requirements. (Actually, the event which have $N_{BBC}$ =2, 3... can be explained in the difference of $N_{BBC}$ in online and offline. ) Additionally, in Figure 5.14, $N_{track}$ distributions, in UPC (red), in MB with ERT2x2 (blue), and in UPC with ($N_{BBCN} = 0 \& N_{BBCS} = 0$) (magenta) are compared. To use a same vertex range, $|z_{ZDC}|$ <30 cm is required for all distributions. The MB distribution is normalized to have the same entries from $N_{track}$ of 40 to 100 as those in UPC events.

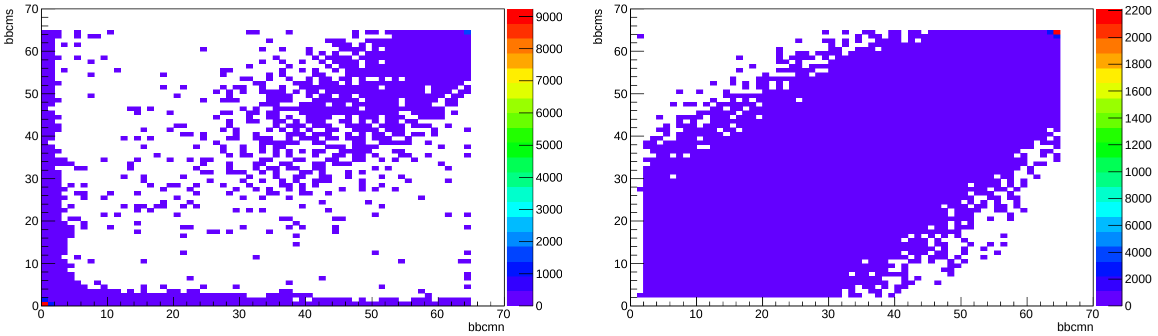

**Figure 5.13:** Left:The distributions of $N_{BBCN}$ and $N_{BBCS}$ of the UPC sampled events. Right:The distributions of $N_{BBCN}$ and $N_{BBCS}$ of the MB sampled events.

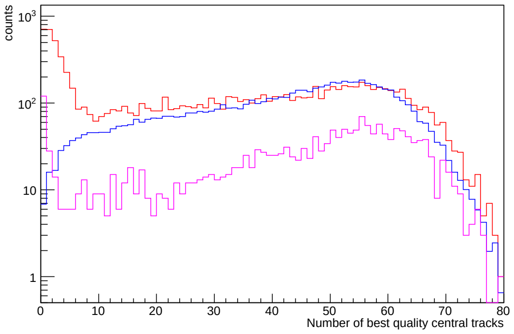

**Figure 5.14:** The $N_{track}$ distributions, UPC(red), MB with ERT2x2(blue), and UPC with $N_{BBCN} = 0 \& N_{BBCS} = 0$ (magenta) are compared. To use a same vertex range, $|z_{ZDC}|$ <30 cm are required for all distributions. The MB distribution is normalized to the UPC distribution from 40 to 100.

The UPC events contain MB-like events and they cannot be removed even by the cut of $N_{BBCN} = 0 \& N_{BBCS} = 0$ as shown in Fig 5.14

It is suspected that the BBC trigger or DAQ has a problem to lose the data time to time. So that the VETO is not able to set online or offline. The fraction of the loss was estimated from the trigger rate and found to be 0.4 %. In UPC triggered events, about 75 % are this un-vetoed events. This doesn't affect in the analysis. Since the veto by $N_{track}$ is robust in removing these events.

### 5.4.3 Event characteristic of triggered events with at least one electron (positron) pair

Event characteristics after selecting electron (positron) pairs are plotted. The distribution of electron pair mass of all data which is taken by UPC trigger in the 2007 PHENIX run without any cut is shown in Fig. 5.15. The red histogram is unlike-sign pair (electron and positron pair) and the blue histogram is like-sign pair (”electron-and-electron” or ”positron-and-positron” pair). It is interesting to note that the invariant mass distribution is almost ideational for like and unlike-sign pairs, except at low mass and $M_{pair}$ >3 GeV. The signal of $J/\psi$ is already seen at this stage. The $N_{track}$ distributions of these events are shown in the Fig 5.16 with mass cut $0.5 - 2.0$ GeV and $< 2.0$ GeV.

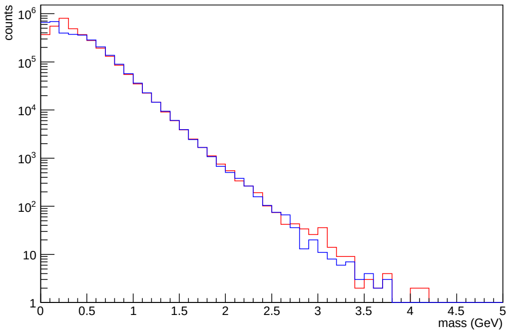

**Figure 5.15:** The distribution of electron pair mass of all data which was taken by UPC trigger in the 2007 PHENIX run without any cut

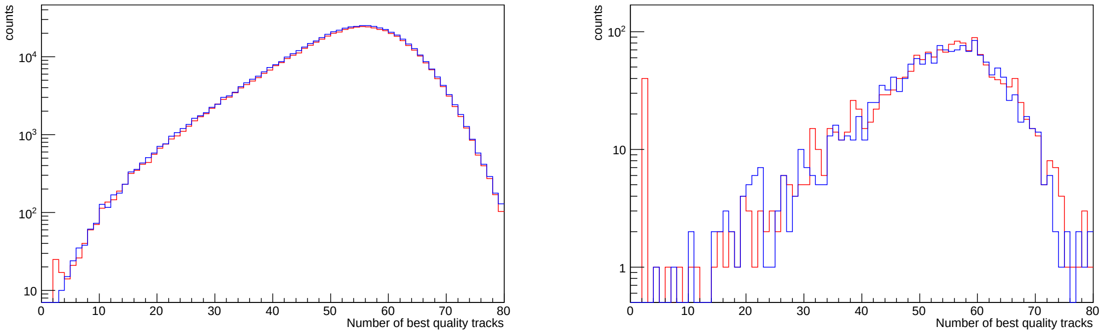

**Figure 5.16:** Left:$N_{track}$ distribution where the events have the pairs with mass from 0.5 to 2.0 GeV. Right:$N_{track}$ distribution where the events have the pairs with mass from 2.0 GeV. Red (blue) line corresponds to unlike (like) sign pair.

There is a peak at $N_{track}$ =2 for the unlike sign pairs. The peak is more separated if a cut on $M_{pair}$ is imposed to select $J/\psi$ area, dicating UPC production of $J/\psi$.

The $N_{track}$ distributions after all cuts except $N_{track}$ =2 are shown in Fig 5.17 Even after

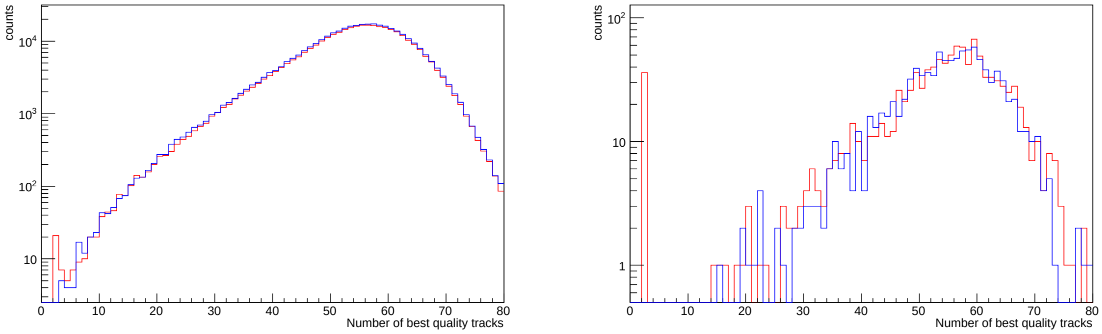

**Figure 5.17:** Left:$N_{track}$ distribution with "$(E_{ZDCN} > 30$ GeV | $E_{ZDCS} > 30$ GeV)& $|z_{PC}| <30$ cm & $(N_{BBCN} =0|N_{BBCS} =0)$" where the events have the pairs with mass from 0.5 to 2.0 GeV . Right:$N_{track}$ distribution with "$(E_{ZDCN} > 30$ GeV | $E_{ZDCS} > 30$ GeV)& $|z_{PC}| <30$ cm & $(N_{BBCN} =0|N_{BBCS} =0)$." where the events have the pairs with mass from 2.0 GeV. Red (blue) line corresponds to unlike (like) sign pair.

reconfirmation of trigger in BBC and ZDC, a large part of high multiplicity events remain, as described in the previous section, there are clearer separation between $N_{track}$ =2 events and high multiplicity events.

## 5.5 The final samples

Finally 252 pairs remained after the all cuts described in Sec. 5.4. Among them 245 events are unlike-pairs. The conditions are summarized as "$(E_{ZDCN} > 30$ GeV $\mid E_{ZDCS} > 30$ GeV(left))&( $|z_{PC}| <$30 cm )& $(N_{BBCN} = 0|N_{BBCS} = 0)$&( $N_{track} = 2$)". The mass and mass-$p_T$ distributions are shown in Fig. 5.18. There are no like-sign pairs above $M_{pair} > 2.0$ GeV. The peak at $M_{pair} = 0$ is likely to be from photon conversion. In $J/\psi$ area, low-$p_T$ component is significant but also high-$p_T$ components can be seen.

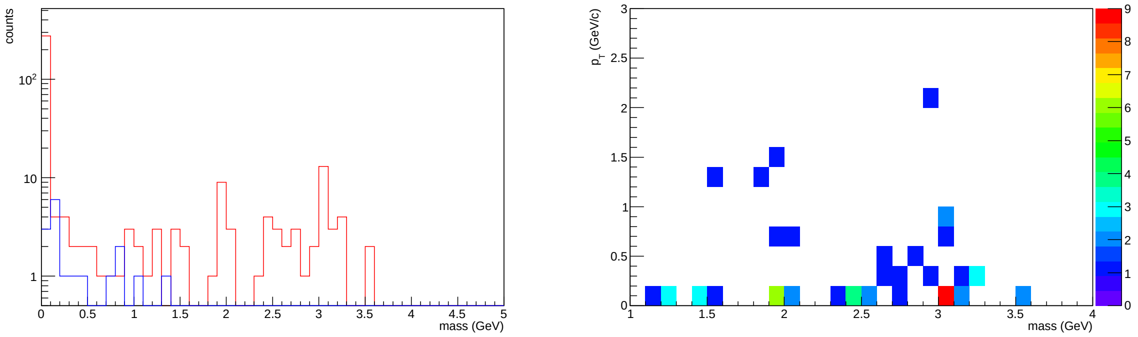

**Figure 5.18:** Left:The distributions of electron pair mass with "$(E_{ZDCN} > 30$ GeV $\mid E_{ZDCS} > 30$ GeV)& $|z_{PC}| <$30 cm & $(N_{BBCN} = 0|N_{BBCS} = 0)$ & $N_{track} = 2$". The red (blue) line corresponds to unlike (like) sign pair. Right: The distributions of electron pair mass and pair $p_T$ with "$(E_{ZDCN} > 30$ GeV $\mid E_{ZDCS} > 30$ GeV)& $|z_{PC}| <$30 cm & $(N_{BBCN} = 0|N_{BBCS} = 0)$ & $N_{track} = 2$".

## 5.6 The background estimation

As shown in Fig 5.15, the contaminated MB events are clearly separated in multiplicity space from UPC signals. Considerable other main background sources for events for $M_{pair}$ 2~4 GeV as follows.

1. $J/\psi$ production from most peripheral collisions.
2. Continuum two photon process, $\gamma\gamma \rightarrow e^{+}e^{-}$ .

### 5.6.1 The contamination from most peripheral collisions

Since 7% of total Au+Au collisions do not hit BBC, there 7% of most peripheral $J/\psi$ events may be accepted by UPC trigger. The number of most peripheral $J/\psi$ is estimated by comparison with p+p collision data taken by the MB trigger. The analysis cuts are as follows.

1. The selection cuts for fiducial cut are same as described in Sec 5.3.
2. The selection cuts for electron identification cut are same as described in Sec 5.1.3.
3. No $E_{ZDCN}$, $E_{ZDCS}$, and $N_{track}$ cuts.

#### The 2006 p+p data

The mass and $N_{track}$ distributions in the 2006 PHENIX run with $L_{int}$=6.2pb$^{-1}$ are shown in Fig 5.19.

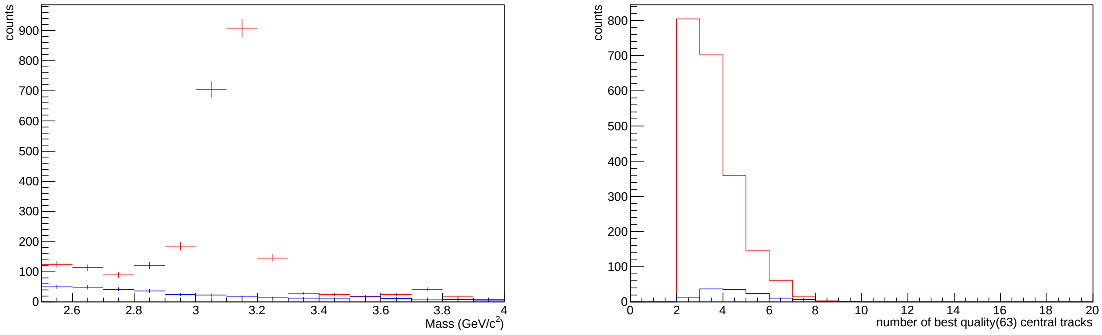

**Figure 5.19:** Left:The distributions of electron pair mass. Right:Its $N_{track}$ distribution where the events have the pairs with mass from 2.7 to 3.5 GeV. The red (blue) line corresponds to unlike (like) sign pairs.

Even in the p+p collisions, the ratio of the number of events with only $J/\psi$ pair those to with $J/\psi$ pair and one or more additional tracks in central arm is about 62% (=804/(2094-804)). Figure 5.20 is a comparison plot of unlike-sign $N_{track}$ distributions of 2007 UPC and 2006 p+p, 2006 data was normalized to have the same value at $N_{track}$ =2. It shows that the samples selected with this UPC selection in Au+Au collision is quite different form those in p+p

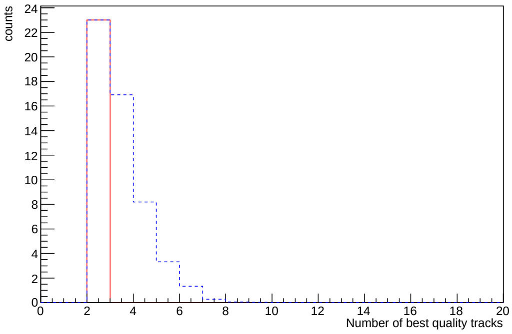

**Figure 5.20:** A comparison plot of unlike-sign $N_{track}$ distributions of 2007 UPC and 2006 p+p.

collision samples. In the latter additional tracks are observed for 60 % of the events, while the selected sample have no additional tracks. This is a strong indication that the selected events are produced from a different mechanism from the incoherent convolution of p+p scattering. The photo induced process $\gamma + Au \rightarrow J/\psi$ + Au is strongly indicated.

**Numerical estimation** For the purpose of reference, contamination from most peripheral are estimated.

The Au+Au run, number of the equivalent p+p collisions which passed ($N_{BBCN}$ =0|$N_{BBCS}$ =0) ($N^{pp}_{pass}$) is calculated as follows;

$$N^{pp}_{pass} = L_{int}\sigma_{Au}\epsilon^{in}N^{col}_{average} = 527 \cdot 10^6/b \times 6.85b \times 0.027 \times 1.73 = 17.5 \times 10^7, \tag{5.3}$$

where $N^{col}_{average}$ is the simulated average number of collisions under the condition of ($N_{BBCN}$ =0|$N_{BBCS}$ =0) [64], $L_{int}$ is the integrated luminosity of the 2007 PHENIX run, and $\epsilon^{in}$ = 0.027 is the simulated over all in efficiency of BBC under the condition of ($N_{BBCN}$ =0|$N_{BBCS}$ =0).

In 2006 PHENIX run, there are about 2k $J/\psi$ events and its integrated luminosity is $L_{int}$=6.2pb$^{-1}$ which corresponds to $2.6 \times 10^{10}$ p+p collisions. Therefore, contamination from most peripheral $J/\psi$ $N_{pair}$ is calculated as following;

$$N_{pair} = \frac{2000}{2.6 \times 10^{10}} \times 17.5 \times 10^7(1 - \epsilon^{pphard}_{BBC}) \sim 0.36, \tag{5.4}$$

where $(1 - \epsilon^{pphard}_{BBC})$ is a correction due to that the efficiency of MB trigger is strongly biased by the evidence of the $J/\psi$ . In this estimation, additional tracks from the other simultaneous collisions are not taken in account.

As shown before, 60% of $J/\psi$ events have additional tracks in p+p collisions. From the fact that the remained events has only 2 tracks. It is concluded that the events from the most peripheral collisions is negligible.

### 5.6.2 Diffractive collisions

As same as UPC events, $J/\psi$ events from diffractive processes are also exclusive. Diffractive $J/\psi$ events can pass the UPC trigger, and may not be included in the p+p samples taken by the MB trigger. The rate of the such events are estimated with PYTHIA [64] monte calro.

**Diffractive process simulation** 100 k diffractive collisions are generated. The setting is as follows.

1. pp 200GeV cms.
2. msel=0 (only specified processes are done).
3. Sub process 92,93 (single diffractive), and 94 (double diffractive).

The simulated distribution of $N_{BBCN}$ and $N_{BBCS}$ is shown in Fig. 5.21. 84% of diffractive collisions are passed VETOBBC. On the other hand, the number of electrons (positrons) and $N_{muon}$ distributions (for the next Chap 6) are shown in Fig 5.22. There are no events with an electron in $10^5$ diffractive events.

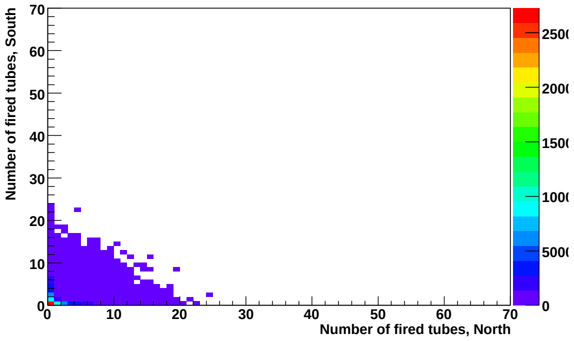

**Figure 5.21:** The distributions of $N_{BBCN}$ and $N_{BBCS}$ for diffractive process. Simulated by PYTHIA.

Since typically 30 % of collisions are diffractive collisions in the energy region, in the 2007 PHENIX run, about $0.3 \times 17.5 \times 10^7 \sim 5 \times 10^7$ diffractive collisions are expected.

It is not enough to make conclusion, but it is very unlikely to have a pair with high mass around $J/\psi$.

### 5.6.3 $\gamma\gamma \rightarrow e^+e^-$

The another possible background events are from UPC two photon process, the $\gamma\gamma \rightarrow e^+e^-$ , which can be source of continuum background.

The contribution of $\gamma\gamma$ is estimated and is shown in this section. As same as the 2004 published cross section calculation, in the simulation STARLIGHT [40] model is used for mass

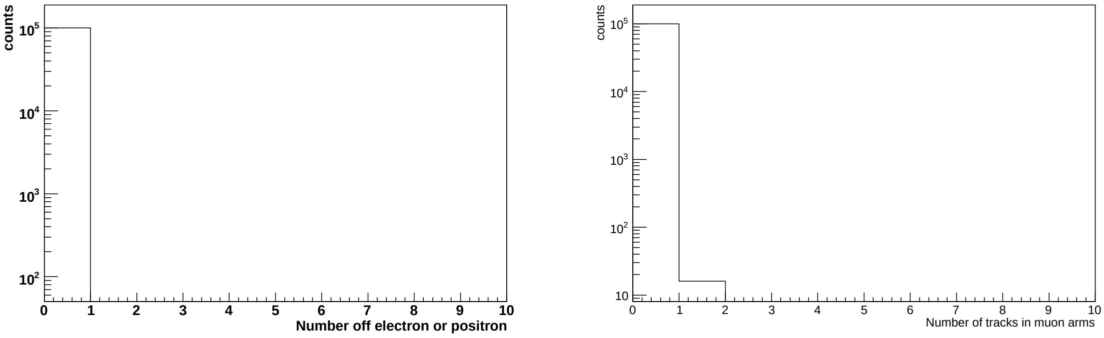

**Figure 5.22:** Left: The distribution of the number of electrons (positrons), Simulated by PYTHIA. Right: The distribution of the *npart_muon* for diffrative process.

distribution shape. The simulated absolute cross section is not used and the absolute cross section of continuum background is determined by data. The following procedure was taken:

1. The generated events are reconstructed with the detector simulation. At this stage the trigger requirement is not imposed.
2. The trigger efficiency of ERT2x2 is imposed and the mass distribution is obtained.
3. Fit $\frac{dN}{dm_{ee}}$ distribution with the $J/\psi$ signal and the obtained continuum mass shape.

The data set has 6M $\gamma\gamma \rightarrow e^+e^-$ events of invariant mass $M > 1$ GeV/c$^2$. Its distributions are given by the STARLIGHT model [40] for coherent production.

The pair mass and $p_T$ distribution are shown in Fig 5.23. The following function is a fitting function of the mass plot.

$$\frac{dN}{dm_{e^+e^-}} = e^{a+bm_{e^+e^-}} \tag{5.5}$$

The parameter $a$ is fixed to reproduce the integrated value, and $b$ is estimated $b = -1.93 \pm 0.052$.

### $\epsilon_{ERT2x2}^{continuum}(m_{e^+e^-})$ (The $p_T$ averaged $\epsilon_{ERT2x2}$ of the continuum process

Assuming BBCLL1, ERT2x2, and ZDC are independent of each other, $\epsilon_{trigger} = \epsilon_{BBCVETO} \cdot \epsilon_{ERT2x2}^{effective} \cdot \epsilon ZDC$, where $\epsilon_{ERT2x2}^{effective}$ is efficiency of ERT2x2 for dielectron pair. For real UPC events, $\epsilon_{BBCVETO}$ and $\epsilon_{ZDC}$ are thought as independent from pair mass and $p_T$ . On the other hand, $\epsilon_{ertt2x2}^{effective}$ obviously depends on $m_{e^+e^-}$, $p_T$ and sector of EMCAL. Since there are low statistics, for continuum, $p_T$ and sector dependency is averaged, then $\epsilon_{ertt2x2}^{effective}$ is treated as a function of $m_{e^+e^-}$, $\epsilon_{ERT2x2}^{continuum}(m_{e^+e^-})$.

The scatter distribution of event by event pair mass and $\epsilon_{ERT2x2}^{continuum}(m_{e^+e^-})$ for STARLIGHT model coherent high-mass $e^+e^-$ continuum is shown in Fig. 5.24. For each event, $\epsilon_{ERT2x2}^{continuum}(m_{e^+e^-})$ is calculated with following equation;

$$\epsilon_{ERT2x2}^{effective} = 1 - (1 - \epsilon_{ERT2x2}^{cluster1}(p_T, sector))(1 - \epsilon_{ERT2x2}^{cluster2}(p_T, sector)), \tag{5.6}$$

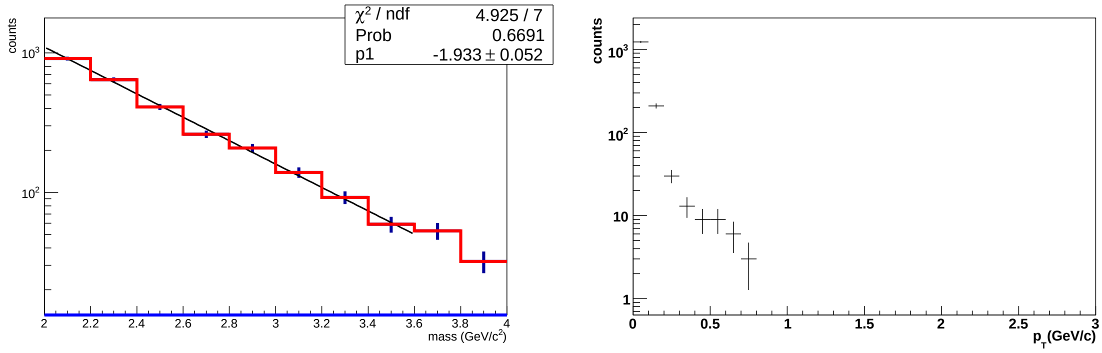

**Figure 5.23:** The simulated data invariant mass of unlike-sign pairs (blue-colored) and like-sign pairs (red-colored) for $N_{electron/positron} == 2$ (left plot). dN/d$p_T$ distribution in [2.0,4.0] (right plot).

where $\epsilon^{cluster}_{ERT2x2}(p_T, sector)$ is a efficiency for single cluster.

The detail on the sector by sector trigger efficiency for single cluster is described in the Correlation factor Section 5.7.4. The central point of the each black cross on Fig 5.24 is the average value of the corresponding $p_T$ bin. The error bars of the black crosses correspond to the RMS values. The averages were fitted with a quadratic function.

$$\epsilon^{e^+e^- continuum}_{ERT2x2} = a \times (m_{e^+e^-} - b)^2 + c.$$

This function is not suited above 3.6 GeV, but there were no data remained in the region.

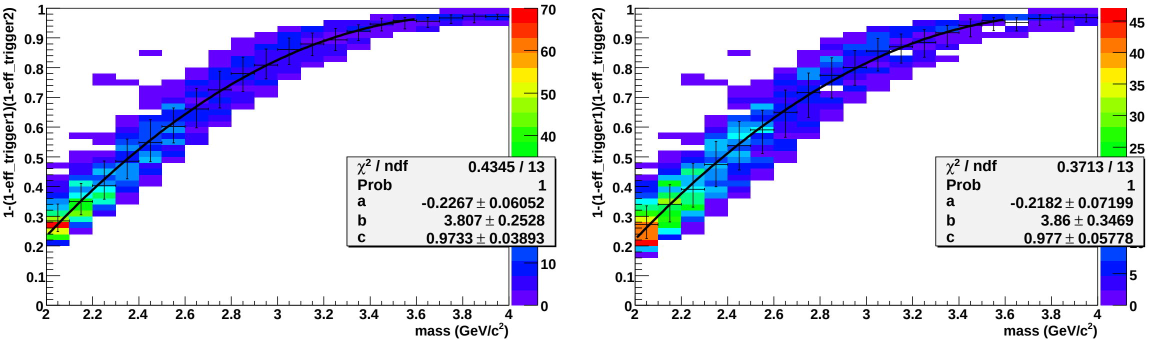

**Figure 5.24:** The scatter plot of$\epsilon_{ERT2x2}$ and $m_{ee}$, and its fitting result with $\epsilon^{continuum}_{ERT2x2}(m_{e^+e^-}) = a \times (m_{e^+e^-} - b)^2 + c$. The left panel is for before run 235000, and the right is for after run 235000.

## 5.7 The correction factors

### 5.7.1 The efficiency of UPC trigger at mid-rapidity ($\epsilon_{trigger}$)

The BBC, ZDC and ERT2x2 triggers can be assumed independent. Then,

$$\epsilon_{trigger} = \epsilon_{ERT2x2}^{effective} \times \epsilon_{BBC_{VETO}} \times \epsilon_{ZDC} \tag{5.7}$$

Details of the efficiency of each trigger are as follows.

### 5.7.2 $\epsilon_{ZDC}$

In PHENIX $\sqrt{s_{NN}} = 200$ GeV measurement, the energy of emitted neutrons can be reasonably thought to be 100 GeV. The resolution $\frac{\delta E}{E}$ of ZDC is 0.3 for this energy, then the ">30 GeV" cuts in the trigger confirmation correspond to 3 $\sigma$ cut. The efficiency of ZDC trigger $\epsilon_{ZDC}$ for event with one neutron can be assumed to be 1. The $\epsilon_{ZDC}$ was assumed 1.

**Acceptance of ZDC** The acceptance of ZDC is $d\theta = 2$ mrad. On the other hand, $p_Z$ of emitted neutrons can be assumed 100 GeV/$c$ , and the Fermi momentum constrains its $p_T$ about 0.25 GeV/$c$ . The 0.25/100 corresponds to 0.25 mrad.

### 5.7.3 $\epsilon_{BBCVETO}$

The central UPC trigger requires VETO on BBC coincidence.

To reduce argument, $\epsilon_{BBCVETO}$ is defined not only efficiency of the online BBCVETO trigger but also the cuts on the BBC charge. Then the BBC offline cut is decided as follows

1. In north or south, the number of BBC tubes whose charge is greater than the charge of one minimum ionized particle is zero.

Even if there are no incident particles in BBC, some amount of charge in the BBC are reconstructed due to a noise. Additionally, even UPC events, existing of weak photons can't be rejected.

Then 'both $N_{BBCN} = N_{BBCS} = 0$' requirement is too strong cut and not imposed in this analysis.

The efficiency loss from BBC trigger is due to the random trigger from noise. It is estimated from the ratio of events which has a charge in one side of BBC, shown in Tab. 5.3.

| * | $N_{BBCN}$==0 | $N_{BBCN}$!=0 |
|---|---|---|
| $N_{BBCS}$ ==0 | 34 | 9 |
| $N_{BBCS}$! =0 | 2 | killed |

**Table 5.3:** The number of correspond events.

If noise hit of the two detectors is uncorrelated, $\epsilon_{BBCVETO}$ is estimated as,

$$1 - \frac{9}{34+9} \times \frac{2}{34+2} = 0.988^{+0.008}_{-0.016} \tag{5.8}$$

### 5.7.4 $\epsilon^{effective}_{ERT2x2}$

The definition of $\epsilon^{effective}_{ERT2x2}$ is the efficiency of the ERT2x2 trigger for a dielectron pair. The threshold value of The ERT2x2 trigger was set to 1 GeV in the 2007 run. However, the turn on curve of ERT2x2 trigger is not the step function. The ERT2x2 trigger efficiency is evaluated for each of all eight sectors as a function of $p_T$ ; ($\epsilon^{cluster}_{ERT2x2}(p_T, sector)$).

**The electron trigger efficiency** The sector by sector trigger efficiency was determined by following method.

1. Using the events taken by the MB trigger, all clusters are searched in offline. For each cluster, it is examined whether the ERT2x2 trigger fired or not. The $dN/dp_T$ distribution for the all clusters and triggered clusters were compared. The typical result is shown in the left panel in Fig 5.25.

2. As seen in the figure, a certain amount of clusters which fires the trigger even their energy are far below the threshold. There are accidentally matching clusters. Assuming all clusters below $p_T < 0.5$ GeV/$c$ are accidental, then the fraction is $\frac{\int_0^{0.5} triggerd}{\int_0^{0.5} all}$ In Fig 5.25, it is considered the accidental tail bit did not depend on $p_T$ , and the fraction of events were subtracted (red line).

3. The ratio of the two histograms was plotted and taken as the efficiency plot. The result is shown in Fig. 5.25 (right).

4. The distribution was fitted with a function $(p0/2) \times erfc(\frac{p1-p_t}{p2})$. p0, p1 and p2 were free parameters (the height, the mean point and the width), where the $erfc$ is the usual complementary error function $\frac{2}{\sqrt{\pi}} \int_x^{inf} exp^{-t^2} dt$.

In this procedure, EMCAL fiducial cut in usual PHENIX $J/\psi$ analysis is applied. However some tiles which are not listed on the fiducial map disarrange the efficiency function, especially for the p0 values. They rarely become hot and return higher $p_T$ value.

Then, the noisy tiles were checked and removed by following procedure. (The new noisy tiles are already applied in Fig 5.25.)

1. Make a tile hit map of each sector and each run with clusters which have over 2 GeV. A typical result is shown in Fig 5.26.

2. Remove noisy tiles by seeing. The list is shown in Tab. 5.4. The result to which is applied the new noisy list is shown in Fig 5.26.

Figures 5.27, 5.28, and 5.29 show run dependence of the p0, p1, p2 values for all sectors. The values for sector 0∼5 were stable. However, the parameters of sector 6 and 7 changed at

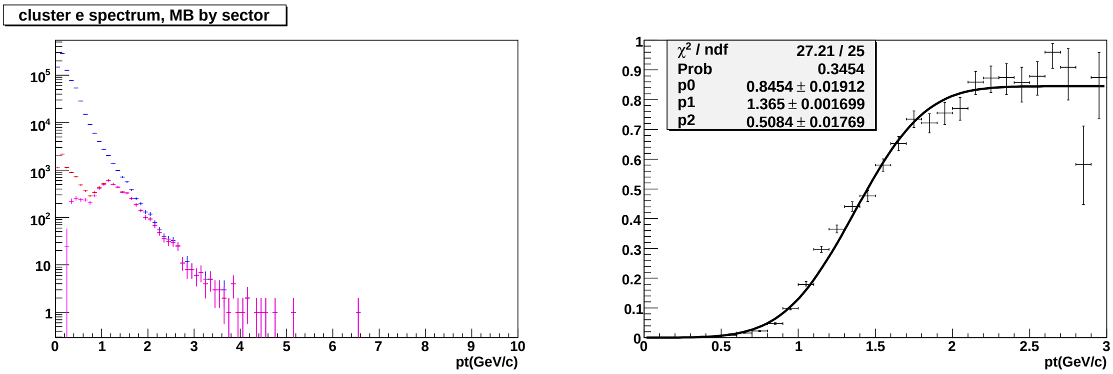

**Figure 5.25:** Left:The MB (BLUE), ERT2x2 (RED) and subtracted ERT2x2 (magenta) triggered cluster $dN/dp_T$ distributions at sector0 in run231155. Right: ERT2x2 turn on curve at sector0 in run231155.

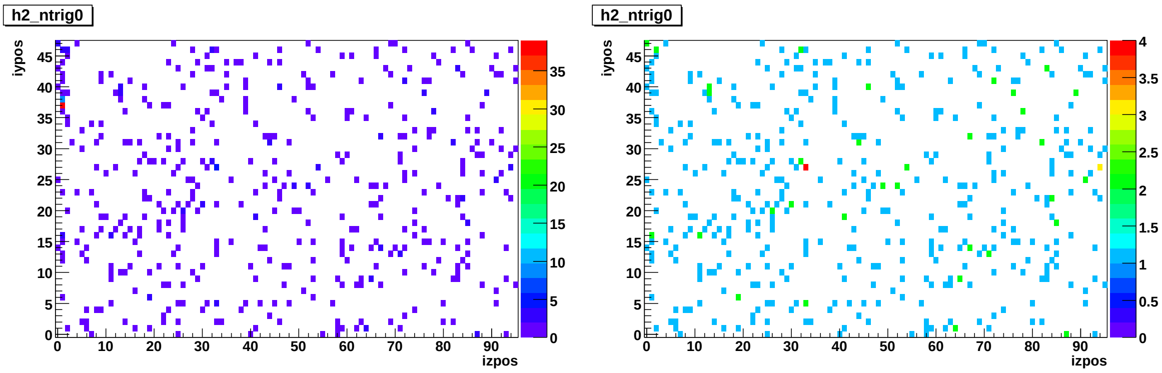

**Figure 5.26:** Left:$p_T > 2$GeV hit map with only fiducial cut in [63] at run231155 sector0. Right:$p_T > 2$GeV hit map with new noisy list at run231155 sector0.

**Table 5.4:** The noisy tower list

| sector | izpos | iypos |
|---|---|---|
| 0 | 1 | 38 |
| 0 | 1 | 46 |
| 1 | 92 | 15 |
| 1 | 94 | 42 |
| 1 | 94 | 43 |
| 1 | 95 | 41 |
| 1 | 95 | 44 |
| 1 | 95 | 45 |
| 2 | 42 | 34 |
| 3 | 58 | 18 |
| 3 | 60 | 19 |
| 3 | 61 | 19 |
| 5 | 16 | 4 |
| 6 | 2 | 7 |
| 6 | 2 | 7 |
| 7 | 8 | 32 |
| 7 | 8 | 33 |
| 7 | 8 | 34 |
| 7 | 8 | 35 |
| 7 | 9 | 31 |
| 7 | 9 | 32 |
| 7 | 9 | 33 |
| 7 | 9 | 34 |
| 7 | 9 | 35 |
| 7 | 12 | 32 |
| 7 | 12 | 33 |
| 7 | 13 | 32 |
| 7 | 13 | 33 |
| 7 | 14 | 34 |
| 7 | 57 | 0 |
| 7 | 68 | 29 |
| 7 | 68 | 34 |
| 7 | 69 | 34 |
| 7 | 69 | 16 |
| 7 | 51 | 6 |

run 235000. Therefore the runs were divided into two groups. Finally, 5.27, 5.28, and 5.29 were projected to its Y-axis and get their MEAN and RMS values. The results are shown in Tab. 5.5.

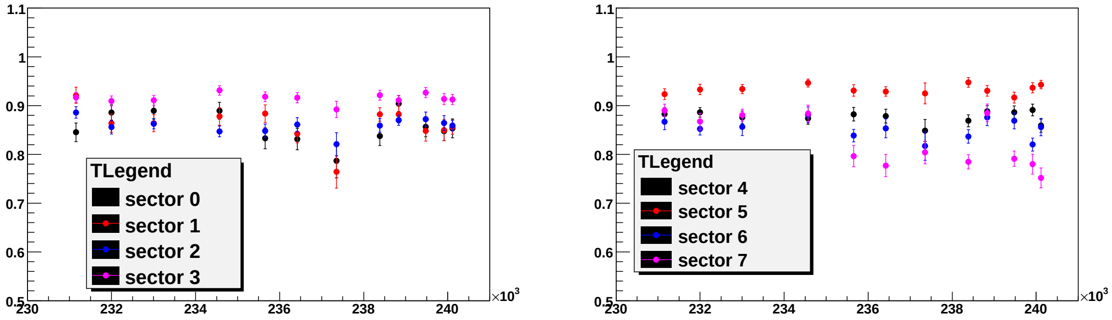

**Figure 5.27:** Thep0 values for each sector and run.

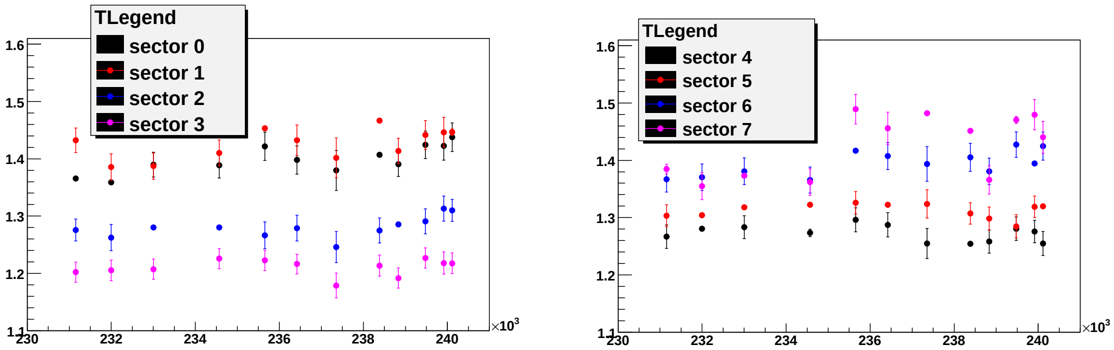

**Figure 5.28:** The p1 values for each sector and run.

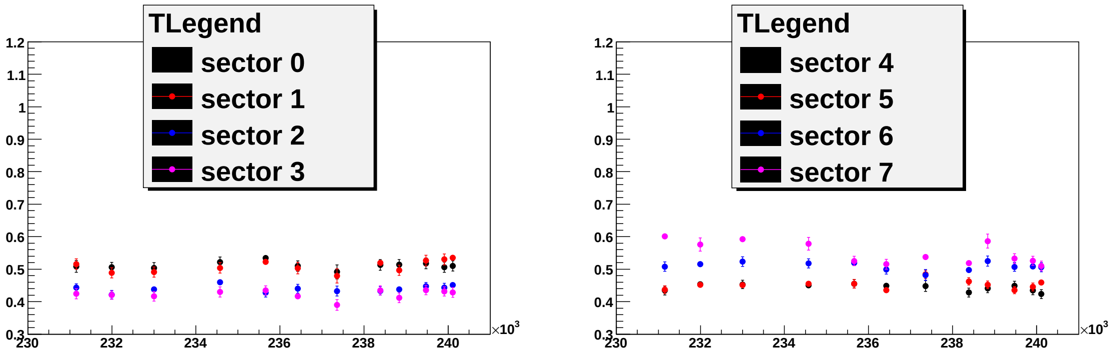

**Figure 5.29:** The p2 values for each sector and run.

**Table 5.5:** The projection result of Fig 5.27 5.28 5.29.

| | MEAN | RMS |
|---|---|---|
| sector 0,p0 | 0.854 | 0.0314 |
| sector 0,p1 | 1.39 | 0.0235 |
| sector 0,p2 | 0.511 | 0.0100 |
| sector 1,p0 | 0.861 | 0.0357 |
| sector 1,p1 | 1.42 | 0.0252 |
| sector 1,p2 | 0.509 | 0.0172 |
| sector 2,p0 | 0.858 | 0.0153 |
| sector 2,p1 | 1.28 | 0.0178 |
| sector 2,p2 | 0.439 | 0.00996 |
| sector 3,p0 | 0.914 | 0.00932 |
| sector 3,p1 | 1.21 | 0.0137 |
| sector 3,p2 | 0.422 | 0.0125 |
| sector 4,p0 | 0.876 | 0.0121 |
| sector 4,p1 | 1.27 | 0.0136 |
| sector 4,p2 | 0.443 | 0.0102 |
| sector 5,p0 | 0.932 | 0.00895 |
| sector 5,p1 | 1.31 | 0.0121 |
| sector 5,p2 | 0.452 | 0.0129 |
| sector 6 $run23500 <$,p0 | 0.864 | 0.0110 |
| sector 6, $run23500 <$p1 | 1.37 | 0.00598 |
| sector 6 $run23500 <$,p2 | 0.516 | 0.00558 |
| sector 6 $run23500 >$,p0 | 0.8458 | 0.0200 |
| sector 6 $run23500 >$,p1 | 1.40 | 0.0152 |
| sector 6 $run23500 >$,p2 | 0.505 | 0.0125 |
| sector 7 $run23500 <$,p0 | 0.880 | 0.00838 |
| sector 7 $run23500 <$,p1 | 1.36 | 0.0112 |
| sector 7 $run23500 <$,p2 | 0.586 | 0.0104 |
| sector 7 $run23500 >$,p0 | 0.796 | 0.0365 |
| sector 7 $run23500 >$,p1 | 1.45 | 0.0369 |
| sector 7 $run23500 >$,p2 | 0.531 | 0.0224 |

**The efficiency to trigger the dielectron events($\epsilon_{ert2x2}^{effective}$)**

The efficiency of dielectron depends on the mass, $p_T$ , and decay angle of the dielectron system, so that it is model dependent. The procedure is discussed in the Sec. 5.7.4.

### 5.7.5 The luminosity $L_{int}$

**Checking triggers**

**The integrated luminosity**

Total count of BBCLL1 triggers in the good run list is $3.32426 \times 10^9$. So the integrated Luminosity in the analysis is

$$L_{int} = \frac{N_{BBCLL1analyzed}}{\sigma_{AuAu} \times \epsilon_{BBC}} = \frac{3324 \cdot 10^6}{6.85 \text{ b} \times 0.92} = 527.45 \pm 23 \ \mu\text{b}^{-1} \tag{5.9}$$

Since the efficiency of the ERT2x2 is described in Sec. 5.7.4, the good run list is divided into two groups, before($N_{BBCLL1analyzed} = 0.953181 \times 10^9$) and after($N_{BBCLL1analyzed} = 2.37108 \times 10^9$) run 235000.

**Systematic error from vertex detectors** In standard PHENIX analysis, luminosity is counted by BBCs, and the *zvtx* is measured by the BBC. On the other hand, in this analysis, luminosity is counted by the BBC, but the *zvtx* is measured by PC or ZDC. The systematic error is estimated by following method.

1. Make a Gaussian distribution with its $\sigma$= 25 cm (as same as the typical $z_{BBC}$ distribution) and define its area with ±30 cm cut as A.
2. At ±100 cm, divide the original distribution into 2000 bins. Then make 2000 new Gaussian distribution. Their center point is defined as central of each bin, their integrated values are defined as the area of the original distribution in the bin, and their $\sigma$ is defined as $\sigma_{z_{PC}1}$ (or $\sigma_{z_{ZDC}}$)
3. Integrate new distributions with the range of ±30 cm and the integrated area is defined as B.
4. $(A - B)/A$ can be treated as systematic errors.

By the method $(A - B)/A$ for $z_{PC}$ is just 0.002 and for $z_{ZDC}$ is just 0.005. Therefore, no extra errors is considered from the different vertex measurement.

## 5.8 Trigger and detector efficiency calculation($\epsilon^{effective}_{ert2x2}$ and $(Acc \cdot \epsilon_{reco} \cdot \epsilon_{cuts})$)

As shown in Fig 5.24, $\epsilon^{continuum}_{ERT2x2}$ has already been calculated for the $\gamma\gamma \rightarrow e^+e^-$. The effect of $(Acc \cdot \epsilon_{reco} \cdot \epsilon_{cuts})$ is already taken into account in Fig 5.23. Due to $p_T$ dependence, another calculation for the $(Acc \cdot \epsilon_{reco} \cdot \epsilon_{cuts})$ of $J/\psi$ and the $\epsilon^{J/\psi}_{ERT2x2}$ are needed.

### 5.8.1 The simulation of $J/\psi$

For the coherent $J/\psi$ case, due to the spin conservation, the STARLIGHT model for the coherent $J/\psi$ assume $\lambda = 1$ polarization. The $\lambda$ is polarization factor, 1 means full transverse polarization and -1 is full longitudinal polarization. For the incoherent $J/\psi$ case, there are theoretical uncertainty. The $\lambda$ can take one to zero. Typically, the polarization measurement requires a large number of events. The $\lambda$ of UPC $J/\psi$ can't be determined with this experimental data. Then

1. Unpolarized and transversely polarized $J/\psi$ particles are generated in monte carlo with a flat distribution in $\psi$, y and $p_T$ space in the regions [0,2$\pi$], [-0.5,0.5] and [0,3.0], respectively.

2. They are fed to the detector simulation, the reconstruction program, and offline cuts. In total, there are 240 M events.

3. The events are weighted on $p_T$ and used for the calculation of detector acceptance, $(Acc \cdot \epsilon_{reco} \cdot \epsilon_{cuts})$ and the trigger efficiency $\epsilon^{J/\psi}_{ERT2x2}(p_T)$.

4. Since the coherent production is dominant for $p_T < 0.4$ GeV/$c$ , For $p_T > 0.4$ GeV/$c$ , both unpolarized and transversely polarized data qre used. Their average value is taken as the central value and the difference is taken as the systematic uncertainty.

#### The simulated invariant mass distribution

The simulated invariant mass distributions and a fitting result with a single-Gaussian is shown in Fig. 5.30.

However, their $\chi^2/NDF$ are not so good because of tail of $J/\psi$. In usual PHENIX central arm $J/\psi$ analysis, double-Gaussian is used as a fitting function for $J/\psi$. For example, the fitting results with double-Gaussian is shown in Fig. 5.31. They have better $\chi^2/NDF$ , especially realistic transversely polarized case. On the other hand, they have too many free parameters for the real invariant mass distribution. Additionally, since there is no $z_{BBC}$ information, $\sigma$ values will be changed, then the $\sigma$ values can't be fixed to $\sigma$ values of $J/\psi$ in another measurement, for example $\sigma$ of p+p $J/\psi$. Therefore single-Gaussian is used in this thesis.

**$p_T$ resolution and bin size** The width of $J/\psi$ mass distribution in p+p data are consistent with the width of the simulated distribution. So that resolution is well measured in the monte calro. The simulated reconstructed $p_T$ distributions of $e^+e^-$ pairs from $J/\psi$ pairs with generated $p_T$ , 0.0∼0.01, 0.5∼0.51 (Red), 1.0∼1.01 (blue), and 2.0∼2.01GeV/$c$ , are shown in Fig. 5.32.

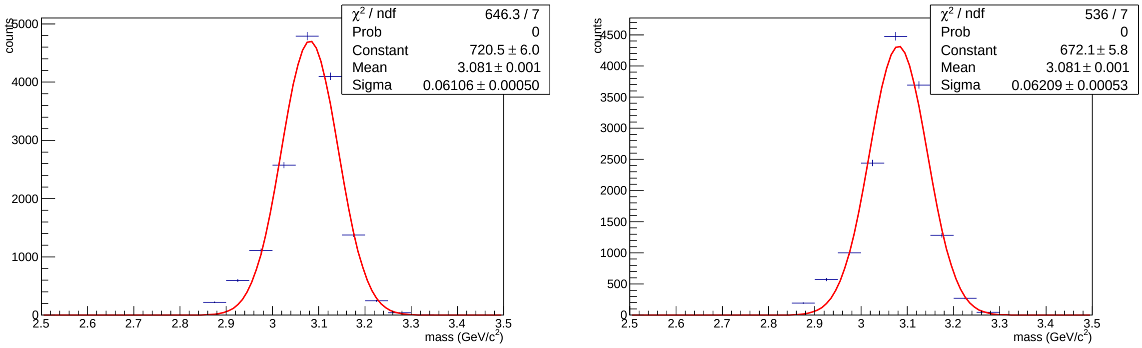

**Figure 5.30:** Left: The simulated full transversely polarized case invariant mass distributions and the single-Gaussian fitting results. Right: The simulated unpolarized case invariant mass distributions and the single-Gaussian fitting results.

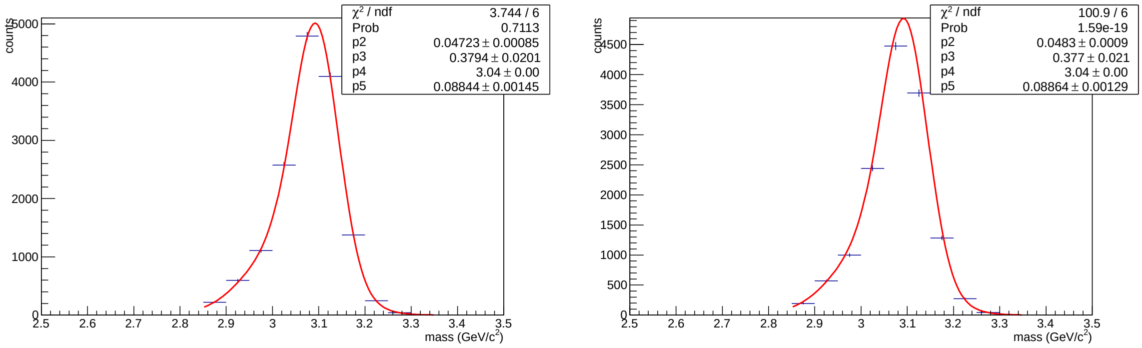

**Figure 5.31:** The simulated invariant mass distribution and the double-Gaussian fitting results. The left panel is the full transversely polarized case and the right one is the unpolarized case.

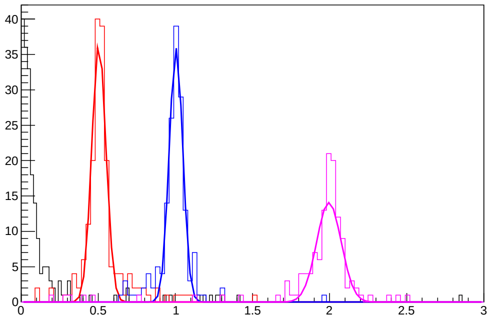

**Figure 5.32:** The simulated reconstructed $p_T$ distributions of $e^+e^-$ pairs from $J/\psi$ with generated $p_T$ , 0.0∼0.01, 0.5∼0.51 (Red), 1.0∼1.01 (blue), and 2.0∼2.01, GeV/$c$ .

Simulated $p_T$ resolutions are 60~80 MeV/c. The used bin sizes, 200 MeV/c, are large enough than the resolutions.

### $p_T$ weighting function

There is no well accepted theoretical prediction on $p_T$ distribution of UPC $J/\psi$ production. Therefore, $p_T$ distribution of $J/\psi$ in p+p collision at $\sqrt{s_{NN}} = 200$ GeV is used as a template. The $(1/2\pi p_T)d^2N/dp_Tdy$ $[(\mathrm{GeV}/c)^{-2}]$distribution at p+p $\sqrt{s_{NN}} = 200$ GeV is shown in Fig. 5.33. The distribution was fitted

$$p_0(1 + p_T/p_1)^{-6} \tag{5.10}$$

The $p_1$ value is 3.905 GeV/c.

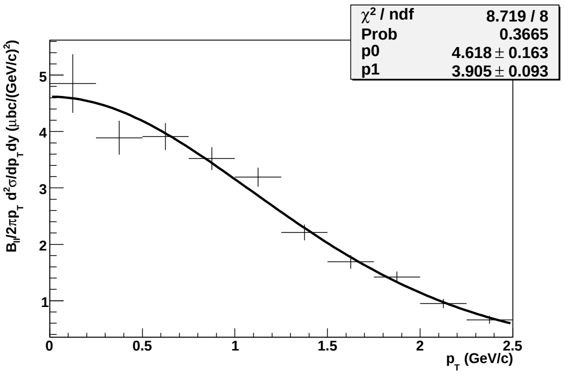

**Figure 5.33:** The black crosses correspond to $(1/2\pi p_T)d^2N/dp_Tdy$ $[(\mathrm{GeV}/c)^{-2}]$of $J/\psi$ in p+p collisions [70]. Fitting function is $p_0(1 + p_T/p_1)^{-6}$

### The $p_T$ dependence of $(Acc \cdot \epsilon_{reco} \cdot \epsilon_{cuts})$

The $(Acc \cdot \epsilon_{reco} \cdot \epsilon_{cuts})$ of the transversely polarized and unpolarized cases is shown in Fig. 5.34. For the final calculation, $(Acc \cdot \epsilon_{reco} \cdot \epsilon_{cuts})$ of the transversely polarized case is used in $p_T < 0.4$ GeV/$c$ , the averaged values are used in $p_T > 0.4$ GeV/$c$ . The definition of $(Acc \cdot \epsilon_{reco} \cdot \epsilon_{cuts})$ is follows.

$$\frac{\sum_{p_T^{reco} \in bin}(1 \times w(p_T^{reco} \in bin))}{\sum_{p_T^{generated} \in bin}(1 \times w(p_T^{generated} \in bin))}, \tag{5.11}$$

where $p_T^{reco}$ is the reconstructed $p_T$ and $p_T^{generated}$ is the generated $p_T$ value of a truck.

### The $p_T$ dependence of $\epsilon_{J/\psi}^{ERT2x2}$

The results of the polarized case and unpolarized case are shown in Fig. 5.35 and Fig. 5.36. Bin by bin $\epsilon_{effective}^{ERT2x2}$ are calculated by following equation

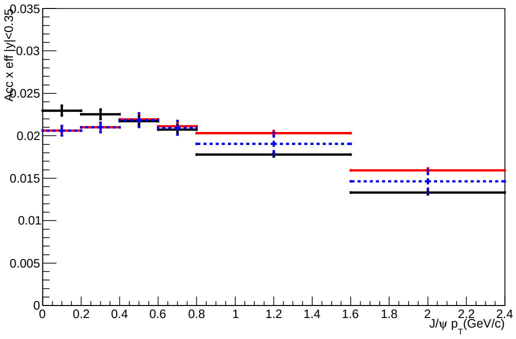

**Figure 5.34:** The $p_T$ dependence of simulated Acc × efficiency of transverse polarized (Red line) and unpolarized (Black line) case. The blue line is the actually used Acc × efficiency.

$$\frac{\sum_{p_T^{reco}\in bin}(1-(1-\epsilon_{ERT2x2}^{track1}(p_T^{reco},sector))(1-\epsilon_{ERT2x2}^{track2}(p_T^{reco},sector))\times w(p_T^{reco}\in bin))}{\sum_{p_T^{reco}\in bin}(1\times w(p_T^{reco}\in bin))} \tag{5.12}$$

Please note there are two run groups. The averaged value will be used to calculate $\frac{B_{ee}d^2\sigma_{J/\psi}}{2\pi p_T dp_T dy}$.

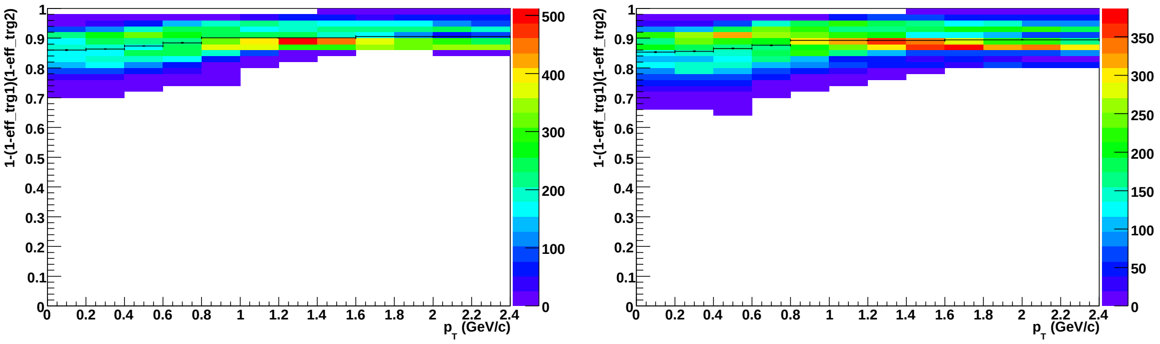

**Figure 5.35:** Left:The $p_T$ dependence of $\epsilon_{effective}^{ERT2x2}$ for transverse polarized $J/\psi$ at before run23500. Right:The $p_T$ dependence of $\epsilon_{effective}^{ERT2x2}$ for transverse polarized $J/\psi$ at after run23500. Please note scatter plot was not weighted because of to help seeing.

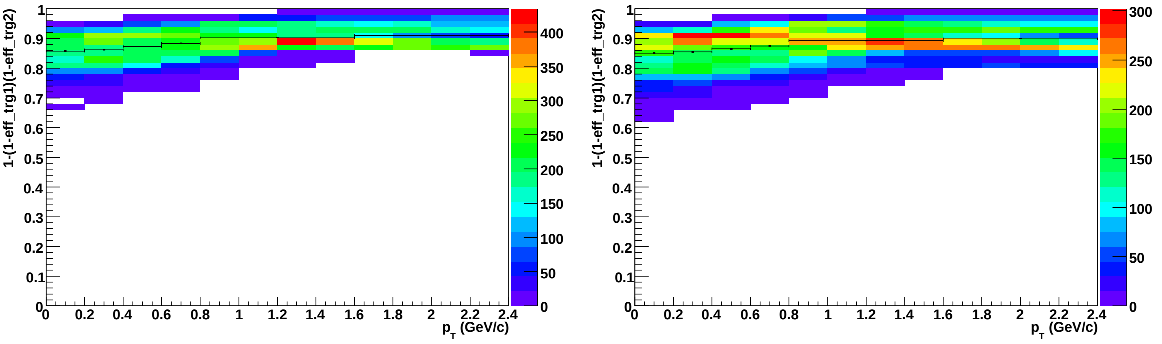

**Figure 5.36:** Left:The $p_T$ dependence of $\epsilon^{ERT2x2}_{effective}$ for unpolarized $J/\psi$ at before run23500. Right:The $p_T$ dependence of $\epsilon^{ERT2x2}_{effective}$ for unpolarized $J/\psi$ at after run23500.

## 5.9 The cross-section measurement

### 5.9.1 The extraction of number of $J/\psi$ ($N_{J/\psi}$)

As described in final sample Sec. 5.5, the invariant mass distribution is shown in Fig. 5.18 (left).

As described in this section, $dN/dM_{ee}$ $\gamma\gamma \to e^+e^-$ are determined by STARLIGHT [40] MC with the acceptance and trigger efficiency correction. Since the efficiency changed after run 23500, the shapes are different before and after two run groups. Luminosity weighted distribution is used.

Then the shape is described by following function.

$$\frac{dN}{dm_{e^+e^-}} = e^{A+slope\cdot m_{e^+e^-}} \cdot \frac{N_{evt}(<23500)(a0 \times (m_{e^+e^-} - b0)^2 + c0) + N_{evt}(>23500)(a1 \times (m_{e^+e^-} - b1)^2 + c1)}{N_{evt}(full)} + \frac{B}{\sqrt{2\pi}\cdot\sigma} \cdot e^{-0.5\cdot(m_{e^+e^-}-3.096)^2/\sigma^2}, \tag{5.13}$$

where a0, b0, c0, a1, b1, c1 (0 means for before run 235000, 1 means after run 235000 ) were listed in Table 5.5, and $A$ and $B$ are the fitting parameters. The fitting result is $\sigma = 74 \pm 23$ MeV/c$^2$ and $N_{J/\psi} = 16.2 \pm 4.7$ with fitting range $2.0 < M_{pair} < 4.0$ GeV.

### The $p_T$ distribution of $J/\psi$

The $m_{e^+e^-}$ distribution with the fit is shown in Fig 5.37. Its $\frac{dN}{dp_T}$ distribution within the three sigma around the $J/\psi$ , $3.096 \pm 3 \times 0.074$ GeV/$c^2$ , is shown in the right panel. The distribution includes not only $J/\psi$ $e^+e^-$ pairs, but also continuum $e^+e^-$ pairs.

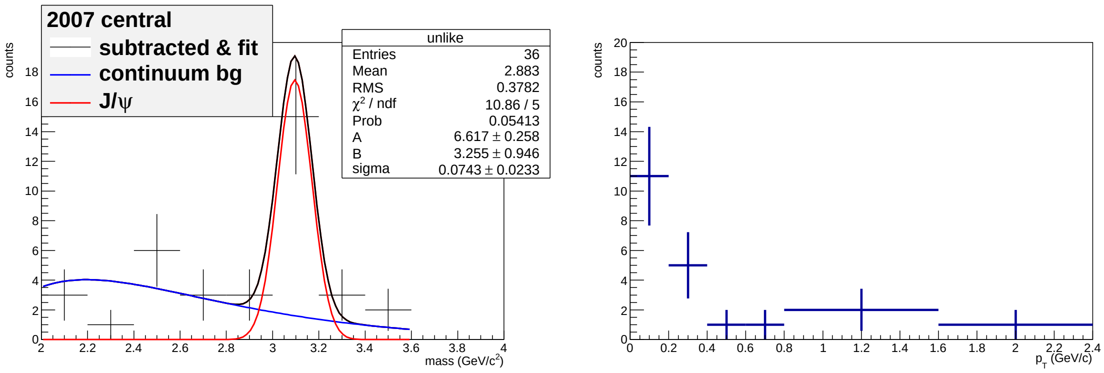

**Figure 5.37:** Left:The real data $dN/dm_{ee}$ plots. The fitting function is shown as the black line. The blue line is continuum $e^+e^-$ part. The red line is $J/\psi$ part. Right:The $p_T$ distribution within $J/\psi$ area (3 $\sigma$).

The $p_T$ distribution in the mass range in the STARLIGHT simulation is shown in Fig. 5.38.

The normalization is made from the continuum contribution in the fit. Total continuum contribution integrated over $p_T$ is 5.4 counts. The errors are decided by following equation.

The $p_T$ distribution after subtracting the background (Fig 5.38) is shown in Fig. 5.39. The errors are estimated as;

$$err^2_{subtracted} = err^2 + err^2_{continuum} \tag{5.14}$$

The result is summarized in Tab. 5.6

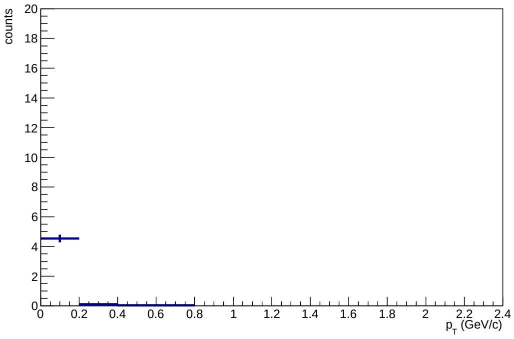

**Figure 5.38:** The continuum pair $p_T$ distribution within $3.096 \pm 3 \times 0.074$ GeV/$c^2$ using STARLIGHT model [40]

.

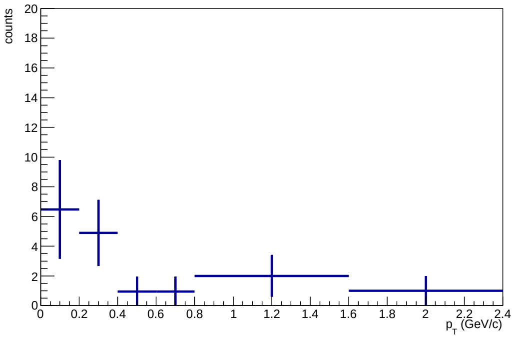

**Figure 5.39:** The subtracted pair $p_T$ distribution.

### The systematic uncertainties of the fitting

The systematic uncertainties are considered for the following items.

1. Each sector by sector turn on curve has three parameters; amplitude, p0, p1 and p2. The three (times eight sectors times two run groups) values are modified by random Gaussian distribution, with the mean and RMS shown in Tab 5.5. If the amplitude become over 1, it is set to 1.

**Table 5.6:** The count in each $p_T$ bins of the original, normalized continuum $e^+e^-$,and subtracted.

| $p_T$ (GeV/c) | original | normalized continuum $e^+e^-$ | subtracted |
|---|---|---|---|
| 0.0-0.2 | 11.4±3.3 | 4.5±0.2 | 6.5±3.3 |
| 0.2-0.4 | 5±2.2 | 0.1± 0.004 | 4.9±2.2 |
| 0.4-0.6 | 1±1.0 | 0.4 ±0.003 | 0.95±1.0 |
| 0.6-0.8 | 1 ±1.0 | 0.4 ±0.003 | 0.95±1.0 |
| 0.8-1.6 | 2±1.4 | - | 2±1.4 |
| 1.6-2.4 | 1 ±1.0 | - | 1±1 |

2. Exponential curve has just one parameter, slope. The slope is set the same method.
3. Remake Eq.5.17.

The distribution of 300 random shifted functions and corresponding number of $J/\psi$ are shown in Fig 5.40. Therefore, systematic error was set to 0.26 counts.

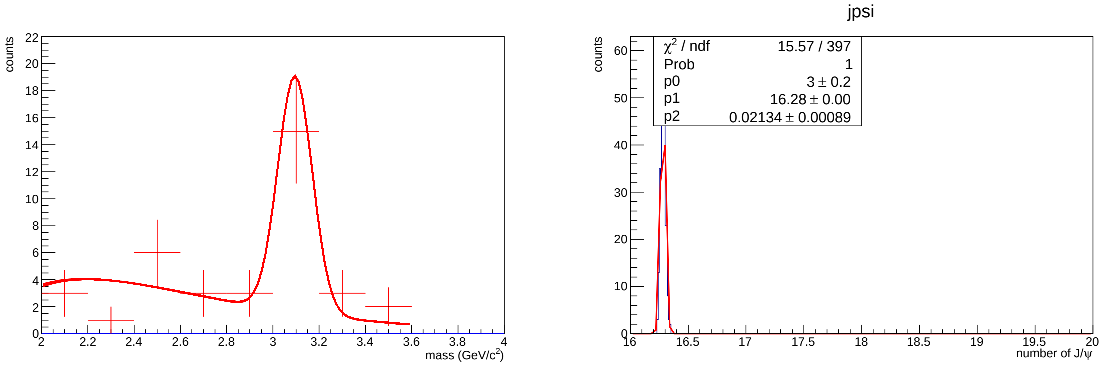

**Figure 5.40:** Left :The 300 times random fitting results. Right:corresponded number of $J/\psi$ distribution.

**UPC $\psi(2s)$** Contribution of UPC $\psi(2s)$ is expected, however there are too low statistics to measure its contribution. HERA reported 2% $\psi(2s)$ contribution in $\gamma p \rightarrow J/\psi$ measurement (for $J/\psi \rightarrow \mu^+\mu^-$, 7%) [66]. If force 2% $\psi(2s)$ contribution in the fitting procedure, its systematic error is enough lower than the statistical error.

### 5.9.2 The double differential cross section

The $J/\psi$ cross section for Au+Au→ Au*+Au*+$J/\psi$ + $k$ neutrons($k > 0$) integrated in a given rapidity and the transverse momentum bin is calculated according to,

$$\frac{d^2\sigma_{J/\psi}}{2\pi p_T dp_T dy} = \frac{1}{2\pi p_T B_{ee} \Delta p_T \Delta y} \frac{N_{J/\psi}}{(Acc \cdot \epsilon_{reco} \cdot \epsilon_{cuts}) \cdot \epsilon_{trigger} \cdot \mathcal{L}_{int}}, \tag{5.15}$$

where $B_{ee}$ is the $J/\psi$ $e^+e^-$ branching ratio, $N_{J/\psi}$ is the measured $J/\psi$ yield, $\mathcal{L}_{int}$ is the integrated luminosity, $527.45 \pm 23$ $\mu$b$^{-1}$, $\Delta y$ is 1. The middle point of the each $p_T$ bins is used for the $p_T$.

The $p_T$ dependency of $(Acc \cdot \epsilon_{reco} \cdot \epsilon_{cuts}) \cdot \epsilon_{trigger}$ are shown in Fig 5.34, 5.35, 5.36.

**Summary of systematic Uncertainly**

The total systematic error was calculated by following equation.

$$\frac{\epsilon_{totalsys}}{\sigma} = \sqrt{\left(\frac{\epsilon_{Acc\times\epsilon}}{Acc \times \epsilon}\right)^2 + 0.115^2_{sim\epsilon} + \left(\frac{\epsilon_{L_{int}}}{L_{int}}\right)^2 + \left(\frac{\epsilon_{\epsilon^{eff}_{ERT2x2}}}{\epsilon^{eff}_{ERT2x2}}\right)^2 + \left(\frac{Njpsi_{sys}}{Njpsi}\right)^2 + \left(\frac{\epsilon_{\epsilon_{BBCVETO}}}{\epsilon_{BBCVETO}}\right)^2} \tag{5.16}$$

Where,

1. Type A and B:$Njpsi_{sys}$ is the systematic error of $J/\psi$ counting, shown in Fig 5.40
2. Type B:$\epsilon_{Acc\times\epsilon}$ is the systematic error in Fig 5.34. The sources were simulation statistical error and $\frac{|pol-nonpol|}{2}$
3. Type B:$0.115^2_{simerr}$ is the systematic error of the simulation itself [63].
4. Type B:$\epsilon_{L_{int}}$ is the statistical error of integrated luminosity.
5. Type B:$\epsilon_{\epsilon^{effecitve}_{J/\psi}}$ is the systematic error of $\epsilon^{effective}_{J/\psi}$, shown in Fig 5.35 and 5.36
6. Type B:$\epsilon_{\epsilon_{BBCVETO}}$ is the statistical error to estimate $\epsilon_{BBCVETO}$.

The type A systematical errors are the point to point uncorrelated systematical errors. The type B systematical errors are correlated errors. For example, systematic errors from UPC $J/\psi$ polarization affects in all bins coherently.

### 5.9.3 Result

The result is shown in Fig. 5.41 and Tab. 5.7.

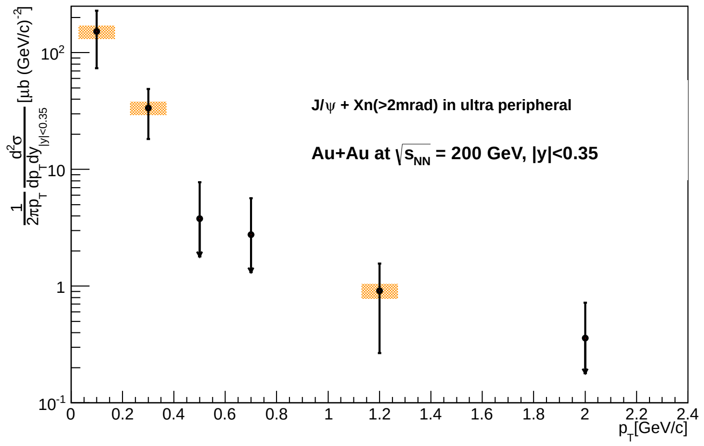

**Figure 5.41:** The $(1/2\pi p_T)d^2N/dp_Tdy$ [(GeV$/c)^{-2}$]distribution in Ultra-Peripheral Au-Au Collisions at $\sqrt{s_{NN}}$ = 200 GeV in the 2007 run.

**Table 5.7:** The $(1/2\pi p_T)d^2N/dp_Tdy$ [(GeV$/c)^{-2}$]in Ultra-Peripheral Au-Au Collisions at $\sqrt{s_{NN}}$ = 200 GeV in the 2007 run.

| $p_T$ (GeV/c) | $(1/2\pi p_T)d^2N/dp_Tdy$ [(GeV$/c)^{-2}$] | statistical error | systematic error |
|---|---|---|---|
| 0.0-0.2 | 152 | 78 | 19.3 |
| 0.2-0.4 | 33.6 | 15.3 | 4.25 |
| 0.4-0.6 | 3.79 | 3.96 | 0.489 |
| 0.6-0.8 | 2.76 | 2.89 | 0.358 |
| 0.8-1.6 | 0.913 | 0.646 | 0.13 |
| 1.6-2.4 | 0.358 | 0.358 | 0.0532 |

### 5.9.4 The integrated Cross section for coherent UPC $J/\psi$ production at mid-rapidity

The integrated cross section is calculated as follows;

$$\Sigma_{bin}\Delta p_T\left(\frac{d^2\sigma_{J/\psi}}{\Delta p_T dy}\right). \tag{5.17}$$

Its systematic error is calculated as follows;

$$\Sigma_{bin}\left(\frac{sys_{ith}}{d\sigma/dy_{ith}}\right), \tag{5.18}$$

where $d\sigma/dy_{ith}$ is the $d\sigma/dy$ of $i$th bin and $sys_{ith}$ is its systematic error.

The result is $45.6 \pm 13.3\,(\text{stat}) \pm 5.9\,(\text{sys})\ \ \mu\text{b}$. The cross-section compared to theoretical curves [40, 38, 41, 42, 42, 43] and results obtained by the year 2004 runs($76 \pm 31\,(\text{stat}) \pm 11\,(\text{sys})\ \ \mu\text{b}$) is shown in Fig. 5.42.

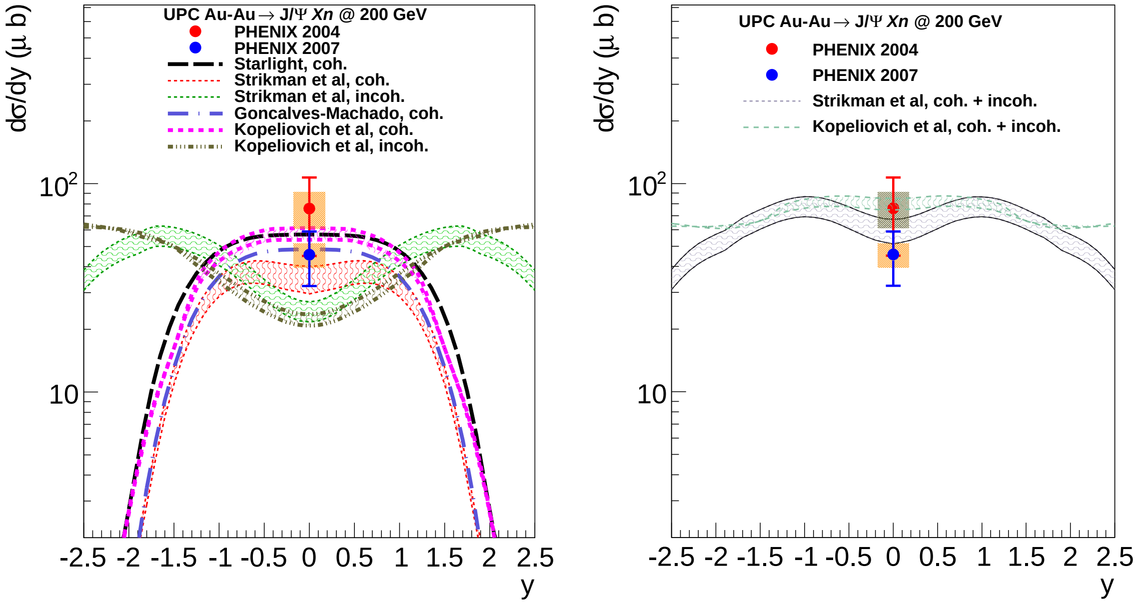

**Figure 5.42:** The measured cross-section compared to theoretical [40, 38, 41, 42, 42, 43] and the 2004 result.

The combined result of the two measurements is $55.9 \pm 13.2\,(\text{stat}) \pm 7.6\,(\text{sys})\ \ \mu\text{b}$. The systematic error of 2004 and 2007 are assumed as independent. The 2007 and 2004 combined result is shown in Fig 5.43. Comparison with the theoretical expectation are discussed in Chapter 6.

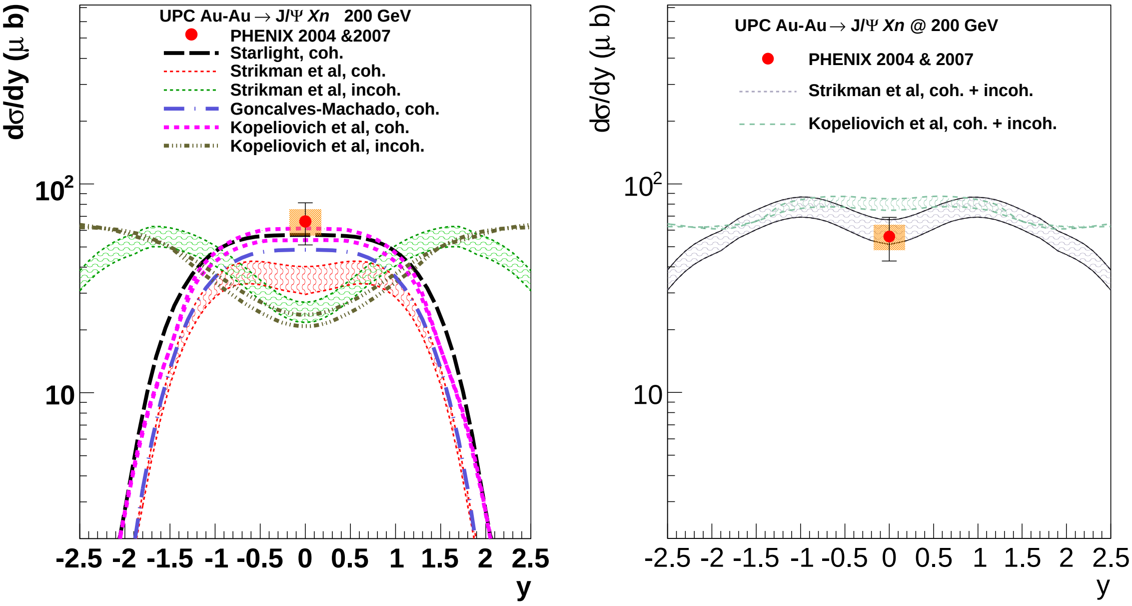

**Figure 5.43:** 2004 and 2007 combine cross-section compared to theoretical [40, 38, 41, 42, 42, 43].

### Cross section calculation with $+XnYn$ (double neutron tag)

The purpose of the section is to measure $d\sigma/dy$ of $J/\psi$ $+XnYn$ in the central rapidity.

Comparison with the double neutron tagged cross section in the forward rapidity will be discussed in the the next Chap. 6. There was just one additional cut "both side neutron tagging(both ZDC $>$ 30 GeV)".

**$dN/dm_{ee}$ and $dN/dp_T$ distribution** The $dN/dm_{ee}$ and $dN/dp_T$ distributions with $+XnYn$ condition are shown in Fig. 5.44. The $\sigma$ value is fixed to the value with $+Xn$ condition.

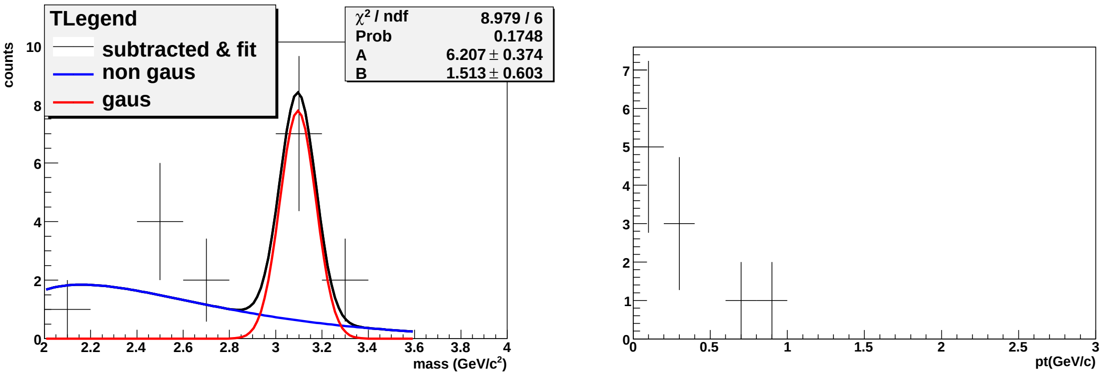

**Figure 5.44:** Left:The real data $dN/dm_{ee}$ plots with $+XnYn$ condition. The fitting function is shown as the black line. The blue line is continuum $e^+e^-$ part. The red line is $J/\psi$ part. Right:The $p_T$ distribution within $J/\psi$ 3 $\sigma$

The number of $J/\psi$ is $7.56 \pm 3.01$. Since there are too low statistics, the systematic error of number of $J/\psi$ can't be determined by same way. Therefore it is simply scaled with the single tagged result.

$$7.56 \times \frac{0.26}{16.2} = 0.12, \tag{5.19}$$

where 16.2 is number of $J/\psi$ $(+Xn)$ and 0.26 is its systematic error. Finally both side tagging UPC $J/\psi$ $\frac{d\sigma}{dy}$ at the central-rapidity is calculated by same procedure in Eq. 5.17, $21.0 \pm 7.9\,(\mathrm{stat}) \pm 2.7\,(\mathrm{sys})\ \mu\mathrm{b}$.

# Chapter 6

# Analysis of $J/\psi$ production at forward rapidity

## 6.1 Event reconstruction

### 6.1.1 The definition of PHENIX variables

Basic variables are as same as the central analysis case. Some muon specific variables are listed, below

1. $xposi, yposi(i = 1, 2, 3, 4)$:The x and y position. The 1 corresponds to the front of MuTR. The 2, 3, and 4 corresponds to the end of each station.
2. $DG0$:The distance from the projected road from MUID to the MuTR track at MuTR gap1 (cm).
3. $DDG0$:The angle between the projected road from MUID and the MuTR track at MuTR gap1 (degree).
4. $N_{muon}$:The number of reconstructed tracks in muon arms (It is not number of muons).
5. $Q_{rxnpn}$, $Q_{rxnps}$:The total charge of the north (south) side of RXNP (a.u.). Since the purpose of RXNP is to measure $\nu_2$, its absolute value isn't studied well. Anyway, this value will be used to check noise level or not.

### 6.1.2 The tracking algorithm

At first, the tracking algorithm of PHENIX muon arm will be described very briefly. The more detailed description is in Ref. [71]

**Load finding in MUID**

MUID has five gaps and each gap has horizontal and vertical direction wires and absorbers. Then each MUID gap has two dimensional hit information. Adjacent hit packs in the each gap of MuID are grouped into clusters. The maximum cluster size is two packs. Three or more packs are divided into two or more clusters.

For horizontal and vertical direction, one dimensional straight fits between each cluster pair of gap2 and gap3 are made. Then, clusters in gap1, gap4, and gap5 are searched for ± 60 cm window from the projection point for each road. If there were two or more candidate clusters in one gap, new roads are made as much as possible. Just one gap can be allowed to be skipped in the process.

Then, the two directions MUID roads are paired into a two dimensional road. In this process, the difference between the maximum gap of horizontal and vertical roads should be less than two gaps.

**Track finding in MuTR**

MuTR has three stations and each station has two or three gaps and each gap has two directions (not horizontal and vertical but cross together) wire sets. Each MuTR station can make two dimensional position information. The crossing point of two or more fired wires is called stub. All possible pairs between MuTR station 3 stubs and clusters of MUID gap1 are made. The pairs in the north (south) arm are checked matching with MUID roads within ±30 (50) cm. The algorithm selects each closest pair. Then, go to MuTR gap 2 and 1 to search the nearest stub.

There are nose cones between collision point and North and south muon arms and MUID has Fe shield to reduce hadron contamination.

Since the suppressor disturbs track information, then only information of MuTR is used to reconstruct momentum of the tracks. Therefore, as different from the analysis of the central arm case, the momentum resolution of Muon arm isn't affected by the change of main vertex detector.

### 6.1.3 The muon track selection

Following cuts were applied to muon candidate tracks [72]. For the North arm:

1. Reach gap 5 (max) of MUID
2. $DG0 < 15$ cm
3. $DDG0$ <10 degree
4. Track chi2 <10 cm
5. Number of MuID hits >=7 (N)
6. $|p_Z| > 2$ GeV/$c$
7. $1.2 < |\eta| < 2.2$
8. MUID2D trigger of the same arm is fired

For south arm:

1. Reach gap 5 (max) of MUID

2. $DG0 < 20$ cm

3. $DDG0$ <8 degree

4. Track chi2 <8 cm

5. Number of MuID hits >=8 (N)

6. $|p_Z| > 2$ GeV/$c$

7. $1.2 < |\eta| < 2.2$

8. MUID2D trigger of the same arm is fired

## 6.2 Vertex reconstruction

As different from central UPC trigger, forward UPC triggers require both side neutron tagging. The $z_{ZDC}$ is always available.

### 6.2.1 Neutron requirement

In this analysis, both ZDCs were required to detect neutrons in order to obtain the $Z_{ZDC}$ from their timing information. As shown in Sec. 5.7.5, the resolution of $Z_{ZDC}$ is about 3 cm. In mid-rapidity UPC analysis, Zvertex was calculated from track extrapolation. In muon arm analysis, due to the nose cone, track extrapolation ($Z - T = \sqrt{x^2 + y^2}$ plane projection ) was not accurate. The $z_{zdc}$ - $Z_{muon}$ (track extrapolated Zvertex) distribution and its fitting result with a Gaussian function in the sampled forward UPC trigger events is shown in Fig. 6.1. The $\sigma$value of 25 cm is quite larger than 3 cm, therefore $z_{vtx}$ measured with the muon arm isn't appropriate in the analysis.

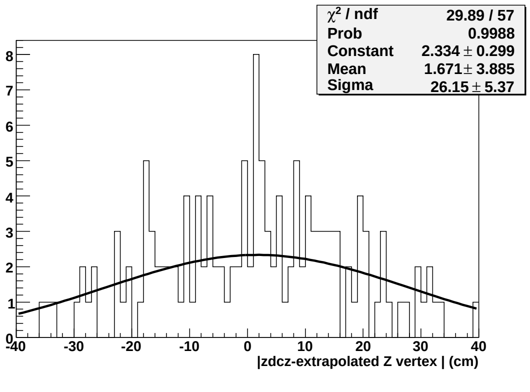

**Figure 6.1:** The distribution of the $z_{zdc}$ - track extrapolation Zvertex.

## 6.3 The fiducial cuts

The main source of dead map of muon arms is due to broken wires. In this analysis, dead map in the 2010 PHENIX run analysis were used [72]. Two run-by-run unstable big holes are found in the octant 4 and 8 of South arm. As shown in Fig. 6.2, their areas are removed from the analysis. In the south arm, $-0.8 < \phi < -0.55$ region of the octant 4 or 8 is killed by the fiducial cut from real and simulated data.

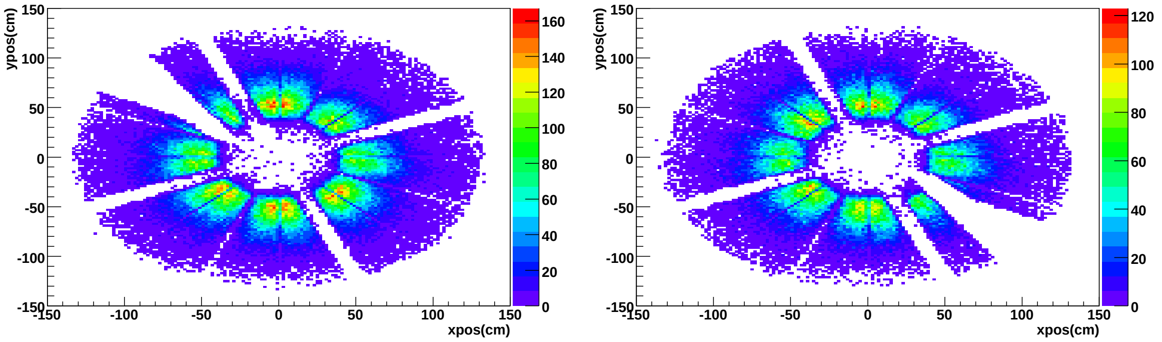

**Figure 6.2:** The distribution of $x$ and $y$ position of muon tracks in UPC real data files in the South arm. Left:when oct4 has a big hole. Right:oct8 has a big hole.

Additionally, some broken wires of MuTr are disabled in the simulation.

## 6.4 Event selection

Following selections are applied step-by-step in order to select UPC $J/\psi$ events.

- Good run selection:The criteria is described in the next section.
- Trigger selection:Events triggered with Forward-UPC triggers are selected.
- Muon finding:
- Offline reconfirmation of the triggered conditions.
  - $E_{ZDCN} > 30$ GeV & $E_{ZDCS} > 30$ GeV.
  - $(N_{BBCN} = 0 | N_{BBCS} = 0)$.
- Using usual vertex range:$|z_{zdc}| < 30$ cm.
- $Q_{rxnpn} < 1000$ and $Q_{rxnps} < 1000$
- $N_{track} = 0$

### 6.4.1 Good run selection

The good runs are selected with the following requirements which were commonly used in the other measurements.

1. The run lasted at least 15 minutes of data acquisition.
2. Online calibration was done for all detectors. (PHENIX detectors sometimes (day by day, week by week, etc.) need recalibration, and sometimes they were forgotten)
3. Only MB runs are accepted.
4. Runs with huge tripping in MuTR are rejected.

### 6.4.2 Event characteristic of triggered events with at least a $\mu$ pair

As was the case of the central UPC trigger, contamination of MB events is the main component of the UPC triggered events. The pair mass distributions of the all triggered data with the non-multiplicity cut, "$(|z_{zdc}|$ <30 cm& $(E_{ZDCN} >$ 30GeV & $E_{ZDCS} >$ 30 GeV & $(N_{BBCN}{=}0|N_{BBCS}{=}0)$" are shown in Fig 6.3.

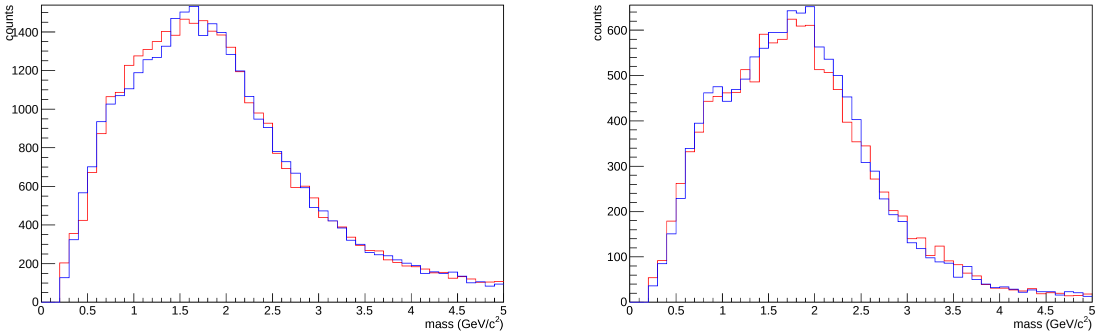

**Figure 6.3:** Left:The invariant-mass distributions of the $\mu^+\mu^-$ pairs with the non-multiplicity cut, "$|z_{zdc}|$ <30 cm& $(E_{ZDCN} >$ 30GeV & $E_{ZDCS} >$ 30 GeV & $(N_{BBCN}{=}0|N_{BBCS}{=}0)$" in North arm. Right:The invariant-mass distributions of the $\mu^+\mu^-$ pairs with the non-multiplicity cut, "$|z_{zdc}|$ <30 cm& $(E_{ZDCN} >$ 30GeV & $E_{ZDCS} >$ 30 GeV & $(N_{BBCN}{=}0|N_{BBCS}{=}0)$" in South arm.

The $N_{track}$ distributions where the events have at least one muon pair with mass from 2.7 to 3.5 GeV are shown in Fig 6.4.

Clear three peaks can be seen at the north. The first peak has only unlike-sign pairs, and the second and third peaks have the almost same amount of unlike and like-sign pairs. On the other hand, South arm has lower background components.

The corresponding distributions of $Q_{rxnp}$ are shown in Fig 6.5. Figure 6.6 is expanded view near 0. Both distributions have almost same amount of unlike and like-sign pairs and they don't have clear border line. On the other hand, unlike-sign dominant component and other components can be divided easily.

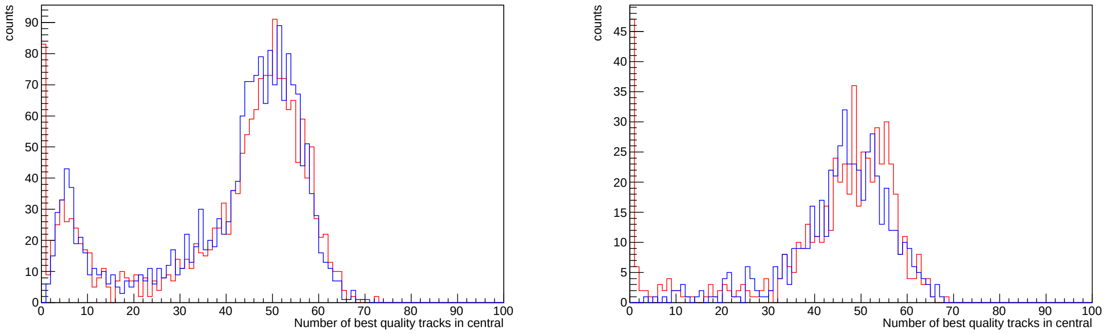

**Figure 6.4:** Left:The distributions of $N_{track}$ for $\mu$ pair in the North arm where the events have the pairs with mass from 2.7 to 3.5 GeV with the non-multiplicity cut. Right:The distributions of $N_{track}$ for $\mu$ pair in the South arm where the events have the pairs with mass from 2.7 to 3.5 GeV with the non-multiplicity cut. The red (blue) line corresponds to unlike (like) sign pair.

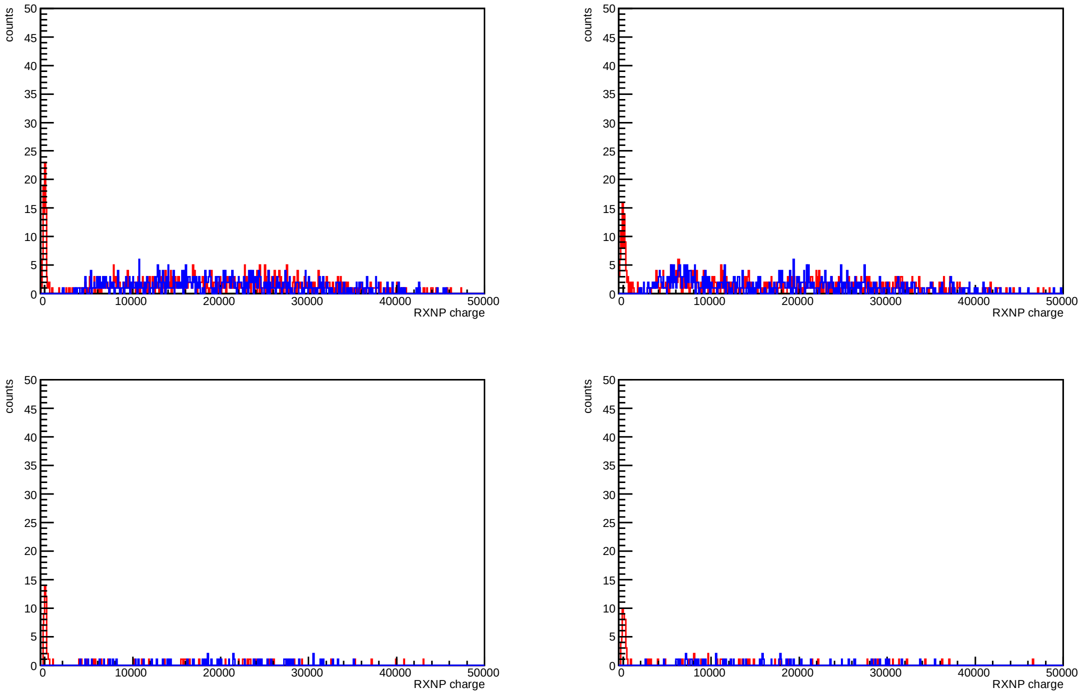

**Figure 6.5:** The distributions of RXNP charge with the cut of "$|z_{zdc}|$ <30 cm& ($E_{ZDCN}$ > 30GeV & $E_{ZDCS}$ > 30 GeV)& ($N_{BBCN}$=0$|N_{BBCS}$=0)&(2.7< $mass$ <3.5 GeV) ". Upper (Under) two figures correspond to when dimuon pair is detected by the north (south) arm. The charge of the north (south) RXNP is shown in Left (Right) panel.

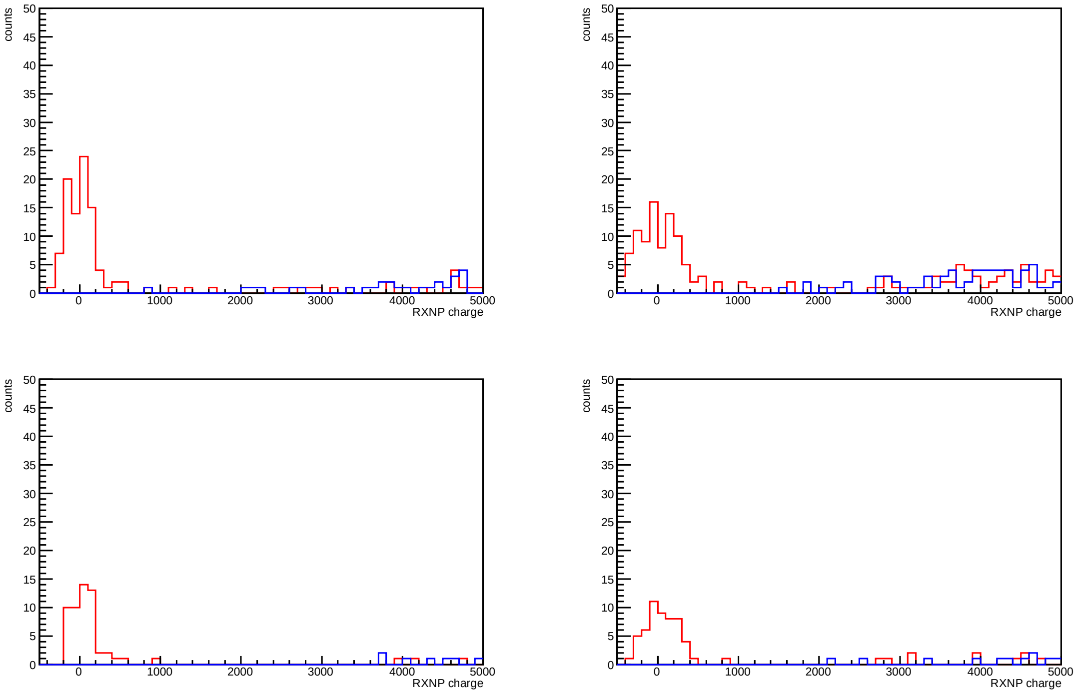

**Figure 6.6:** Same as Fig 6.5, with adifferent x-axis scale, in order to see.

The unexpected background process can be removed by the cut of ($Q_{rxnpn}$ <1000 & $Q_{rxnps}$¡1000)

The distributions of $N_{track}$s at 2.6∼3.6 GeV/$c^2$ with the cut of ”$|z_{zdc}|$ <30 cm& ($E_{ZDCN} >$ 30GeV & $E_{ZDCS} >$ 30 GeV )& ($N_{BBCN}$=0$|N_{BBCS}$=0)& ($Q_{rxnpn}$ <1000 & $Q_{rxnps}$¡1000)&(2.7< $mass$ <3.5 GeV)” are shown in Fig 6.7.

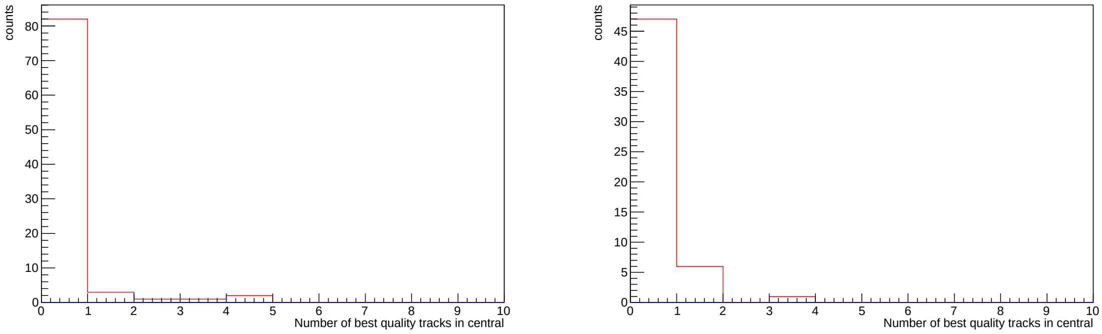

**Figure 6.7:** The distributions of $N_{track}$s at 2.6∼3.6 GeV/$c^2$ with the cut of ”$|z_{zdc}|$ <30 cm& ($E_{ZDCN} >$ 30GeV & $E_{ZDCS} >$ 30 GeV )& ($N_{BBCN}$=0$|N_{BBCS}$=0)& ($Q_{rxnpn}$ <1000 & $Q_{rxnps}$¡1000)&(2.7< $mass$ <3.5 GeV)”.

Clear peak at zero can be seen and there are some events with additional tracks. It suggests contamination from most peripheral.

## 6.5 The final sample

The conditions are summarized as ”$|z_{zdc}| <30$ cm& ($E_{ZDCN} > 30$GeV & $E_{ZDCS} > 30$ GeV )& ($N_{BBCN}=0|N_{BBCS}=0$)& ($Q_{rxnpn} <1000$& $Q_{rxnps} <1000$)”. Invariant-mass distributions of the $\mu^+\mu^-$ pairs and correspond $p_T$ distributions for the final samples are shown in Fig. 6.8 and 6.9.

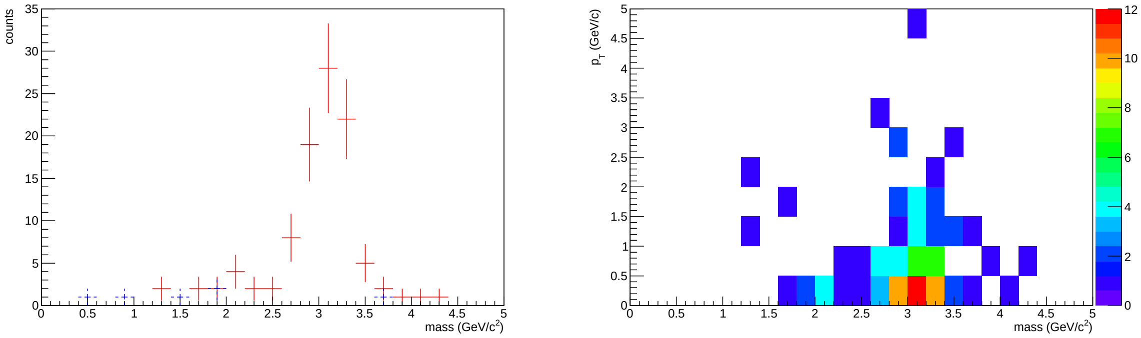

**Figure 6.8:** Left:The distributions of muon pair mass for the final sample in North arm. The red (blue) line corresponds to unlike (like) sign pair. Right: The correspond —PT distribution.

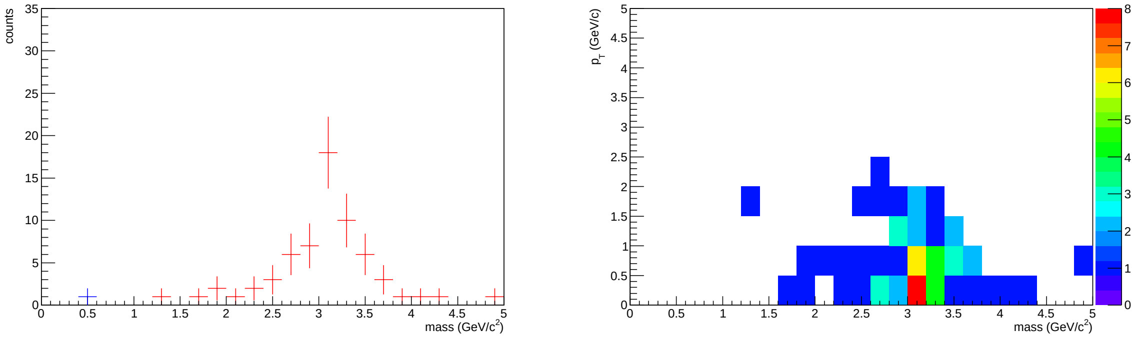

**Figure 6.9:** Left:The distributions of muon pair mass for the final sample in South arm. The red (blue) line corresponds to unlike (like) sign pair. Right: The correspond —PT distribution.

The distributions of ZDC energy deposit are shown in Fig 6.10. There is a clear correlation between the direction of $J/\psi$ and forward neutron multiplicity. The mean values of the ZDC energy distribution which is the same side of measured $J/\psi$ are significantly higher than another one which is the opposite side of measured $J/\psi$.

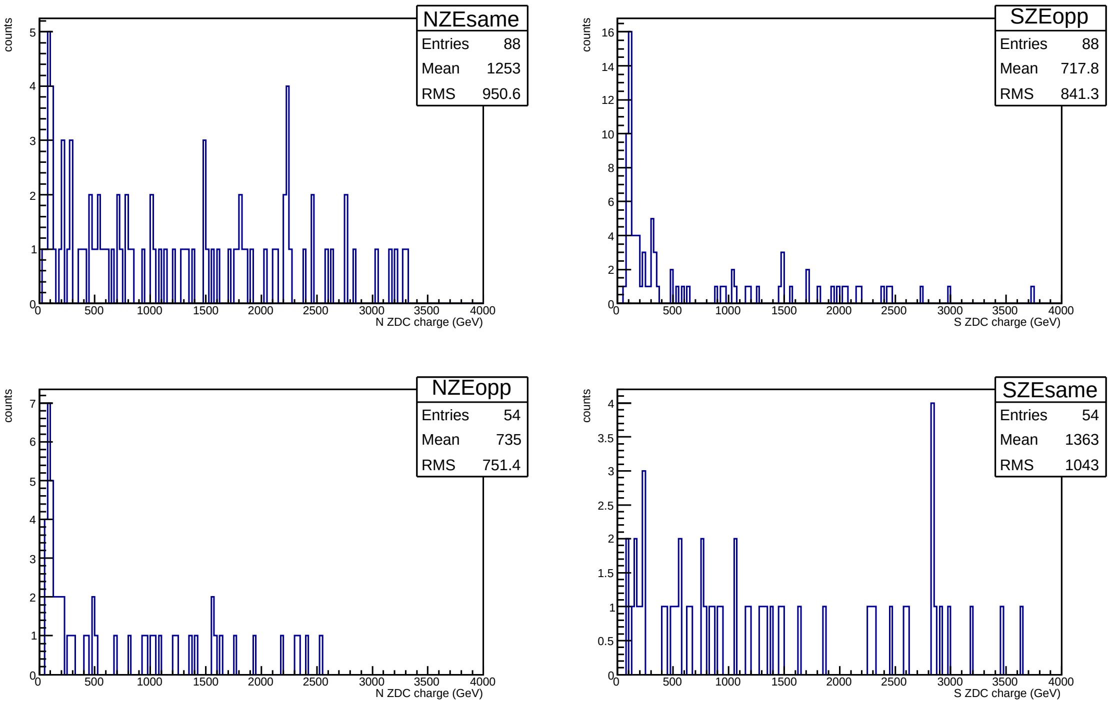

**Figure 6.10:** The ZDC energy deposit distributions of the final samples at 2.6 3.6 GeV/$c^2$ . Left (Right) two panels correspond to the north (south) ZDC. Upper (Lower)figures corresponds to when dimuon is detected by the north (south ) arms.

## 6.6 The background estimation

Considerable other main background sources for events with $M_{pair}$ 2∼4 GeV as follows.

1. $J/\psi$ production from most peripheral collisions.
2. Continuum UPC process, $\gamma\gamma \rightarrow \mu^+\mu^-$ .

### 6.6.1 The contamination from most peripheral collisions

The dimuon invariant mass yields of p+p collisions at $\sqrt{s}$= 200 GeV in the 2009 PHENIX run are shown in Fig. 6.11.

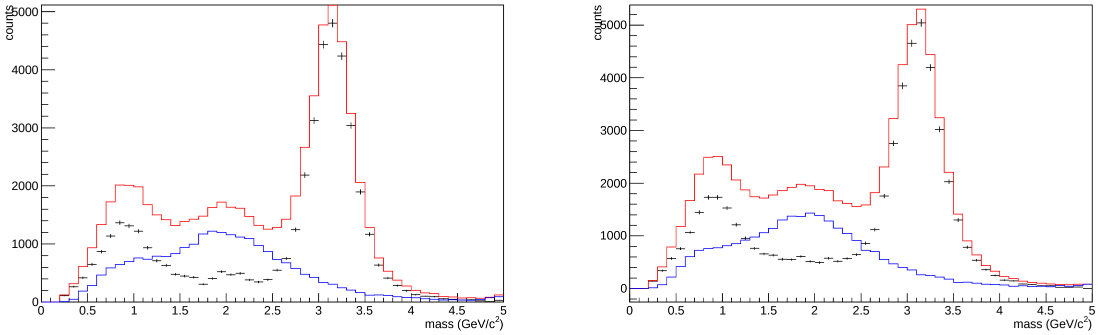

**Figure 6.11:** Left:The dimuon invariant mass yields of p+p collisions at $\sqrt{s}$= 200 GeV in 2009 year in the North arm. Right:The dimuon invariant mass yields of p+p collisions at $\sqrt{s}$= 200 GeV in 2009 year in the South arm. The red (blue) lines corresponds to unlike (like) sign pair.

To cancel the difference of the of $\mu^+$ and $\mu^-$, the amount of like-sign pairs is defined as the geometric mean of the statistics of $\mu^+\mu^+$ pairs and $\mu^-\mu^-$ pairs. The distributions of $N_{track}$s for $\mu^+\mu^-$ pairs where the events have pairs with mass from 2.6 to 3.6 GeV. GeV/$c^2$ are shown in Fig 6.12.

The dimuon invariant mass yields of p+p collisions at $\sqrt{s}$= 200 GeV in the 2009 PHENIX run with $N_{track}$=0 are shown in Fig. 6.13.

Following are shown in above figures:

1. In p+p, the ratio of unlike-sign to like-sign events in the continuum is about $\frac{3}{2}$.
2. The ratio wasn't changed with $N_{track}$=0.
3. 72 % of forward $J/\psi$ events have no central tracks.

There are seven $J/\psi$ candidate events with central tracks in the north (south) arm, therefore $7 \times 0.39 = 2.8$ contamination $J/\psi$ events under the full UPC selection are expected. The normalized invariant mass and its $p_T$ distribution to have 2.8 $J/\psi$ candidate events are shown in Fig 6.14 and Fig 6.15.

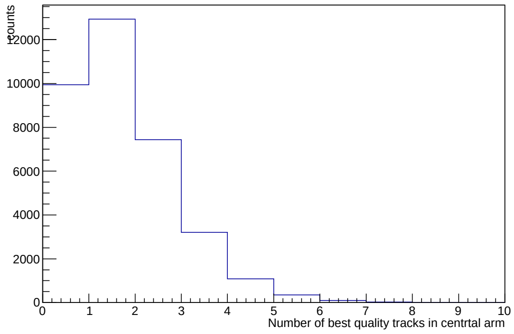

**Figure 6.12:** The distributions of $N_{track}$ for $\mu^+\mu^-$ pairs where the events have the pairs with mass from 2.6 to 3.6 GeV. p+p collisions at $\sqrt{s}$= 200 GeV in the 2009 PHENIX run.

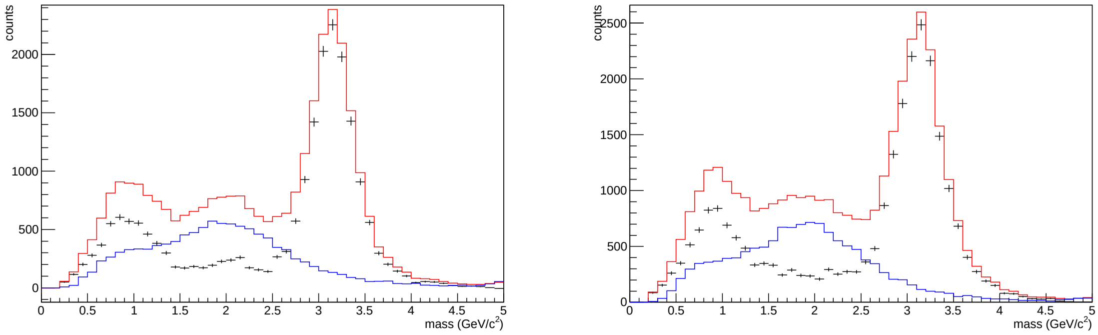

**Figure 6.13:** Left:The dimuon invariant mass yields of p+p collisions at $\sqrt{s}$= 200 GeV in the 2009 PHENIX run in the North arm with $N_{track}$=0. Right:The dimuon invariant mass yields of p+p collisions at $\sqrt{s}$= 200 GeV in the 2009 PHENIX run in the South arm with $N_{track}$=0. The red (blue) line corresponds to unlike (like) sign pair.

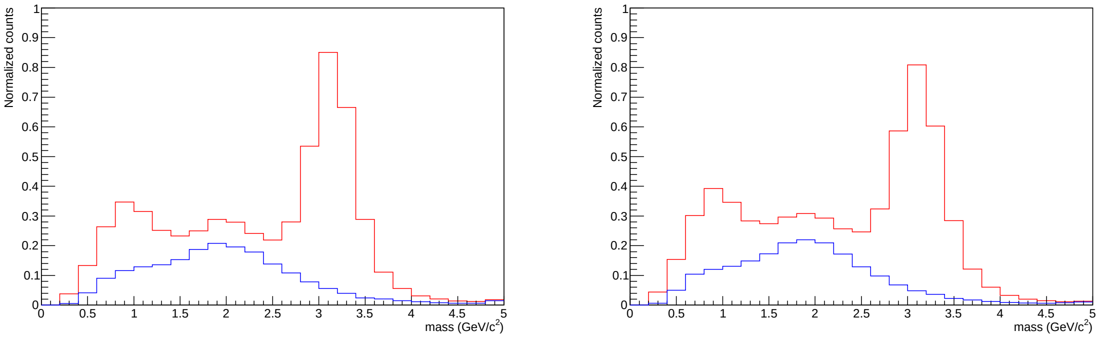

**Figure 6.14:** Left:The normalized distributions of mass for $\mu^+\mu^-$ pair where the events have the pairs with mass from 2.6 to 3.6 GeV in p+p collisions at $\sqrt{s}$= 200 GeV in the 2009 PHENIX run in the North arm to have 2.8 $J/\psi$ events. Right:The normalized distributions of mass for $\mu^+\mu^-$ pair where the events have the pairs with mass from 2.6 to 3.6 GeV in p+p collisions at $\sqrt{s}$= 200 GeV in the 2009 PHENIX run in the South arm to have 2.8 $J/\psi$ events. The red (blue) line corresponds to unlike (like) sign pair. The left (right) side corresponds to the north (south).

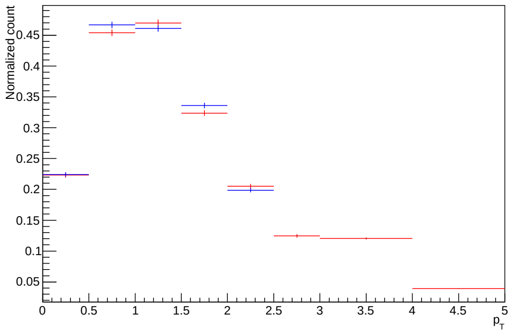

**Figure 6.15:** Normalized $p_T$ distribution where the events have the pair with mass from 2.6 to 3.6 GeV/$c^2$ in p+p collisions at $\sqrt{s}$= 200 GeV in the 2009 PHENIX run.

### 6.6.2 $\gamma\gamma \rightarrow \mu^+\mu^-$

The simulated invariant mass and rapidity distribution where the events have the pairs with mass from 2.0 to 4.0 GeV and $5 > |y|$ of $\gamma\gamma \rightarrow \mu^+\mu^-$ pairs using STARLIGHT model are shown in Fig 6.16.

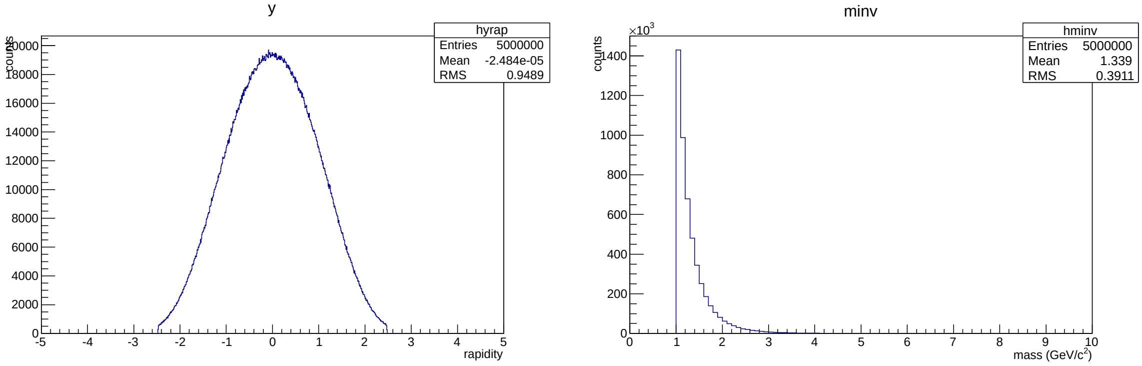

**Figure 6.16:** Left:The generated rapidity distribution of $\gamma\gamma \rightarrow \mu^+\mu^-$ where the events have the pairs with mass from 2.0 to 4.0 GeV and $5 > |y|$ using STARLIGHT model. Right :That of invariant mass.

The total cross section of $\gamma\gamma \rightarrow \mu^+\mu^-$ where the events have the pairs with mass from 2.0 to 4.0 GeV and $5 > |y|$ is 124 $\mu b$ [40]. If the ratio of no neutron tagging to $XnYn$ is assumed as same as that of coherent $J/\psi$, effective total cross section is 15.4 $\mu b$. The measured $\frac{d\sigma}{dy}$ of the muon arms is 20∼ 30 $\mu b$. The $\gamma\gamma$ process looks that it can be dominant back ground sources. However, the acceptance × efficiency of the PHENIX muon arms at lower mass and the edge of the detector ($|y| \simeq$1.2) are lower than that of $J/\psi$ . The detector passed invariant mass and $p_T$ distributions are shown in Fig. 6.17 and Fig. 6.18. Their contribution can be negligible.

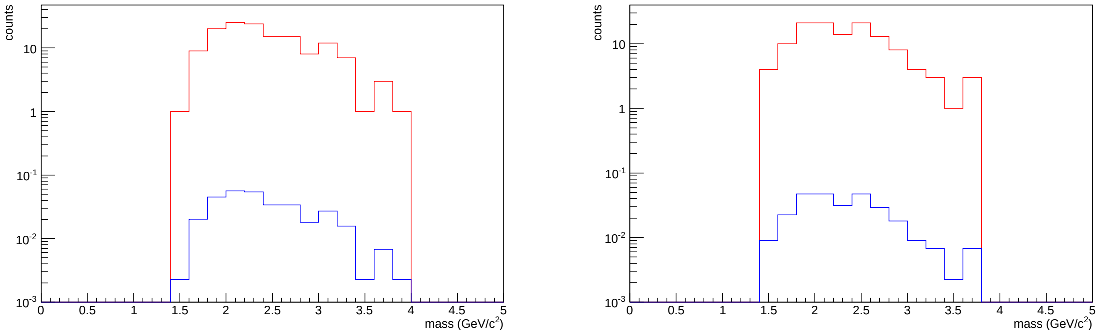

**Figure 6.17:** Left:The simulated distribution of detector passed invariant mass in the North arm. Right:The simulated distribution of detector passed invariant mass in the South arm. The red lines show all generated and the blue line is normalized to luminosity in the 2010 PHENIX run.

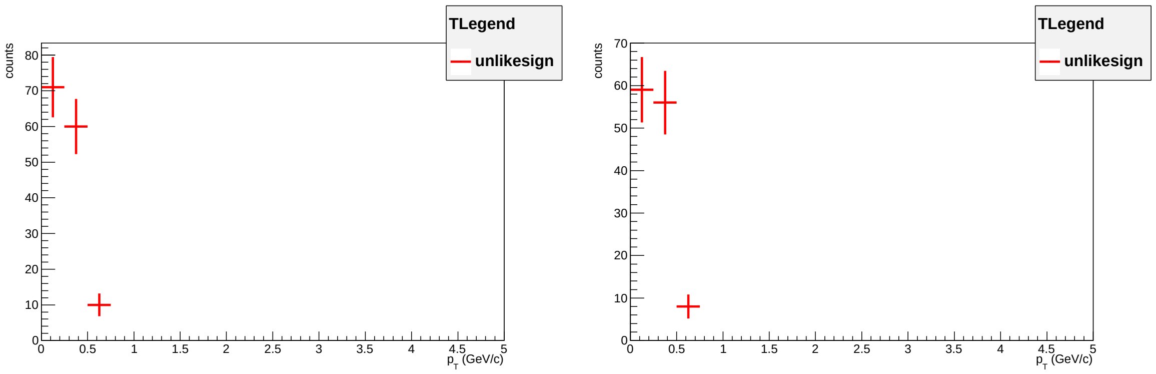

**Figure 6.18:** Left:The simulated distribution of detector passed $p_T$ in the North arm. Right:The simulated distribution of detector passed $p_T$ in the South arm.

Additionally, $p_T$ resolution of PHENIX muon arms around $J/\psi$ mass is typically 200 MeV/c. The generated $p_T$ distribution of $\gamma\gamma \rightarrow \mu^+\mu^-$ pairs using STARLIGHT model is nearly equal to clear narrow peak at 0 GeV/$c$ . Even in Fig. 6.18, tail of few events reach at the region of $p_T >$ 0.5 GeV/c, the $p_T$ bin size of 0.5 GeV/$c$ for the real data is acceptable.

### 6.6.3 Fitting (Over all continuum background)

At $\sim$ 2.0 GeV/$c^2$ , the sum of the expected yield of $\gamma\gamma$ and the yield of most peripheral contamination per bin is lower than one event. On the other hand, several events with low $M_{\mu\mu}$ pairs are observed in the final sample. Therefore, some other continuum process is suggested, for example $\gamma Au \rightarrow c\bar{c} \rightarrow \mu^+\mu^-$ , $\gamma Au \rightarrow \pi^+\pi^- \rightarrow \mu^+\mu^- + X$, and others. Unfortunately, there are too low statistics to discuss more detail.

Finally, following fitting function is used;

$$Acc_{supp}(m) \times \left[ p_0 \frac{1-p_4}{\sqrt{2\pi}p_2} e^{\frac{-(m-p_1)^2}{2p_2^2}} + p_0 p_4 \frac{1}{\sqrt{2\pi}p_3} e^{\frac{-(m-p_1)^2}{2p_3^2}} + p_5 exp(m/p_6) \right] \tag{6.1}$$

where $Acc_{sup}$ is mass dependence of the dimuon geometric acceptance, defined in each $p_T$ ranges, two Gaussian functions correspond to $J/\psi$ and tail of $J/\psi$ respectably, $p_0$ is the yield of $J/\psi$, $p_1$ and $p_2$ are mean value and $\sigma$ of Gaussian function of $J/\psi$, $p_3$ is the $\sigma$ of the Gaussian of function of the tail of $J/\psi$, $p_4$ is the ratio of the Gaussian of function of the tail of $J/\psi$, and $p_5$ and $p_6$ are the parameters of the exponential. Obviously, there are too many free parameters for the too low statistics of the final samples. Therefore, following procedure was taken to get fitting function for the real event of UPC.

1. $Acc_{sup}$ depends on $p_T$, then divide final sample into some $p_T$ ranges.

2. The invariant mass distribution of correspond $p_T$ range of p+p collisions at $\sqrt{s}$= 200 GeV is fitted with the function.

3. Different from the analysis of the central-rapidity(+Xn) , in this measurement, the $z_{vtx}$ information is always available and only MuTR is used in momentum reconstruction, the resolution of $p_T$ will not change from normal p+p collisions. Therefore, the mean values and $\sigma$ values can be fixed to p+p values.

4. Fix the slope of exponential value to that of p+p case. It corresponds to assume $\gamma Au \to c\bar{c}$ is dominant process, or mass dependency is independent of its process.

5. There are just two parameters, they correspond to yield of $J/\psi$ and background. The fitting function can be used for the final samples.

The fitted invariant mass distributions of p+p collisions at $\sqrt{s}$= 200 GeV and corresponding results are shown in Fig. 6.19 $\sim$ 6.31.

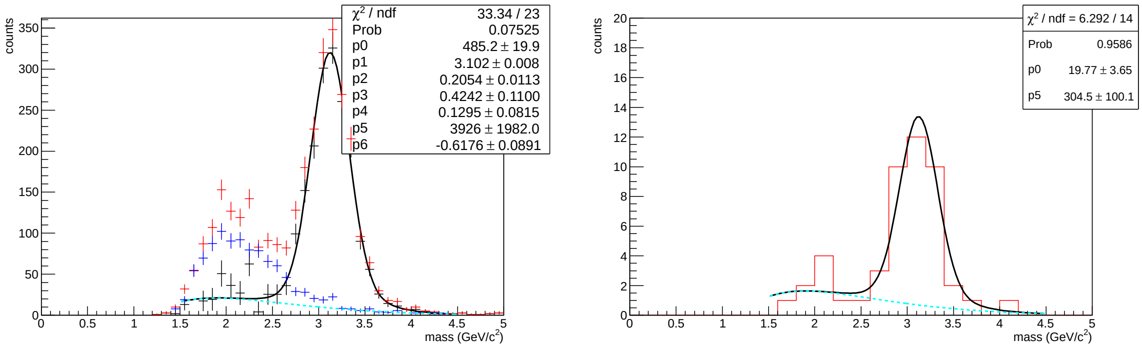

**Figure 6.19:** Left:The fitted invariant mass distribution and fitting result in the North arm of p+p collisions at $\sqrt{s}$= 200 GeV, $p_T$ <0.5 GeV/$c$ . Right:The fitting result in the North arm of UPC at $\sqrt{s}$= 200 GeV, $p_T$ <0.5 GeV/$c$ . The red (blue) crosses correspond to unlike (like) sign pair and the black crosses correspond to subtracted. The black line corresponds to the fitting result, light blue line corresponds to continuum background

Finally, number of $J/\psi$ in each $p_T$ region were calculated as follows;

$$N_{J/\psi} = \int Acc_{supp}(m) \times \left[ p_0 \frac{1-p_4}{\sqrt{2\pi}p_2} e^{\frac{-(m-p_1)^2}{2p_2^2}} + p_0 p_4 \frac{1}{\sqrt{2\pi}p_3} e^{\frac{-(m-p_1)^2}{2p_3^2}} \right]. \tag{6.2}$$

Its statistical errors were estimated as follows;

$$N_{J/\psi} \times \frac{err_{p_0}}{p_0}, \tag{6.3}$$

where $err_{p_0}$ is fitting error of $p_0$. Additionally, the systematic error of this fitting method is estimated as the sqrt of integrated value of the continuum component at 2.6$\sim$ 3.6 GeV. The results are summarized in Tab. 6.1.

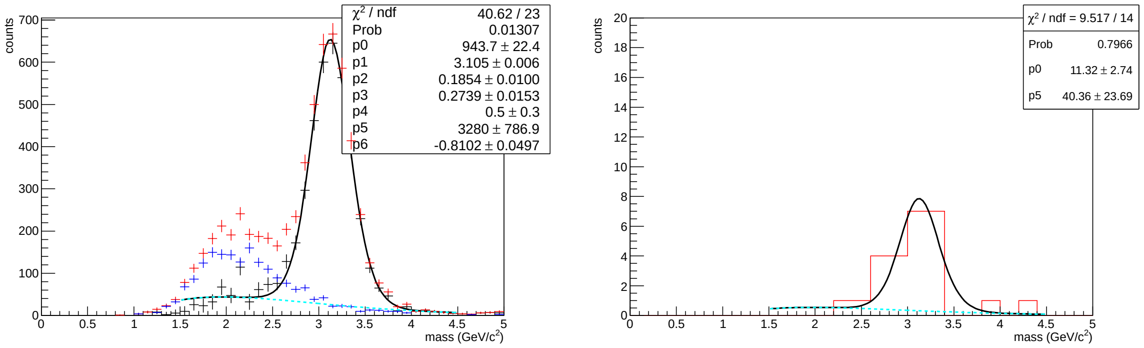

**Figure 6.20:** Left:The fitted invariant mass distribution and fitting result in the North arm of p+p collisions at $\sqrt{s}$= 200 GeV, 0.5 < $p_T$ <1.0 GeV/$c$ . Right:The fitting result in the North arm of UPC at $\sqrt{s}$= 200 GeV, 0.5 < $p_T$ <1.0 GeV/$c$ . The red (blue) crosses correspond to unlike (like) sign pair and the black crosses correspond to subtracted. The black line corresponds to the fitting result, light blue line corresponds to continuum background

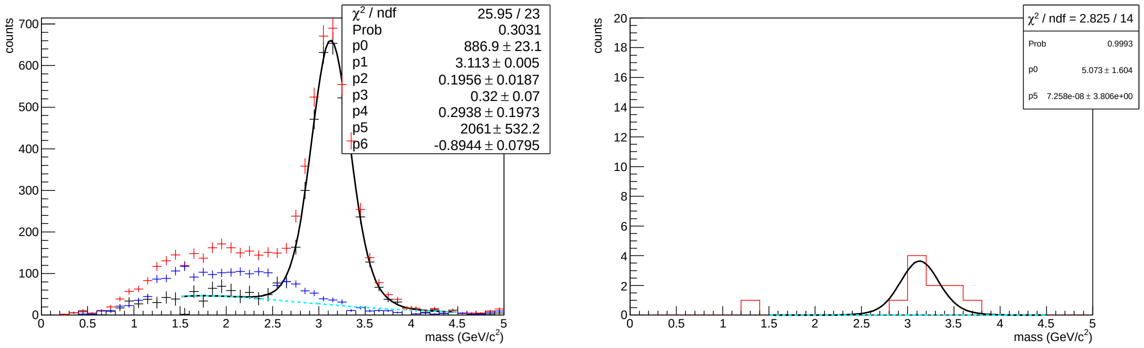

**Figure 6.21:** Left:The fitted invariant mass distribution and fitting result in the North arm of p+p collisions at $\sqrt{s}$= 200 GeV, 1.0<$p_T$ <1.5 GeV/$c$ . Right:The fitting result in the North arm of UPC at $\sqrt{s}$= 200 GeV, 1.0<$p_T$ <1.5 GeV/$c$ . The red (blue) crosses correspond to unlike (like) sign pair and the black crosses correspond to subtracted. The black line corresponds to the fitting result, light blue line corresponds to continuum background

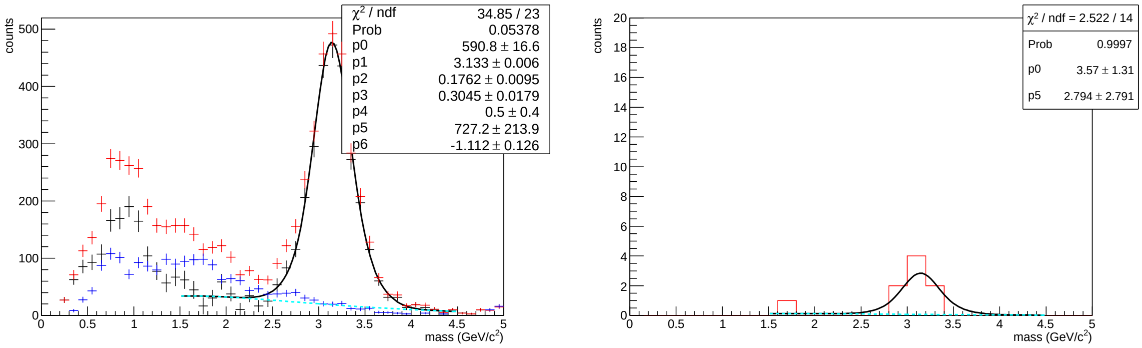

**Figure 6.22:** Left:The fitted invariant mass distribution and fitting result in the North arm of p+p collisions at $\sqrt{s}$= 200 GeV, 1.5 $<$ $p_T$ $<$2.0 GeV/$c$ . Right:The fitting result in the North arm of UPC at $\sqrt{s}$= 200 GeV, 1.5 $<$ $p_T$ $<$2.0 GeV/$c$ . The red (blue) crosses correspond to unlike (like) sign pair and the black crosses correspond to subtracted. The black line corresponds to the fitting result, light blue line corresponds to continuum background

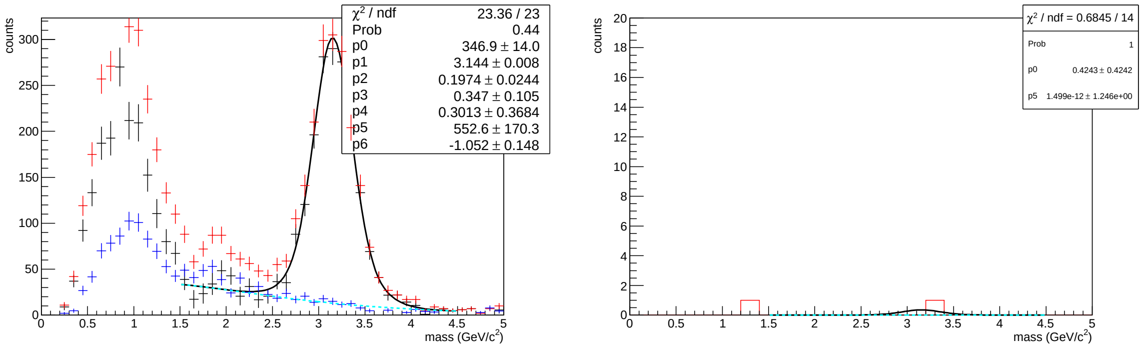

**Figure 6.23:** Left:The fitted invariant mass distribution and fitting result in the North arm of p+p collisions at $\sqrt{s}$= 200 GeV, 2.0$<$$p_T$ $<$2.5 GeV/$c$ . Right:The fitting result in the North arm of UPC at $\sqrt{s}$= 200 GeV, 2.0$<$$p_T$ $<$2.5 GeV/$c$ . The red (blue) crosses correspond to unlike (like) sign pair and the black crosses correspond to subtracted. The black line corresponds to the fitting result, light blue line corresponds to continuum background

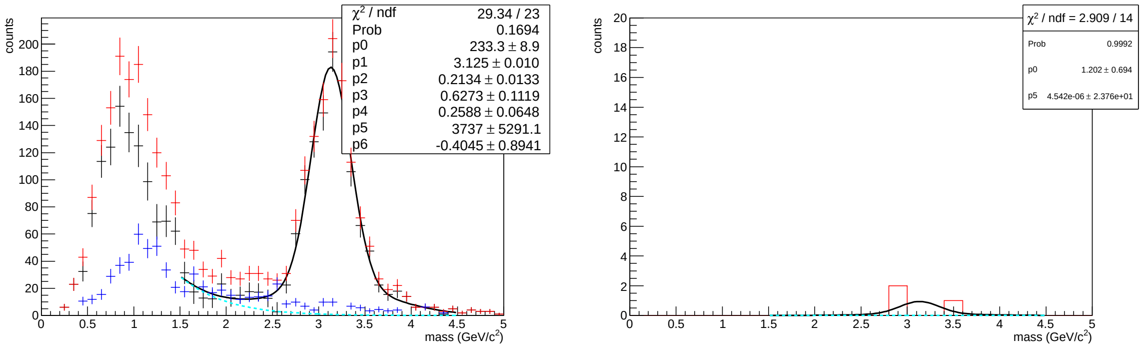

**Figure 6.24:** Left:The fitted invariant mass distribution and fitting result in the North arm of p+p collisions at $\sqrt{s}$= 200 GeV, 2.5 $<p_T<$3.0 GeV/$c$ . Right:The fitting result in the North arm of UPC at $\sqrt{s}$= 200 GeV, 2.5 $<p_T<$3.0 GeV/$c$ . The red (blue) crosses correspond to unlike (like) sign pair and the black crosses correspond to subtracted. The black line corresponds to the fitting result, light blue line corresponds to continuum background

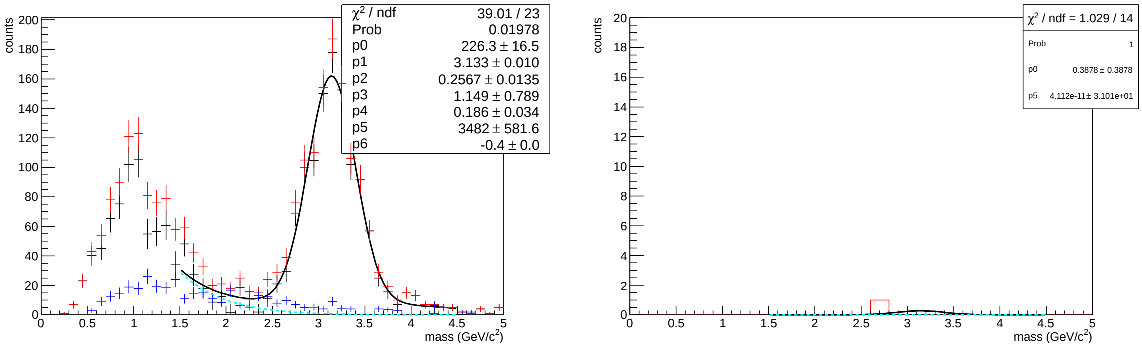

**Figure 6.25:** Left:The fitted invariant mass distribution and fitting result in the North arm of p+p collisions at $\sqrt{s}$= 200 GeV, 3.0 $<p_T<$4.0 GeV/$c$ . Right:The fitting result in the North arm of UPC at $\sqrt{s}$= 200 GeV, 3.0 $<p_T<$4.0 GeV/$c$ . The red (blue) crosses correspond to unlike (like) sign pair and the black crosses correspond to subtracted. The black line corresponds to the fitting result, light blue line corresponds to continuum background

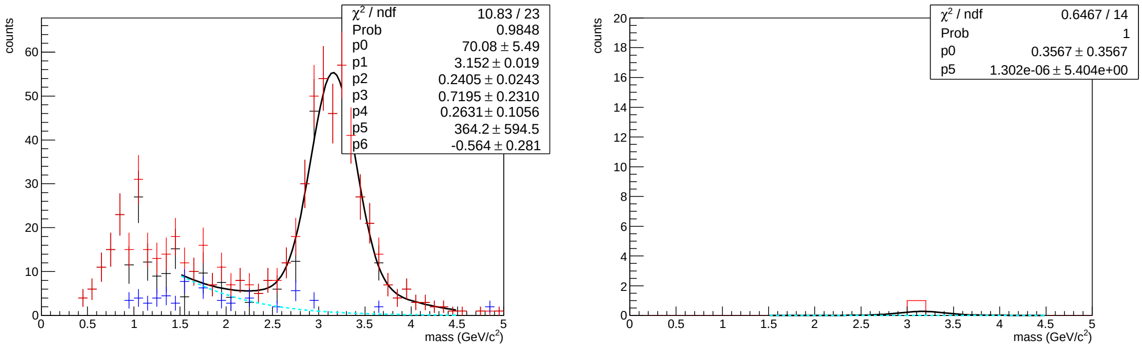

**Figure 6.26:** Left:The fitted invariant mass distribution and fitting result in the North arm of p+p collisions at $\sqrt{s}$= 200 GeV, 4.0 < $p_T$ <5.0 GeV/$c$ . Right:The fitting result in the North arm of UPC at $\sqrt{s}$= 200 GeV, 4.0 < $p_T$ <5.0 GeV/$c$ . The red (blue) crosses correspond to unlike (like) sign pair and the black crosses correspond to subtracted. The black line corresponds to the fitting result, light blue line corresponds to continuum background

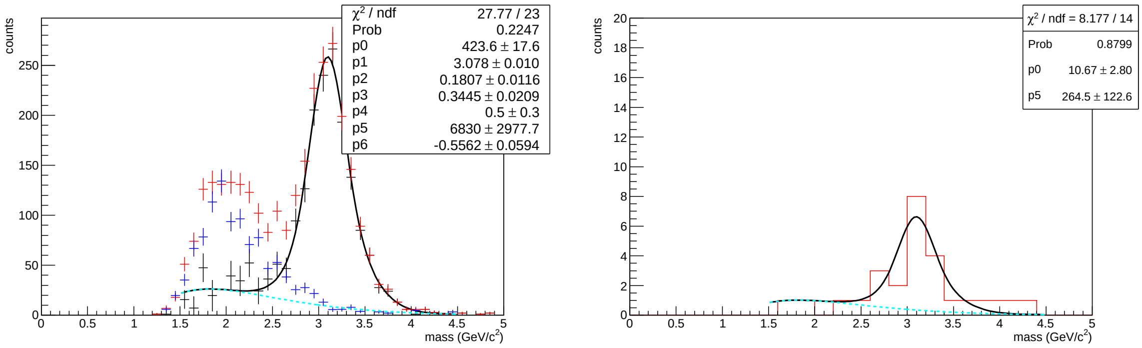

**Figure 6.27:** Left:The fitted invariant mass distribution and fitting result in the South arm of p+p collisions at $\sqrt{s}$= 200 GeV, $p_T$ <0.5 GeV/$c$ . Right:The fitting result in the South arm of UPC at $\sqrt{s}$= 200 GeV, $p_T$ <0.5 GeV/$c$ . The red (blue) crosses correspond to unlike (like) sign pair and the black crosses correspond to subtracted. The black line corresponds to the fitting result, light blue line corresponds to continuum background

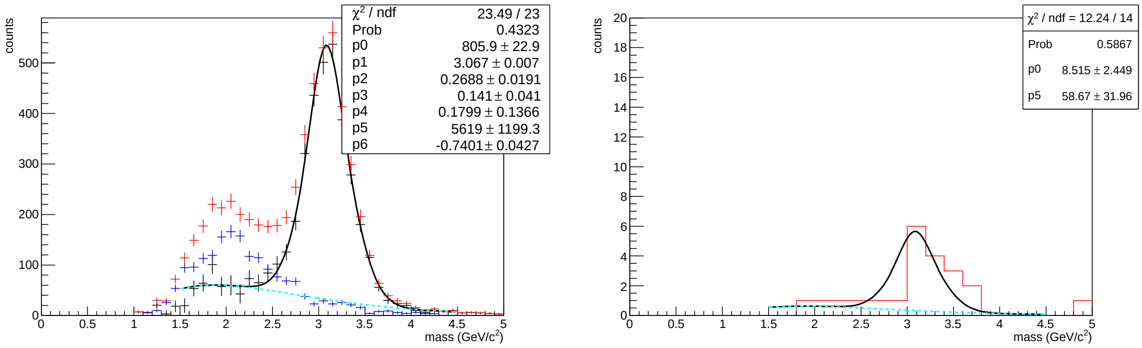

**Figure 6.28:** Left:The fitted invariant mass distribution and fitting result in the South arm of p+p collisions at $\sqrt{s}$= 200 GeV, 0.5 < $p_T$ <1.0 GeV/$c$ . Right:The fitting result in the South arm of UPC at $\sqrt{s}$= 200 GeV, 0.5 < $p_T$ <1.0 GeV/$c$ . The red (blue) crosses correspond to unlike (like) sign pair and the black crosses correspond to subtracted. The black line corresponds to the fitting result, light blue line corresponds to continuum background

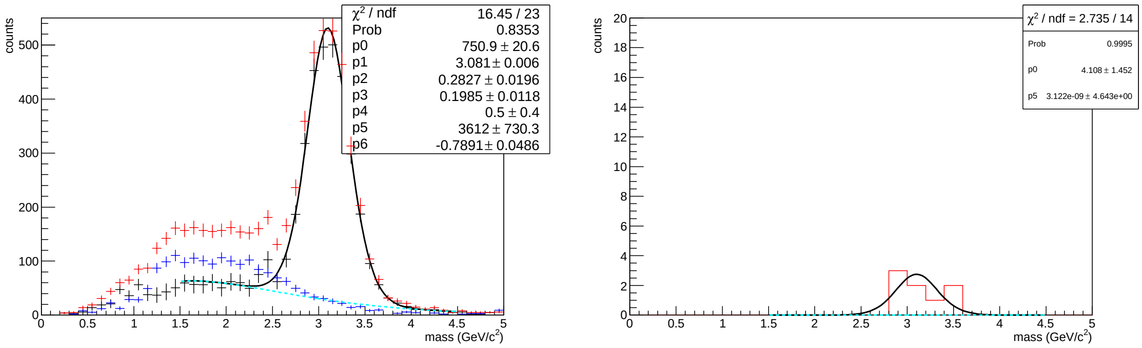

**Figure 6.29:** Left:The fitted invariant mass distribution and fitting result in the South arm of p+p collisions at $\sqrt{s}$= 200 GeV, 1.0<$p_T$ <1.5 GeV/$c$ . Right:The fitting result in the South arm of UPC at $\sqrt{s}$= 200 GeV, 1.0<$p_T$ <1.5 GeV/$c$ . The red (blue) crosses correspond to unlike (like) sign pair and the black crosses correspond to subtracted. The black line corresponds to the fitting result, light blue line corresponds to continuum background

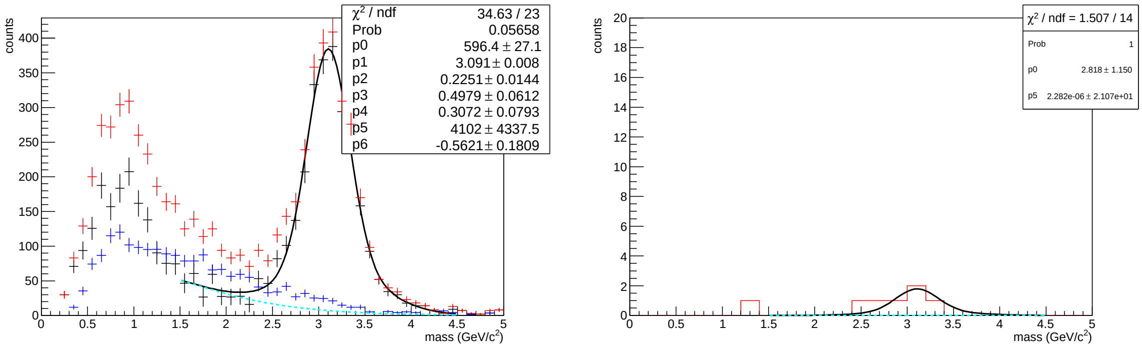

**Figure 6.30:** Left:The fitted invariant mass distribution and fitting result in the South arm of p+p collisions at $\sqrt{s}$= 200 GeV, 1.5 $<$ $p_T$ $<$2.0 GeV/$c$ . Right:The fitting result in the South arm of UPC at $\sqrt{s}$= 200 GeV, 1.5 $<$ $p_T$ $<$2.0 GeV/$c$ . The red (blue) crosses correspond to unlike (like) sign pair and the black crosses correspond to subtracted. The black line corresponds to the fitting result, light blue line corresponds to continuum background

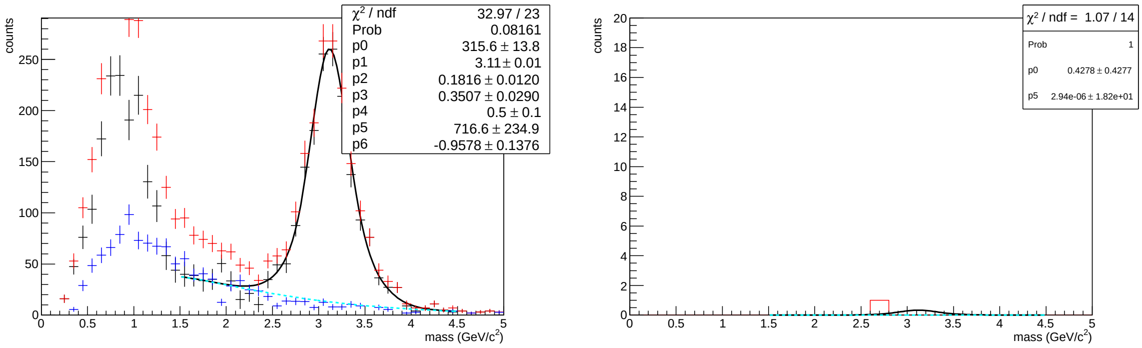

**Figure 6.31:** Left:The fitted invariant mass distribution and fitting result in the South arm of p+p collisions at $\sqrt{s}$= 200 GeV, 2.0$<$$p_T$ $<$2.5 GeV/$c$ . Right:The fitting result in the South arm of UPC at $\sqrt{s}$= 200 GeV, 2.0$<$$p_T$ $<$2.5 GeV/$c$ . The red (blue) crosses correspond to unlike (like) sign pair and the black crosses correspond to subtracted. The black line corresponds to the fitting result, light blue line corresponds to continuum background

| $p_T$ (GeV/$c$ ) | counts | Statistical error | Systematic error |
|---|---|---|---|
| North 0∼0.5 | 34.6 | 5.9 | 1.9 |
| North 0.5∼1.0 | 20.7 | 4.5 | 1.3 |
| North 1.0∼1.5 | 10.0 | 3.2 | -(too low) |
| North 1.5∼2.0 | 9.0 | 3.0 | - |
| North 2.0∼2.5 | 1.0 | 1.0 | - |
| North 2.5∼3.0 | 3 0 | 1.7 | - |
| North 3.0∼4.0 | 2.0 | 1.4 | - |
| North 4.0∼5.0 | 1.0 | 1.0 | - |
| South 0∼0.5 | 18.4 | 4.2 | 1.3 |
| South 0.5∼1.0 | 15.3 | 3.9 | 1.3 |
| South 1.0∼1.5 | 8.0 | 2.8 | -(too low) |
| South 1.5∼2.0 | 5.0 | 2.2 | - |
| South 2.0∼2.5 | 1.0 | 1.0 | - |

**Table 6.1:** The number of correspond events.

## 6.7 The correction factors

### 6.7.1 Luminosity $L_{int}$

The PHENIX north and south muon arms share a collision point. However, the runs with 10 or more tripped HV wires in an arm are excluded from the analysis. Then, integrated luminosity for the north and south arm are not same. The integrated luminosity for the north is 656.9±25.6 $\mu$/b, for the south luminosity is 628.3±25.0 $\mu$/b

### 6.7.2 Efficiency of the muon UPC trigger ($\epsilon_{trigger}$) in the 2010 PHENIX run

$\epsilon_{ZDC}$

As same as central arm analysis, $\epsilon_{ZDC}$ is constant and 1.

$\epsilon_{VETOBBC}$

As same as, central-rapidity analysis, the $\epsilon_{VETOBBC}$ is estimated from Tab 6.2.

$$\varepsilon_{BBCVETO} = 1 - \frac{35}{35+76} \times \frac{32}{32+76} = 0.90 \pm 0.043 \tag{6.4}$$

| * | $N_{BBCN}$==0 | $N_{BBCN}$!=0 |
|---|---|---|
| $N_{BBCS}$==0 | 76 | 35 |
| $N_{BBCS}$!=0 | 32 | killed |

**Table 6.2:** The number of correspond events.

$\epsilon_{MUID2D}$

From the definition of MUID2D at least a muon candidate pair reaches the gap3. The $\epsilon_{MUID2D}$ should have the $p_T$ dependence. However, in this analysis, the stronger condition to reach MUID gap5 is required for muon identification. Additionally, the efficiency of muon identification and its $p_T$ dependence is calculated in Sec 6.8.5. Then this term is ignored.

## 6.8 Trigger and detector efficiency calculation($(Acc \cdot \epsilon_{reco} \cdot \epsilon_{cuts})$)

The goal of this section is to get the (rapidity integrated) $p_T$ dependence and the ($p_T$ integrated) rapidity dependence of $(Acc \cdot \epsilon_{reco} \cdot \epsilon_{cuts}))$.

### 6.8.1 Basic information

As same as the analysis of central-rapidity, $(Acc \cdot \epsilon_{reco} \cdot \epsilon_{cuts})$ is calculated from $J/\psi$ simulation with the following condition. Then

1. Unpolarized and transversely polarized $J/\psi$ particles are generated in Monte Carlo with a flat distribution in $\psi$, $|\eta|$ and $p_T$ space in the regions [0,2$\pi$], [1.2,2.2] and [0,6.0], respectively.
2. They are fed to the detector simulation, the reconstruction program and offline cuts. In total there are 3000k events.
3. The events are weighted on $p_T$ and rapidity to make realistic $p_T$ and rapidity distribution and used for calculation of the detector acceptance, $(Acc \cdot \epsilon_{reco} \cdot \epsilon_{cuts})$. The details are described following subsection.
4. Different from the central arm $J/\psi$ $p_T$ distribution, the coherent peak is not so clear, then both unpolarized and transversely polarized data are used. Their average value is taken as the central value and the difference is taken as a systematic uncertainty.

### 6.8.2 Scatter distribution of *xpos* and *ypos*

Figure 6.32, 6.33, 6.34, and 6.35 show scatter distributions of *xpos* and *ypos* in the north or south arm, for each gap.

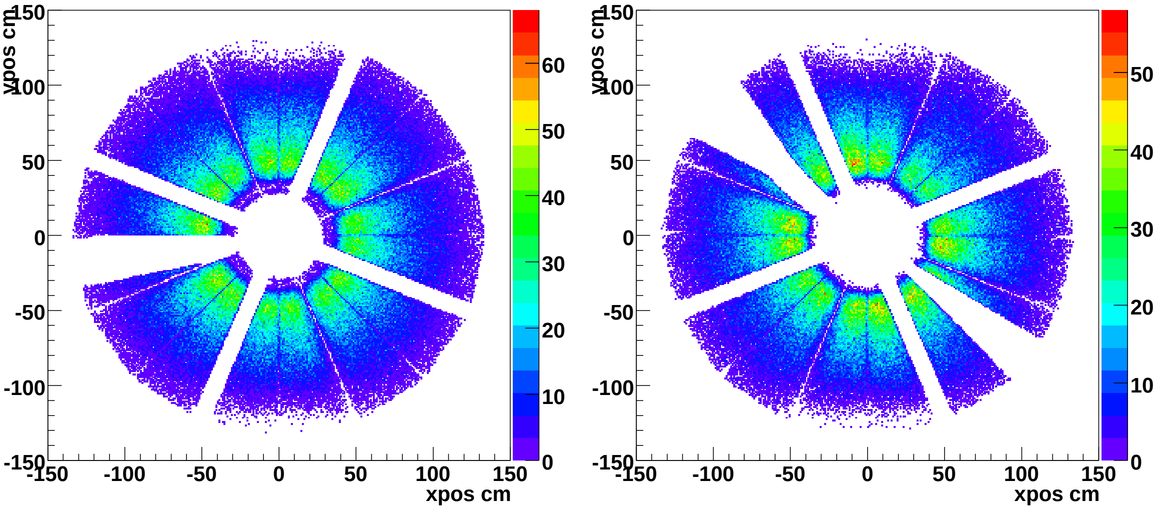

**Figure 6.32:** Left:Scatter distribution $xpos1$ and $ypos1$ of simulated muon tracks in the North arm. Right:Same one in the South arm.

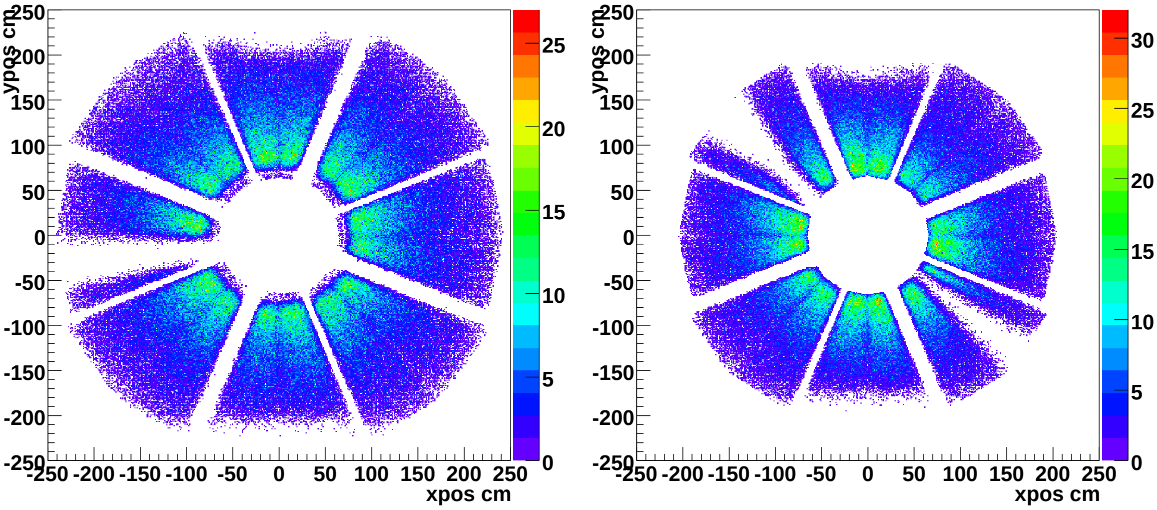

**Figure 6.33:** Left:Scatter distribution $xpos2$ and $ypos2$ of simulated muon tracks in the North arm. Right:Same one in the South arm.

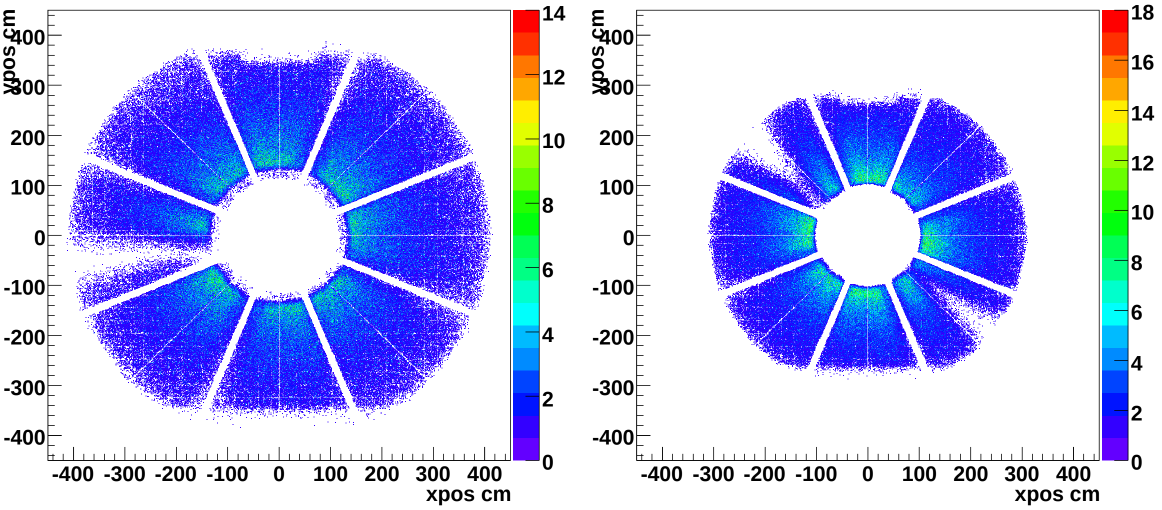

**Figure 6.34:** Left:Scatter distribution $xpos3$ and $ypos3$ of simulated muon tracks in North arm. Right:Same one in the South arm.

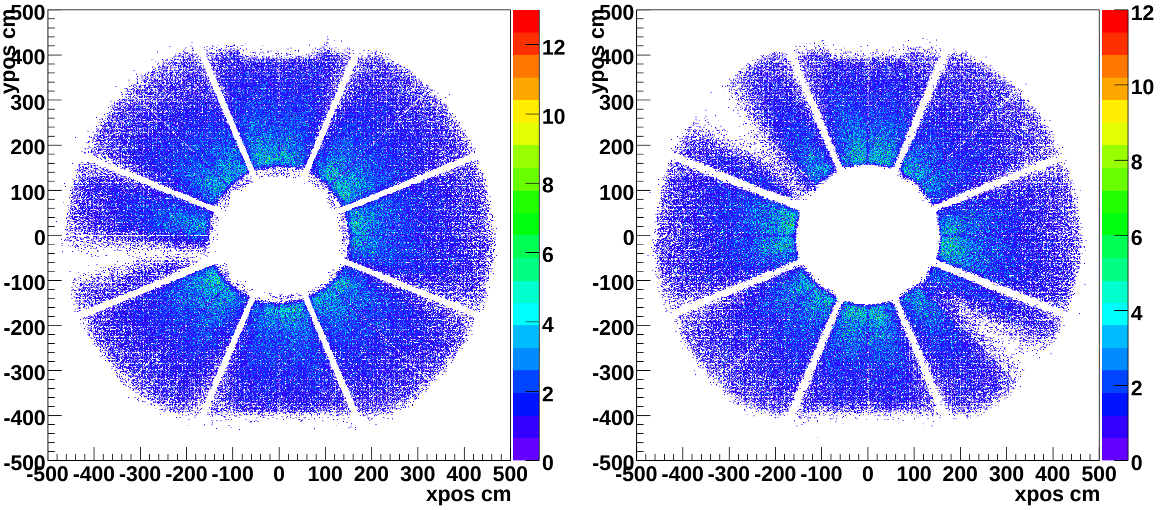

**Figure 6.35:** Left:Scatter distribution $xpos4$ and $ypos4$ of simulated muon tracks in North arm. Right:Same one in the South arm.

### 6.8.3 $p_T$ resolution and bin size

The simulated measured mass distributions of $J/\psi$ pairs with generated $p_T$, 0.0∼0.01, 0.5∼0.51, 1.0∼1.01, 3.0∼3.01, and 5.0∼5.01 GeV/$c$ , are shown in Figure 6.36. The width of $J/\psi$ mass distribution in p+p data in Fig. 6.19∼ 6.31 are consistent with the simulated distribution. So that resolution is well measured in the monte calro.

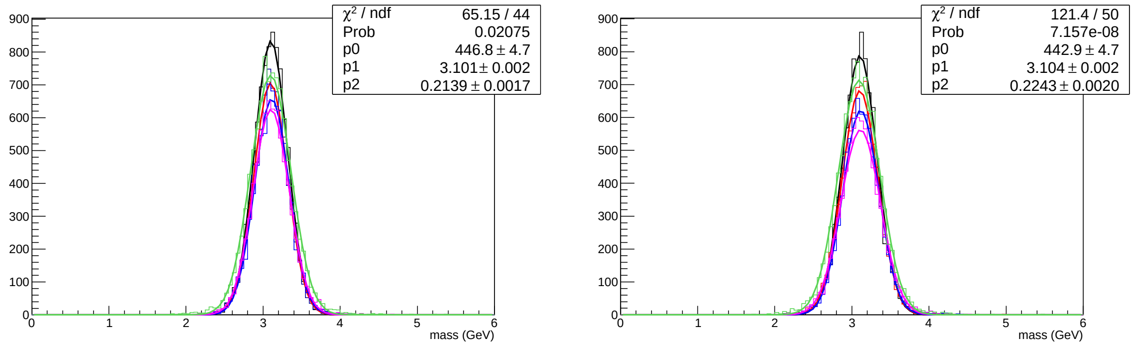

**Figure 6.36:** Left:The simulated measured mass distributions of $J/\psi$ pairs with generated $p_T$, 0.0∼0.01, 0.5∼0.51 (Red), 1.0∼1.01 (blue), 3.0∼3.01 (magenta), and 5.0∼5.01(green) GeV/$c$ in North arm. Right:Same one in the South arm.

The correspondent $p_T$ distributions of $J/\psi$ pairs with generated $p_T$, 0.0∼0.01, 0.5∼0.51, 1.0∼1.01, 3.0∼3.01, and 5.0∼5.01 GeV/$c$ , are shown in Figure 6.37. Simulated $p_T$ resolution of north(south) arm are in the $p_T$ range is 200∼250 (200∼300) MeV. The used $p_T$ bins sizes in the analysis are large enough than the resolutions.

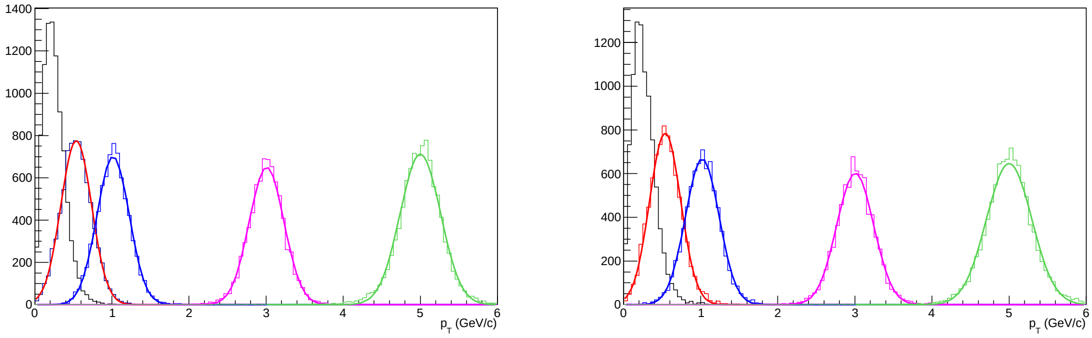

**Figure 6.37:** Left:The simulated measured $p_T$ distributions of $J/\psi$ pairs with generated $p_T$, 0.0∼0.01, 0.5∼0.51 (Red), 1.0∼1.01 (blue), 3.0∼3.01 (magenta), and 5.0∼5.01(green) GeV/$c$ in North arm. Right:Same one in the South arm.

### 6.8.4 Weighting function

In this analysis, $(Acc \cdot \epsilon_{reco} \cdot \epsilon_{cuts})$ are decided from the simulations. It has a dependence on rapidity and $p_T$ distributions. On the other hands, ”Flat distribution in $p_T$ and rapidity” is obviously an unrealistic condition, and there is no well accepted theoretical prediction for UPC. Therefore, the following procedure is taken to create realistic distributions. Because of low statistic, it is assumed that the $p_T$ and rapidity dependence are independently.

1. Make $(Acc \cdot \epsilon_{reco} \cdot \epsilon_{cuts})$ for flat distributions. It is defined as $\frac{\sum_{p_T^{reconstructed} \in bin}}{\sum_{p_T^{generated} \in bin}}$
2. Make $\frac{dN/dp_T}{(Acc \cdot \epsilon_{reco} \cdot \epsilon_{cuts})}$ and $\frac{dN/dy}{(Acc \cdot \epsilon_{reco} \cdot \epsilon_{cuts})}$ distributions. The $\frac{dN}{dp_T}$ are the measured $p_T$ distributions.
3. Fit them with the hypothetical functions.
4. Weight distributions in $p_T$ and rapidity with the hypothetical functions, and remake $(Acc \cdot \epsilon_{reco} \cdot \epsilon_{cuts})$ distributions.
5. Remake $\frac{dN/dp_T}{(Acc \cdot \epsilon_{reco} \cdot \epsilon_{cuts})}$ and $\frac{dN/dy}{(Acc \cdot \epsilon_{reco} \cdot \epsilon_{cuts})}$distributions, and iterated above steps until $(Acc \cdot \epsilon_{reco} \cdot \epsilon_{cuts})$ converging.

**The hypothetical functions** The $\frac{dN/dp_T}{(Acc \cdot \epsilon_{reco} \cdot \epsilon_{cuts})}$ and $\frac{dN/dy}{(Acc \cdot \epsilon_{reco} \cdot \epsilon_{cuts})}$ distributions in the first step (Flat $p_T$ and rapidity) are shown in Fig. 6.38. Due to low statistics, $dN/dy$ distributions are divided just four bins. A bin size of $dN/dp_T$ distributions were decided that each bin in real $dN/dp_T$ distributions should have at least one event. The rapidity distributions are normalized to 4, easy to see. $e^{Ap_T} \times (B|y| + 1.7)$ looks good enough to fit the data. (1.7 was fixed by the reason that the integrated value should be four, the one corresponds to no change.)

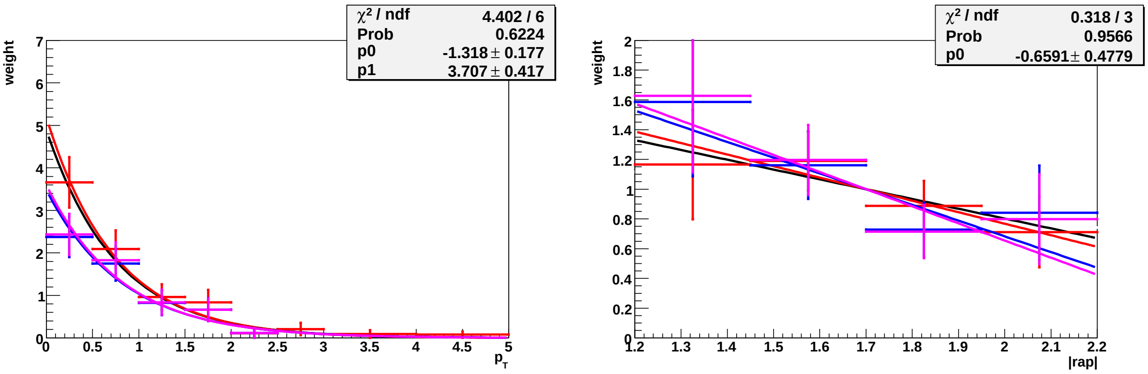

**Figure 6.38:** Left:The $\frac{real-dN/dp_T}{Acc \times \epsilon}$ distributions and its fitting result. Right:The $\frac{real-dN/dy}{Acc \times \epsilon}$ distributions and its fitting result. In each figure, Black line corresponds to unpolarized pairs in the North arm, red corresponds to full transverse polarized pairs in the North arm, blue corresponds to unpolarized pairs in the South arm, magenta corresponds to full-polarized pairs in the South arm.

**Iteration** The procedure was iterated until to have a limit (five times). The A and B values of each step are shown in Tab. 6.3and 6.4. The final results are shown in Fig. 6.39.

**Table 6.3:** The A and B values of each iteration step in unpolarized case

| - | A(unpol N) | B(unpol N) | A(unpol S) | B(unpol S) |
|---|---|---|---|---|
| 1st | -0.66±0.48 | -1.3±0.2 | -0.77±0.47 | -1.3±0.2 |
| 2nd | -1.0±0.5 | -1.4±0.18 | -1.2±0.5 | -1.4±0.2 |
| 3rd | -1.1±0.5 | -1.4±0.2 | -1.1±0.5 | -1.4±0.2 |
| 4th | -1.1±0.5 | -1.4±0.2 | -1.1±0.5 | -1.4±0.2 |
| 5th | -1.1±0.5 | -1.4±0.2 | -1.1±0.5 | -1.4±0.2 |
| 6th | -1.1±0.5 | -1.4±0.2 | -1.1±0.5 | -1.4±0.2 |

**Table 6.4:** The A and B values of each iteration step for full pol case

| - | A(full pol N) | B(Full pol N) | A(full pol S) | B(fullpol S) |
|---|---|---|---|---|
| 1st | -1.1±0.6 | -1.2±0.2 | -1.2±0.6 | -1.2±0.2 |
| 2nd | -1.4±0.6 | -1.2±0.2 | -1.4±0.6 | -1.3±0.2 |
| 3rd | -1.4±0.6 | -1.2±0.2 | -1.4±0.6 | -1.3±0.2 |
| 4th | -1.4±0.6 | -1.2±0.2 | -1.4±0.6 | -1.3±0.2 |
| 5th | -1.4±0.6 | -1.2±0.2 | -1.4±0.6 | -1.3±0.2 |
| 6th | -1.4±0.6 | -1.2±0.2 | -1.4±0.6 | -1.3±0.2 |

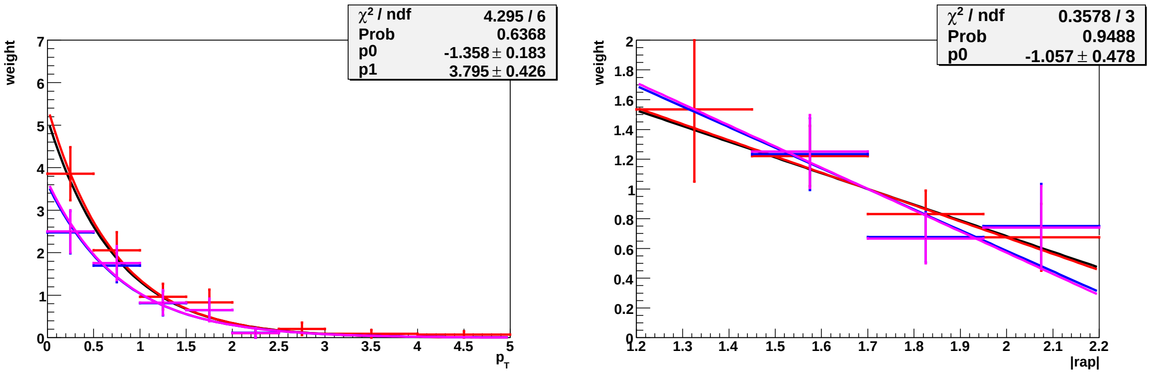

**Figure 6.39:** Left: The $\frac{real-dN/dp_T}{Acc\times\epsilon}$ distributions and their fitting results. Right:The $\frac{real-dN/dy}{Acc\times\epsilon}$ distributions and their fitting results. In each figure, Black line corresponds to unpolarized pairs in the North arm, red corresponds to full transverse polarized pairs in the North arm, blue corresponds to unpolarized pairs in the South, magenta corresponds to full-polarized pairs in the South arm.

### 6.8.5 $(Acc \cdot \epsilon_{reco} \cdot \epsilon_{cuts})$

The $p_T$ and rapidity dependence of $(Acc \cdot \epsilon_{reco} \cdot \epsilon_{cuts})$ in each arm are shown in Fig 6.40 and 6.41.

As same as the 2007 central-rapidity analysis, black and red correspond to the values obtained with unpolarized and transversely polarized, respectively. Their average values (blue) are taken as the central values and the difference is taken as a systematic uncertainty. Different from the central-rapidity data, lower $p_T$ peak are not so clear, then even the lowest bin, the same procedure is taken.

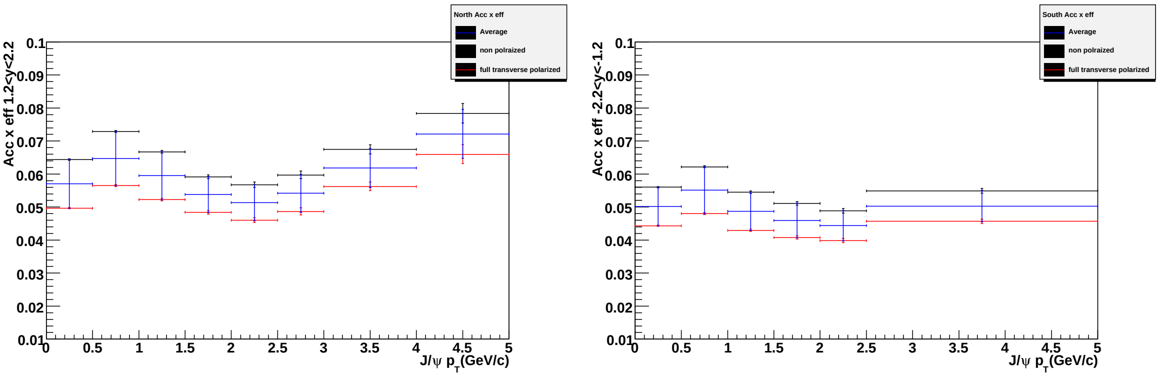

**Figure 6.40:** Left:The rapidity integrated $p_T$ dependence of $(Acc \cdot \epsilon_{reco} \cdot \epsilon_{cuts})$ in the North arm. Right:The rapidity integrated $p_T$ dependence of $(Acc \cdot \epsilon_{reco} \cdot \epsilon_{cuts})$ in the South arm.

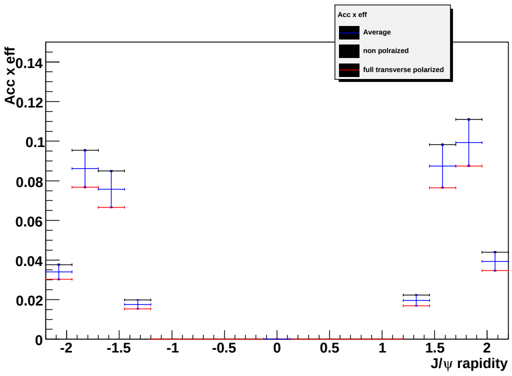

**Figure 6.41:** The $p_T$ integrated rapidity dependence of $(Acc \cdot \epsilon_{reco} \cdot \epsilon_{cuts})$.

## 6.9 Cross section result

### 6.9.1 The extraction of $dN_{J/\psi}/dp_T$

The $p_T$ distribution of the UPC $J/\psi$ is estimated by subtracting the expected most peripheral contamination (Fig 6.15) form Tab. 6.1.

The result is shown in Fig. 6.42 and Tab. 6.5.

**Table 6.5:** The extraction of $dN_{J/\psi}/dp_T$ distribution of UPC $J/\psi$ $+XnYn$ in the 2010 PHENIX run

| $p_T$ (GeV/$c$ ) | 0∼0.5 | 0.5∼1. 0 | 1.0∼1.5 | 1.5∼2.0 | 2.0∼2.5 | 2.5∼3.0 | 3.0∼4.0 | 4.0∼5.0 |
|---|---|---|---|---|---|---|---|---|
| North counts | 34.6 | 20.7 | 10.0 | 9.0 | 1.0 | 3.0 | 2.0 | 1.0 |
| Statistical error | 6.4 | 5.0 | 3.2 | 3.0 | 1.0 | 1.7 | 1.4 | 1.0 |
| Systematic error | 2 | 1 | - | - | - | - | - | - |
| Normalized p+p | 0.311 | 0.632 | 0.654 | 0.451 | 0.286 | 0.174 | 0.168 | 0.0543 |
| Result | 34.3 | 20.1 | 9.35 | 8.55 | 0.714 | 2.83 | 1.83 | 0.946 |
| South counts | 18.4 | 15.3 | 8 | 5 | 1 | - | - | - |
| Statistical error | 4.85 | 4.39 | 2.83 | 2.24 | 10 | - | - | - |
| Systematic error | 1 | 1 | - | - | - | - | - | - |
| Normalized p+p | 0.3 | 0.6 | 1.3 | 1.1 | 0.31 | 0.3 | 0.10 | 0.04 |
| Result | 18.1 | 14.6 | 7.36 | 4.53 | 0.723 | - | - | - |

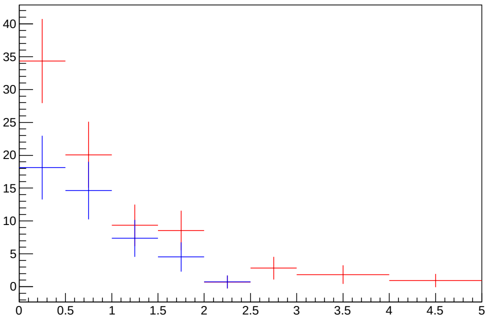

**Figure 6.42:** The $p_T$ distributions of UPC $J/\psi$ The red (blue) line corresponds to north (south).

### 6.9.2 The extraction of $dN_{J/\psi}/dy$

The rapidity distribution is estimated as Fig 6.44 and subtracted p+p and continuum rapidity distributions are shown in Fig 6.43. The $p_T$ distribution of the UPC $J/\psi$ is estimated with following steps;

1. Make the rapidity distribution with the cut of 2.7 GeV/$c^2$ $\leq$ mass. The distribution is shown in the right panel of Fig 6.44.

2. Subtract rapidity distribution of p+p $J/\psi$, shown in the left panel of Fig 6.43, which is normalized to expected yield.

3. Make rapidity distribution with the cut of mass $\geq$ 2.7GeV/$c^2$ & $p_T \leq 1.0$ GeV/$c$ and take as a continuum rapidity distribution. It corresponds to assume the rapidity distribution of continuum background is independent of the mass. The distribution was normalized to the integrated value of rapidity distribution of the subtracted result, shown in the left panel of Fig 6.44, should have same integrated value of Fig 6.42. The normalized result is shown in the right panel of Fig 6.43 and Tab 6.6.

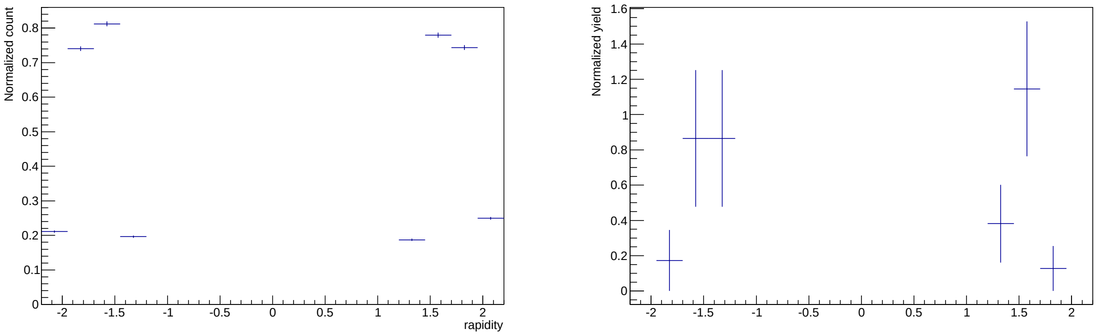

**Figure 6.43:** Left:The rapidity distribution of p+p unlike-sign pairs where the event has the pair with mass form 2.6 to 3.6 GeV/$c^2$ . Right:The rapidity distribution of final samples where the event has a pair with 2.6GeV/$c^2$ $\leq$ mass. Both distributions are normalized to expected yield .

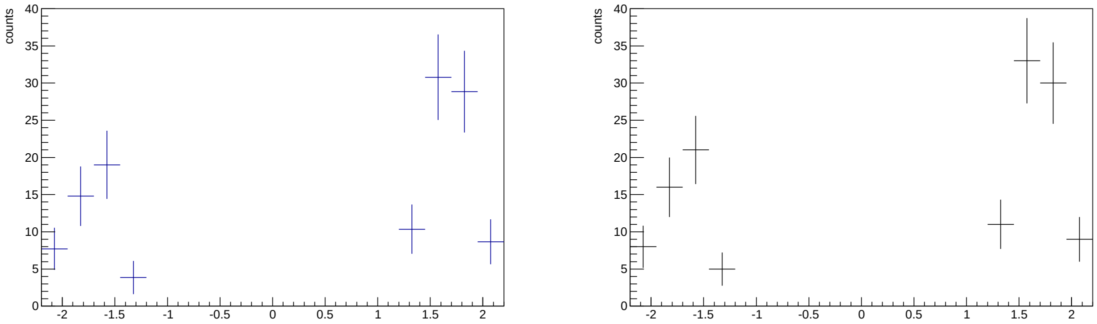

**Figure 6.44:** Left:The rapidity distribution UPC $J/\psi$. Right:rapidity distribution of final samples at 2.6 $\sim$ 3.6 GeV/$c^2$ (without subtraction).

**Table 6.6:** The extraction of $dN_{J/\psi}/dy$of both side neutron tagged $J/\psi \rightarrow \mu^+\mu^-$in the 2010 PHENIX run

| rapidity | -2.2~-1.95 | -1.95~-1.7 | -1.7~-1.45 | -1.45~-1.2 | 1.2~1.45 | 1.45~1.7 | 1.7~1.95 | 1.95~2.2 |
|---|---|---|---|---|---|---|---|---|
| count | 68 | 16 | 21 | 5 | 11 | 33 | 30 | 9 |
| Statistical error | 2.83 | 4 | 4.58 | 2.24 | 3.32 | 5.74 | 5.48 | 3 |
| Normalized p+p | 0.294 | 1.03 | 1.13 | 0.274 | 0.261 | 1.09 | 1.04 | 0.3475 |
| Normalized background | -0 | 0.173 | 0.865 | 0.865 | 0.382 | 1.15 | 0.127 | 0 |
| Statistical error | 0 | 0.173 | 0.387 | 0.387 | 0.22 | 0.382 | 0.127 | 0 |
| Result | 7.71 | 14.8 | 19 | 3.86 | 10.4 | 30.8 | 28.8 | 8.65 |
| Statistical error | 2.83 | 4 | 4.58 | 2.24 | 3.32 | 5.75 | 5.49 | 3.02 |

### 6.9.3 Summary of Systematic errors

The systematic error was calculated by following equation.

$$\frac{\epsilon_{totalsys}}{\sigma} = \sqrt{\left(\frac{\epsilon_{Acc\times\epsilon}}{Acc \times \epsilon}\right)^2 + 0.05^2 + \left(\frac{\epsilon_{L_{int}}}{L_{int}}\right)^2 + + \left(\frac{Njpsi_{sys}}{Njpsi}\right)^2 + \left(\frac{\epsilon_{\epsilon_{BBCVETO}}}{\epsilon_{BBCVETO}}\right)^2} \qquad (6.5)$$

Here

1. Type A and B:$Njpsi_{sys}$ is systematic error of $J/\psi$ counting. It is the defined as the square of the yield of subtracted backgrounds at 2.6$\leq$ mass $\leq$ 3.6 GeV/$c^2$ , most peripheral (p+p) and continuum, respectably.
2. Type B:$\epsilon_{Acc\cdot\epsilon_{reco}\cdot\epsilon_{cuts}}$ is the systematic error shown in Fig 6.40 and 6.41. The sources were simulation statistical error and $\frac{|pol-nonpol|}{2}$
3. Type B:0.05 is the systematic error of simulation itself, 5% [72]
4. Type B:$\epsilon_{L_{int}}$ is the statistical error of integrated luminosity.
5. Type B:$\epsilon_{\epsilon_{BBCVETO}}$ is the statistical error to estimate $\epsilon_{BBCVETO}$.

### 6.9.4 $d^2\sigma/dp_Tdy$ distribution

The $J/\psi$ cross section in a given rapidity and transverse momentum bins were calculated according to,

$$\frac{d^2\sigma}{\Delta p_T \Delta y} = \frac{1}{B_{\mu^+\mu^-} dp_T dy} \frac{N_{J/\psi} - N_{background}}{(Acc \cdot \epsilon_{reco} \cdot \epsilon_{cuts}) \cdot \epsilon_{trigger} \cdot \mathcal{L}_{int}} \qquad (6.6)$$

$$(6.7)$$

The results are shown in Fig. 6.45 and Tab. 6.7.

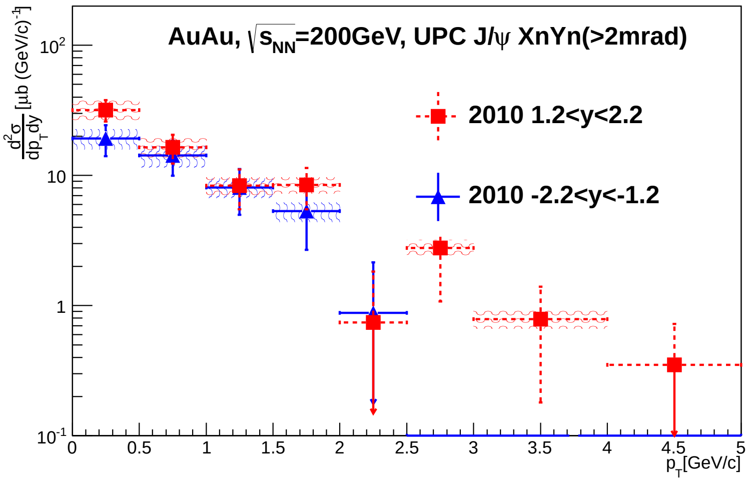

**Figure 6.45:** The $d^2\sigma/dp_Tdy$ distribution of UPC $J/\psi$ $+XnYn$ in the 2010 PHENIX run. The blue line corresponds to the result of the South arm, the red line corresponds to the result of the North arm. The magenta line corresponds to result of the central arm.

**Table 6.7:** The $d^2\sigma/dp_Tdy$ of UPC $J/\psi$ $+XnYn$ in the 2010 PHENIX run

| $p_T$ (GeV/$c$ ) | 0∼0.5 | 0.5∼1. 0 | 1.0∼1.5 | 1.5∼2.0 | 2.0∼2.5 | 2.5∼3.0 | 3.0∼4.0 | 4.0∼5.0 |
|---|---|---|---|---|---|---|---|---|
| North $d^2\sigma/dp_Tdy$ | 34.3 | 17.7 | 8.94 | 9.09 | 0.797 | 2.98 | 0.848 | 0.378 |
| Statistical error | 6.38 | 4.42 | 3.03 | 3.19 | 1.16 | 1.83 | 0.655 | 0.402 |
| Systematic error | 6.35 | 3.01 | 1.45 | 1.25 | 0.335 | 0.43 | 0.129 | 0.0486 |
| South $d^2\sigma/dp_Tdy$ | 21.6 | 16 | 9.1 | 5.97 | 0.988 | - | - | - |
| Statistical error | 5.78 | 4.8 | 3.5 | 2.94 | 1.42 | - | - | - |
| Systematic error | 3.78 | 3.02 | 1.53 | 1.03 | 0.3996 | - | - | - |

### 6.9.5 $d\sigma/dy$ distribution

The results of both side neutron tagged $J/\psi \rightarrow \mu^+\mu^-$in the 2010 PHENIX run and $J/\psi \rightarrow e^+e^-$in the 2007 PHENIX run are shown in Fig. 6.46 and Tab. 6.8.

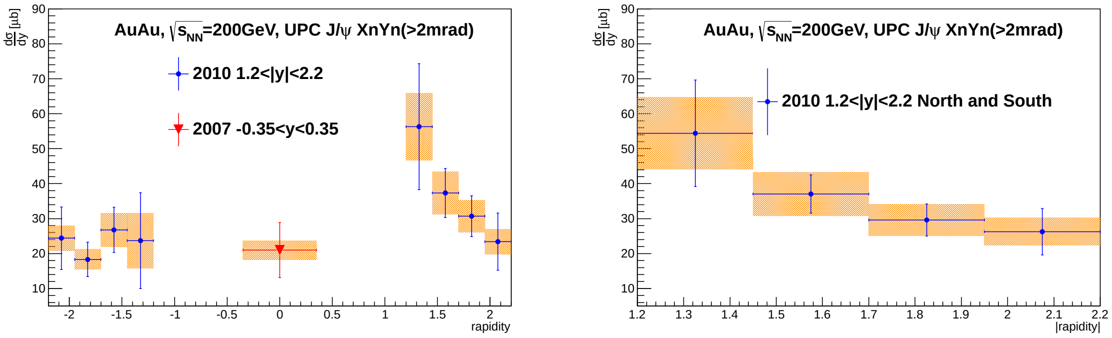

**Figure 6.46:** The $d\sigma/dy$ distribution of both side neutron tagged $J/\psi \rightarrow \mu^+\mu^-$in the 2010 PHENIX run.

**Table 6.8:** The $d\sigma/dy$ of both side neutron tagged $J/\psi \rightarrow \mu^+\mu^-$in the 2010 PHENIX run

| rapidity | -2.2∼-1.95 | -1.95∼-1.7 | -1.7∼-1.45 | -1.45∼-1.2 | 1.2∼1.45 | 1.45∼1.7 | 1.7∼1.95 | 1.95∼2.2 |
|---|---|---|---|---|---|---|---|---|
| $d^2\sigma/dp_Tdy$ | 26.2 | 19.7 | 28.8 | 25.5 | 63.3 | 42 | 34.5 | 26.3 |
| Statistical error | 9.63 | 5.33 | 6.94 | 14.7 | 20.3 | 7.84 | 6.57 | 9.19 |
| Systematic error | 3.8 | 3.08 | 5.18 | 8.43 | 10.8 | 6.87 | 5.17 | 3.97 |
| combined $d^2\sigma/dp_Tdy$ | - | - | - | - | 54.4 | 37 | 29.6 | 26.3 |
| Statistical error | - | - | - | - | 15.2 | 5.47 | 4.61 | 6.65 |
| Systematic error | - | - | - | - | 10.2 | 6.24 | 4.48 | 3.89 |

# Chapter 7

# Results and discussion

## 7.1 One side forward neutron tagged UPC $J/\psi$

The $d\sigma/dy$ and $(1/2\pi p_T)d^2N/dp_Tdy$ $[(\mathrm{GeV}/c)^{-2}]$of UPC $J/\psi$ $+Xn$ in Au+Au at $\sqrt{s_{NN}} = 200$ GeV, $|y| < 0.35$ were measured by the data in the PHENIX 2007 year run.

### 7.1.1 One side neutrons tagging result($J/\psi$ $+Xn$)

The 2007 and 2004 PHENIX run combined result,

$$\frac{d\sigma}{dy} = 55.9 \pm 13.2\,(\mathrm{stat}) \pm 7.6\,(\mathrm{sys})\ \ \mu\mathrm{b} \tag{7.1}$$

The result together with theoretical curves is shown in Fig 7.1 [38] [42] [43] [42].

The combined result is consistent with both Strikman and Kopeliovich coherent and incoherent theoretical curves in the central rapidity.

The details of theoretical predictions in Fig 7.1 are following.

- STARLIGHT : Just for comparison, no shadowing, parameterize to HERA data [40].
- Strikman: $\sigma_{J/\psi N}$ is assumed to 3 mb [38].
- Kopeliovich:The dipole cross section is treated as a function of $r_t$, $\sqrt{s}$, $\sqrt{s}$ is the center of mass energy, $r_T$ is the transverse $q\bar{q}$ separation. Calculations were performed with KST and GBW parameterizations for the dipole cross section, [41].
- Goncalves-Machado: Gluon saturation is assumed [42].

The 2007 only result is as follows;

$$\frac{d\sigma}{dy} = 45.6 \pm 13.2\,(\mathrm{stat}) \pm 6.0\,(\mathrm{sys})\ \ \mu\mathrm{b}. \tag{7.2}$$

Theoretical curves are shown in Fig 7.2 [30, 40, 38, 41, 42, 43].

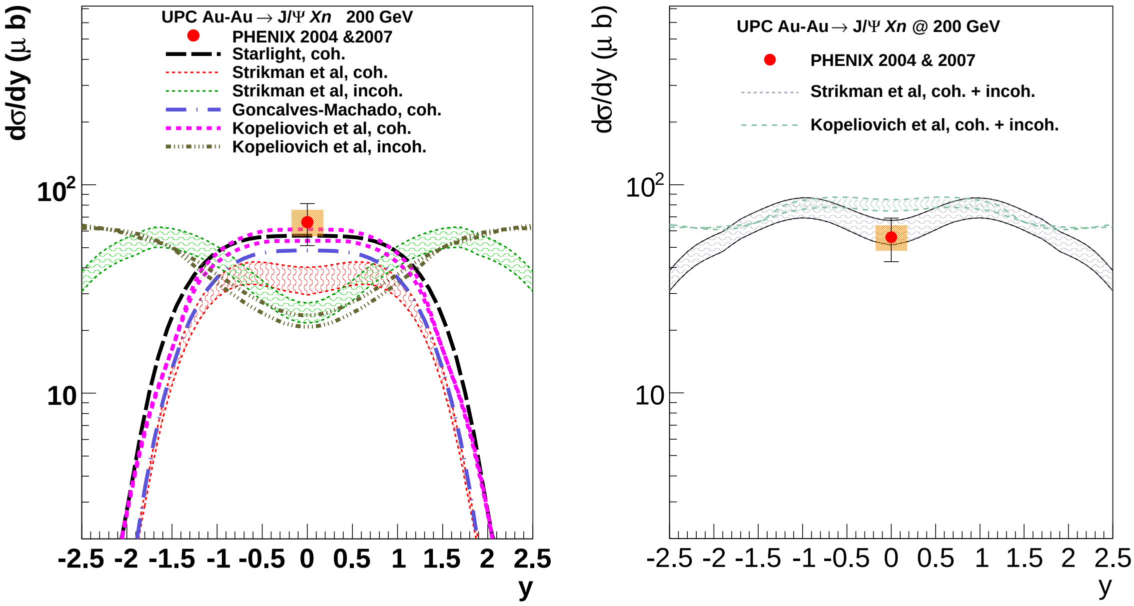

**Figure 7.1:** Right : The 2004 and 2007 combined cross-section compared to theoretical curves [30, 40, 38, 41, 42, 43]. Left :The 2004 and 2007 combined cross-section compared to theoretical curves [38, 41] of coherent + incoherent .

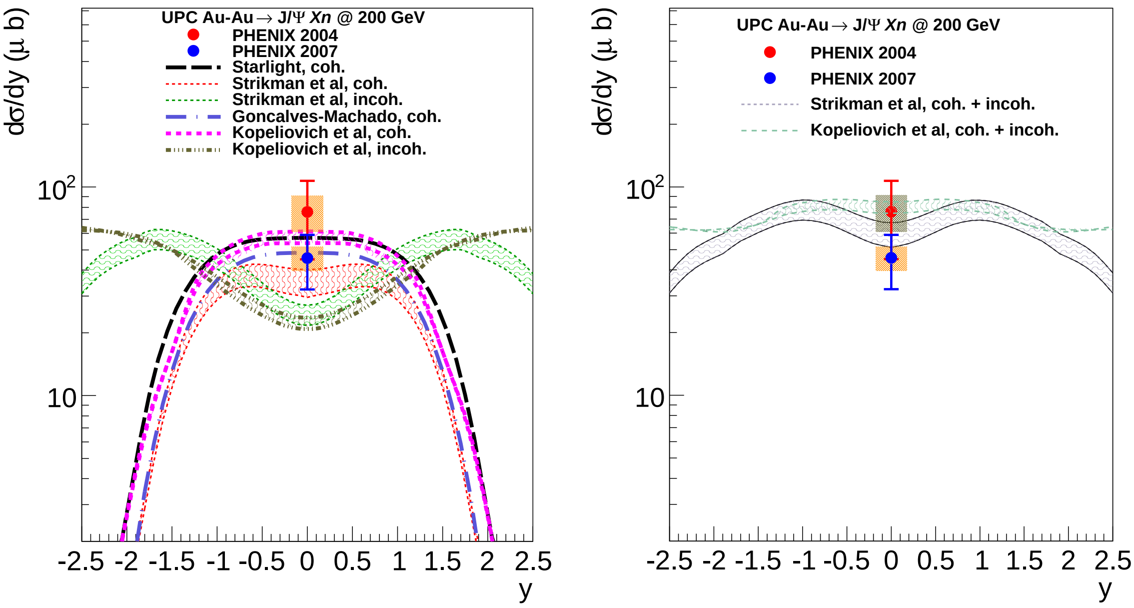

**Figure 7.2:** Left: $d\sigma/dy$ compared to theoretical curves [30, 40, 38, 41, 42, 43] of coherent or incoherent and the previous result in the 2004 PHENIX run. Right: $d\sigma/dy$ compared to theoretical curves [38, 41] of coherent + incoherent and the previous result in the 2004 PHENIX run.

### The double differential cross section on $y$ and $p_T$

The $(1/2\pi p_T)d^2N/dp_Tdy$ $[(\mathrm{GeV}/c)^{-2}]$distribution of Ultra-Peripheral Au+Au Collisions at $\sqrt{s_{NN}}$ = 200 GeV in th 2007 PHENIX run is shown in Fig 7.3. Almost all theoretical predictions expect coherent peak at $p_T$ ~0 and wider $p_T$ distribution for incoherent process [30, 40, 38, 41, 42, 43]. The data clearly shows coherent peak at $p_T < 0.4$ GeV/$c$ . The $d\sigma/dy$ for $p_T < 0.4$ GeV/$c$ is following;

$$\frac{d\sigma}{dy}|_{p_T<0.4} = 31 \pm 9\,(\mathrm{stat}) \pm 4\,(\mathrm{sys})\ \ \mu\mathrm{b}. \tag{7.3}$$

For $p_T > 0.4$ GeV/$c$ is following;

$$\frac{d\sigma}{dy}|_{p_T>0.4} = 14 \pm 7\,(\mathrm{stat}) \pm 2\,(\mathrm{sys})\ \ \mu\mathrm{b}. \tag{7.4}$$

14± 7 ±2 $\mu$b can be assumed as the lower limit of $d\sigma/dy$ of the incoherent UPC $J/\psi$. It shows existing of incoherent process in the mid rapidity region with one sigma criteria.

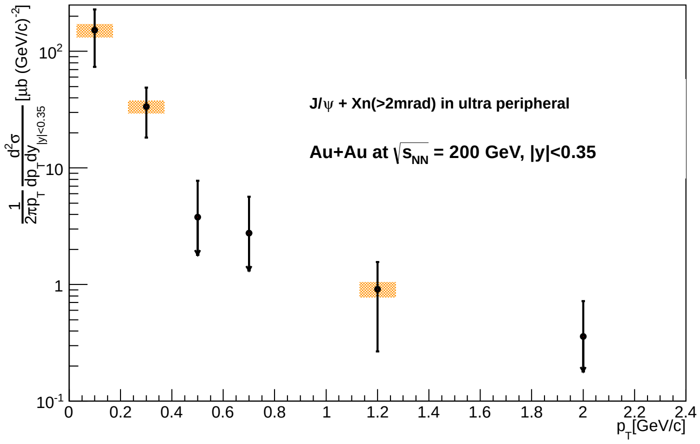

**Figure 7.3:** The $(1/2\pi p_T)d^2N/dp_Tdy$ $[(\mathrm{GeV}/c)^{-2}]$distribution in Ultra-Peripheral Au+Au Collisions at $\sqrt{s_{NN}}$ = 200 GeV in the 2007 PHENIX run.

### 7.1.2 Comparison with collinear approach

Since $d\sigma/dy$ from all theoretical calculations gives flat distribution in $y$, $\frac{d\sigma}{dy}$ at $y = 0$ in coherent UPC $J/\psi$ $+Xn$ is estimated as: [29]. In the calculation, the nuclear breakup probability is assumed as 0.64.

- No shadowing, 113 $\mu$b [29].
- DS, 108 $\mu$b: [29, 32].
- EKS, 83 $\mu$b: [29, 33].
- EPS, 53 $\mu$b: [29, 22].

Obviously, the new data, 31± 9±4 $\mu$b is quite lower than 113 $\mu$b, which corresponds to $R = 1$. The new experimental data is important information to understand gluon physics in nuclear.

### 7.1.3 Compared with the color dipole approach

Theoretical predictions from leading twist order predictions are following [38, 41].

**Strikman**

1. Strikman Glauber ($\sigma^{tot}_{J/\psi N}$= 3 mb):29$\mu$b [38]
2. Strikman Impulse ($\sigma^{tot}_{J/\psi N}$= 0 mb):40$\mu$b [38]

Both predictions are consistent with the measured cross-section within the uncertainties.

**Kopeliovich**

1. Kopeliovich-KST:53$\mu$b [41]
2. Kopeliovich-GBW:60$\mu$b [41]

In color dipole aproach, dipole cross section is important, which takes into account the shadowing effects. Kopeliovich tests two dipole parameterization, well known GBW parameterization [73] and his new KST parameterization [74]. GBW well describes data for DIS at small $x$ and at medium ∼ large $Q^2$ and cannot be applied at small $Q^2$, KST well describes data for DIS at small $x$ and at small ∼ medium $Q^2$ (up to about 10∼20 (GeV/c)$^2$), where $Q^2$ in UPC $J/\psi$ production is well covered.

## 7.2 Double-side forward neutron tagging $J/\psi$ production

### 7.2.1 Both side neutron tagging result($J/\psi$ $+XnYn$)

The $\frac{d^2\sigma}{dydp_T}$ of UPC $J/\psi$ $+XnYn$ in Au+Au at $\sqrt{s_{NN}}$ = 200 GeV in the 2010 PHENIX run is shown in Fig 7.4. The peak of low $p_T$ is not so significant and that the wider $p_T$ distribution is dominant at the rapidity region. The $d\sigma/dy$ distribution of UPC $J/\psi$ $+XnYn$ in Au+Au at $\sqrt{s_{NN}}$ = 200 GeV is shown in Fig 7.5

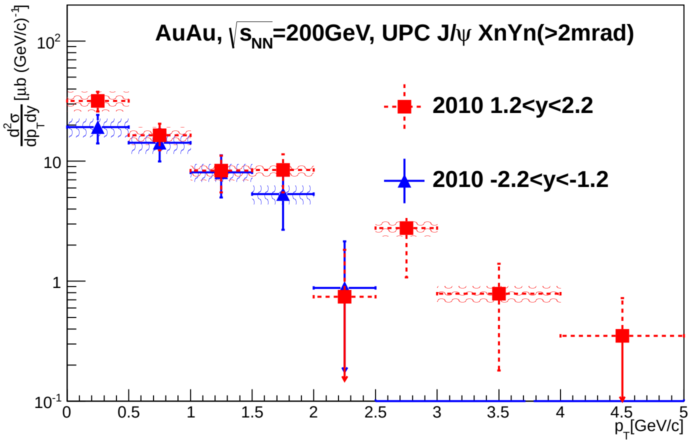

**Figure 7.4:** $\frac{d^2\sigma}{dydp_T}$ of UPC $J/\psi$ $+XnYn$ in Au+Au at $\sqrt{s_{NN}}$ = 200 GeV in the 2010 PHENIX run.

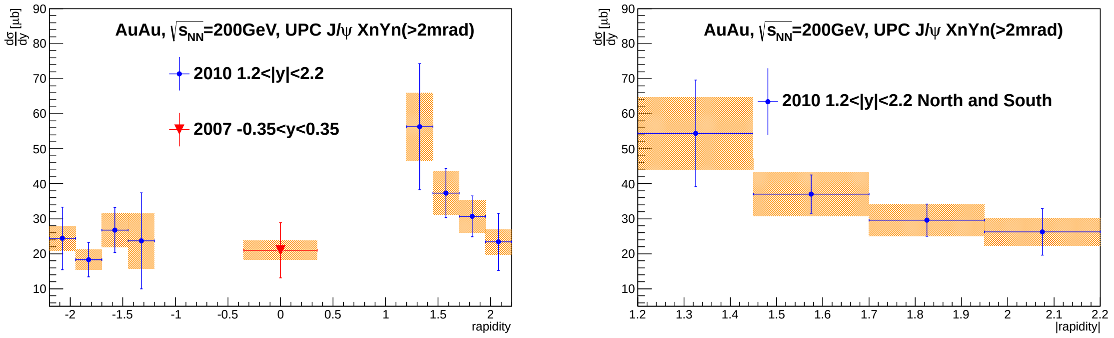

**Figure 7.5:** The $d\sigma/dy$ distribution of UPC $J/\psi$ $+XnYn$ in Au+Au at $\sqrt{s_{NN}}$ = 200 GeV

### 7.2.2 The number of emitted neutrons

The distributions of ZDC energy deposit for event with $J/\psi$ in $1.2 < |y| < 2.2$ are shown in Fig 6.10. The mean values of the ZDC energy distribution which is the same side of measured $J/\psi$ are significantly higher than the other one which is the opposite side of measured $J/\psi$.

In the measurement, mean value of the energy distribution of ZDC of the opposite side of measured $J/\psi$ is 700 GeV, while that value for the ZDC of the same side of measured $J/\psi$ is about 1300GeV.

The symmetry can be an indication of the incoherent process, i.e. the nucleus which interacts with the photon break up.

The theoretical prediction of the distribution of number of emitted neutrons for incoherent events is shown in Fig 2.8 [38]. The average value is 4.5 neutrons. The distribution doesn't include neutrons from the electromagnetic excitation and its systematic error is not estimated.

# Chapter 8

# Summary

The measurement of UPC $J/\psi$ in Au+Au collisions at $\sqrt{s_{NN}} = 200$ GeV in the 2007 and 2010 PHENIX runs has been carried out with the PHENIX detectors.

Electron and positron for central rapidity($|y| < 0.35$) and dimuon pair for forward rapidity($1.2 < |y| < 2.2$) were used to reconstruct $J/\psi$ .

In both central and forward rapidity region, exclusive $J/\psi$ events are observed. The event topology of no presence of the other charged tracks in the central detectors is different from the hadronic production of $J/\psi$ and strongly suggests the photo-induced production. Especially this is the first measurement of the $J/\psi$ exclusive production in the forward rapidity region at this energy.

The cross sections of $J/\psi$ $+Xn$ production in the UPC at the central rapidity (y=0) are measured, where $Xn$ denotes that at least one neutron with energy more then 30 GeV is emitted within 2 mrad from the beam Axis. The results are;

$$\frac{d\sigma}{dy} = 45.6 \pm 13.2\,(\text{stat}) \pm 6.0\,(\text{sys})\ \ \mu\text{b}. \tag{8.1}$$

$$\frac{d\sigma}{dy}|_{p_T<0.4} = 31 \pm 9\,(\text{stat}) \pm 4\,(\text{sys})\ \ \mu\text{b}. \tag{8.2}$$

$$\frac{d\sigma}{dy}|_{p_T>0.4} = 14 \pm 7\,(\text{stat}) \pm 2\,(\text{sys})\ \ \mu\text{b}. \tag{8.3}$$

The sharp pt distribution at $p_T = 0$ demonstrates the presence of the coherent production process, while the existence of high $p_T$ (>0.4 GeV/$c$ ) events indicates the precence of the incoherent process at 2 sigma level.

The results of $p_T < 0.4$ GeV/$c$ cross section is well below the expectation from the case for simple assumption from the proton-proton extrapolation (113 $\mu$b) and suggests a strong suppression of gluon in the nuclei around $x$~0.01.

The combined result of the integrated cross section of $J/\psi$ $+Xn(< 2mrad)$ at $|y| < 0.35$ in the 2004 and 2007 is as follows.

$$\frac{d\sigma}{dy} = 55.9 \pm 13.2\,(\text{stat}) \pm 7.6\,(\text{sys})\ \ \mu\text{b} \tag{8.4}$$

The cross sections of $J/\psi$ $+XnYn$ was measured at the first time as a function of rapidity, where $+XnYn$ denotes that there are at least one neutron emitted in the both side of the beam direction (within 2 m rad). Clear signal are observed for the forward rapidity ($1.2 < |y| < 2.2$). The pt distribution shows a high $p_T$ tail without high concentration at $p_T \sim 0$. This suggests that these $J/\psi$ are producted in the incoherent process. The correlation between the $J/\psi$ rapidiy and the direction of high multiplicity forward neutron are also observed.

# Acknowledgments

First I would like to thank Prof. H. Hamagaki for all his help and direction during my Ph.D. I am very grateful to Dr. Y. Akiba for his appropriate advice and profound discussion about the PHENIX experiment, analysis and physics. A special thanks goes to Dr. T. Gunji in many discussing with me.

I would also like to thank all of my PHENIX collaborators. I would like to give many thanks to the sporksperson Prof. B.V. Jacak for her excellent leader ship. I appreciate Prof.J.S. Haggerty, the PHENIX Deputy Operations Director for Operations. This work is benefited especially from the same analysis team members, Zaida Conesa del Valle, Mickey Chiu, Joakim Nystrand, Sebastian White, Kyrre Skjerdal, Cesar Luiz da Silva, and Ermias T. Atomssa.

# Bibliography

[1] ZEUS Collaboration, phys. Rev. **D67** (2003)

[2] J.D. Bjorken, Proceedings 3rd International Conference on Electron and Photon Interactions, Stanford, (1967), Phys. Rev.**185** (1969) 1975 (with E.A. Paschos)

[3] J. Gomez *et al.,* Phys. Rev. D 49 (1994) 4348

[4] New Muon collaboration, P. Amaudruz *et al.,* Nucl. Phys.**B 441** (1995) 3

[5] New Muon. collaboration, M. Arneodo *et al.,* Nucl. Phys. **B 441** (1995) 12

[6] New Muon collaboration, M. Arneodo *et al.,* Nucl. Phys. **B 481** (1996) 3

[7] D.M. Alde *et al.,* Phys. Rev. Lett. **64** (1990) 2479

[8] FNAL E866 collaboration, M.A. Vasilev *et al.,* Phys. Rev. Lett. **b83** (1999) 2304.

[9] European Muon collaboration, J. Ashman *et al.,* Z. Phys. **C 57** (1993) 211

[10] New Muon collaboration, M. Arneodo *et al.,* Nucl.Phys. **B 481** (1996) 23

[11] Y. L. Dokshitzer. Sov. Phys. JETP **46**, 641 (1977). V. N. Gribov and L. N. Lipatov. Sov. J. Nucl. Phys. **15**, 438 (1972). G. Altarelli and G. Parisi.Nuclear Physics B **126**, 298 (1977). ISSN 0550-3213.

[12] arXiv:hep-ph/0604108

[13] Armesto N, Capella A, Kaidalov A B, Lopez-Albacete J and Salgado C A 2003 Eur. Phys. J. **C29** 531

[14] Hirai M, Kumano S and Miyama M 2001 Phys. Rev. **D 64** 034003

[15] Huang Z, Lu H J and Sarcevic I 1998 Nucl. Phys. **A** 637 79

[16] Bartels J, Gotsman J, Levin E M, Lublinsky M and Maor U 2003 Phys. Rev.**D 68** 054008

[17] Frankfurt L L, Guzey V, McDermott M and Strikman M I 2002 JHEP 0202 027

[18] Armesto N 2002 Eur. Phys. J.**C 26** 35

[19] Eskola K J, Kolhinen V J and Salgado C A 1999 Eur. Phys. J. **C 9** 61

[20] Eskola K J, Kolhinen V J and Ruuskanen P V 1998 Nucl. Phys.**B 535** 351

[21] Li S y and Wang X N 2002 Phys. Lett. **B 527** 85

[22] Eskola, Paukkunen, Salgado, JHEP **04** (2009) 065

[23] K. Hencken *et al.*, Phys. Rept. **458**, 1 (2008) [arXiv:0706.3356 [nucl-ex]].

[24] G. Baur, K. Hencken, D. Trautmann, S. Sadovsky, Y. Kharlov, Phys. Rept. **364** (2002) 359-450.

[25] C. A. Bertulani, S. R. Klein, J. Nystrand, Ann. Rev. Nucl. Part. Sci. **55** (2005) 271-310.

[26] C. F. von Weizsacker, Z. Phys. **88** (1934) 612-625.

[27] E. J. Williams, Phys. Rev. **45** (1934) 729-730.

[28] M. G. Ryskin, Z. Phys., **C37** (1993) 89.

[29] A. L. Ayala Filho, V.P. Goncalves, and M. T. Griep Phys. ReV. **C.78**. 044904

[30] A. Adare *et al.,* Physics Letters **B 679**, 321 (2009)

[31] A. J. Baltz, S. R. Klein, J. Nystrand, Phys. Rev. Lett.**89** (2002) 012301, private

[32] D. de Florian and R. Sassot, Phys. Rev. **D 69**, 074028 (2004)

[33] K. J. Eskola, V. J. Kolhinen, and P. V. Ruuskanen, Nucl. Phys. **B535**, 351 (1998); K. J. Eskola, V. J. Kolhinen, and C. A. Salgado, Eur. Phys. J.**C9**, 61 (1999).

[34] M. Hirai, S. Kumano, and T. H. Nagai, Phys. Rev. **C76**, 065207 (2007).

[35] V.N. Gribov, Sov. J. Nucl. Phys. **9** (1969) 369; V.N. Gribov, Sov. Phys. JETP **29** (1969) 483; V.N. Gribov, Sov. Phys. JETP **30** (1970) 709.

[36] L. Frankfurt, M. Strikman, M. Zhalov, Physics Letters **B** 540 (2002) 220-226

[37] H1 Collaboration, C. Adloff, et al., Eur. Phys. J. **C 20** (2001)29.

[38] M. Strikman, M. Tverskoy and M. Zhalov, Phys. Lett. B 626 **72** (2005)

[39] V. Rebyakova, M.Strikman, MZhalov arXive:1109.0737v1, private communication

[40] J. Nystrand, Nucl. Phys. **A 752**(2005)470c; A.J. Baltz, S.R. Klein, J. Nystrand, Phys. Rev. Lett. **89** (2002) 012301; S.R. Klein, J. Nystrand, Phys. Rev. **C 60**(1999)014903.

[41] Yu. P. Ivanov, B. Z. Kopeliovich and I. Schmidt, arXiv:0706.1532 (2007).

[42] V. P. Goncalves and M. V. T. Machado, Int. J. Mod. Phys. D **16** 533 (2007)

[43] L. Frankfurt, V. Guzey, M. Strikman and M. Zhalov, JHEP **0308** 043 (2003)

[44] H.Hahn *et al.,* NUcl. Instr. and Meth. **A 499**, 245 (2003).

[45] K.H. Ackermann *et al.,* Nucl. Instr. and Meth. **A 499**, 624 (2003).

[46] K. Adcox *et al.,* Nucl. Instr. and Meth. **A 499**, 469 (2003).

[47] M. Adamczyk *et al.,* Nucl. Instr. and Meth. **A 499**, 437 (2003).

[48] B.B. Back *et al.,* Nucl. Instr. and Meth. **A 499**, 603 (2003).

[49] M. Allen *et al.,* Nucl. Instr. and Meth. **A 499**, 549 (2003).

[50] T. Ludlam, Nucl. Instr. and Meth. **A 499**, 428 (2003).

[51] C. Adler *et al.,* Nucl. Instr. and Meth. **A 470**, 488 (2001).

[52] C. Adler *et al.,* Nucl. Instr. and Meth. **A 499**, 433 (2003).

[53] Haggerty J *et al.,* Letter of Intent for PHENIX Reaction Plane Detector. PHENIX internal, 2006.

[54] S.H. Aronson *et al.,* Nucl. Instr. and Meth. **A 499**, 480 (2003).

[55] M. Aizawa *et al.,* Nucl. Instr. and Meth. **A 499**, 508 (2003).

[56] L. Aphecetche *et al.,* Nucl. Instr. and Meth. **A 499**, 521 (2003).

[57] Y. Akiba *et al.,* Nucl. Instr. and Meth. **A 433**, 143 (1999).

[58] H. Akikawa *et al.,* Nucl. Instr. and Meth. **A 499**, 537 (2003).

[59] S.S. Adler *et al.,* Nucl. Instr. and Meth. **A 499**, 560 (2003).

[60] http://www.rhichome.bnl.gov/RHIC/Runs/

[61] J.T.Mitchell *et al.,*Nucl. Instr. and Meth. **A 482**,491(2002).

[62] K.Adcox et al. PHENIX detector overview. ZNucl.Instrum. Meth., **A499**;469-479, 2003.

[63] Atomssa, Ermias Tujuba (2008) $J/\psi$ suppression and elliptic flow in 200 GeV Au+Au collisions at the mid rapidity region of the PHENIX experiment. PhD thesis Physique, Physics, EP/X p.180.

[64] $http : //home.thep.lu.se/\ torbjorn/pythia/lutp0613man2.pdf$

[65] Xiaorong Wang, Hussein Al-Ta'ani, S. Pate, G. Kyle, V. Papavassiliou PHENIX internal analisys note 921

[66] S. Chekanov *et al.,* Eur. Phys. J. **C 24**, 345-360 (2002)

[67] A. Adare *et al.,*Phys.Rev **D.85**.092004

[68] Zaida Conesa del Valle, Yasuyuki Akiba, Mickey Chiu, Mate Csanad, David d ' Enterria, Raphael Granier de Cassagnac, Joakim Nystrand, David Silvermyr, Sebastian White PHENIX internal analisys note 756

[69] C. Amsler *et al.,* (Particle Data Group), Physics Letters **B667**, 1 (2008).

[70] Cesar Luiz da Silva *et al.,* PHENIX PPG 104 (2010);

[71] PHENIX, MUTOO: PHENIX Muon tracker analysis framework, http://www.phenix.bnl.gov/phenix/WWW/publish/hpereira/doc/mutoo/html/index.html.

[72] A. Adare *et al.,*Phys. Rev. **C 86**, 064901 (2012) ,

[73] Golec-Biernat K and Wusthoff M, Phys. Rev. 1999 **D59** 014017

[74] Kopeliovich B Z, Sch*ä*fer A and Tarasov A V 2000 Phys. Rev. **D62** 054022